Experimental studies on statics and dynamics of some novel instabilities in lyotropic systems

by

Tripta Bhatia

Thesis submitted to the
Jawaharlal Nehru University
for the degree of
Doctor of Philosophy

Raman Research Institute
Bangalore 560 080
India

2012

DECLARATION

I hereby declare that the work reported in this thesis is entirely original. This thesis is composed independently by me at Raman Research Institute under the supervision of Dr. Y. Hatwalne. I further declare that the subject matter presented in this thesis has not previously formed the basis for the award of any degree, diploma, membership, associateship, fellowship or any other similar title of any university or institution.

(Dr. Y. Hatwalne) (Tripta Bhatia)

Soft Condensed Matter Laboratory
Raman Research Institute
Bangalore 560 080 - INDIA

CERTIFICATE

This is to certify that the thesis entitled **Experimental studies on statics and dynamics of some novel instabilities in lyotropic systems** submitted by Tripta Bhatia for the award of the degree of Doctor of Philosophy of Jawaharlal Nehru University is his original work. This has not been published or submitted to any other University for any other Degree or Diploma.

Prof. R. Subramanian
Director
Raman Research Institute
Bangalore 560 080 INDIA

Dr. Y. Hatwalne
(Thesis Supervisor)

Contents

Chapter 1

Introduction

In this Chapter, we give a brief introduction to the materials and experimental methods used in this thesis.

1.1 Lyotropic liquid crystals

Liquid crystals are phases of materials having features of both the solid and the liquid phase. There are two types of liquid crystal materials, thermotropic and lyotropic. Thermotropic liquid crystals show phase transitions upon change in temperature, whereas lyotropic liquid crystals are those that exhibit transitions on changing concentrations of water, oil, surfactants, or other species. Many materials exhibit both thermotropic and lyotropic liquid crystalline transitions, i.e. *mesomorphisms* [1].

Amphiphilic molecules in water display a variety of lyotropic liquid crystalline mesophases. Lipid molecules are amphiphilic molecules with hydrophilic and hydrophobic parts. In this thesis experiments are done using the lipid called DOPC (1,2-dioleoyl-sn-glycero-3-phosphocholine) (Fig. 1.1 (a)) in water, and water-glycerol mixtures.

In a mixture of lipid/water, the hydrophilic part forms hydrogen bonds with water, whereas hydrophobic part does not. The hydrogen bond network in the mixture gains entropy if lipid molecules spontaneously self-assemble in such a way that the hydrophilic part is hydrated with water and hydrophobic part is shielded [2]. Geometrical constraints imposed by the aggregate decides the effective shape of molecules (Fig. 1.1 (b)).

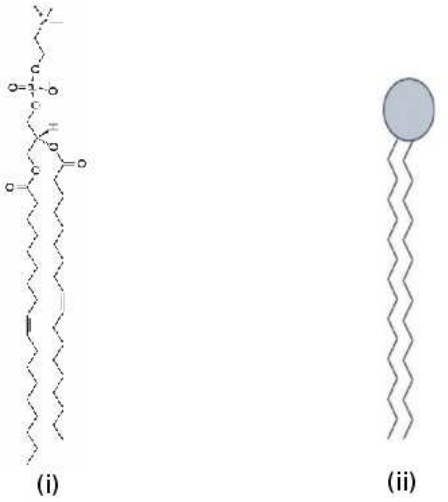

(a) (i) DOPC is a glycero-phospholipid, with PC headgroup and two hydrocarbon tails made up of oleic acid (18:1). The nomenclature represents the number of carbon atoms followed by number of double bonds (one double bond at the 9-10 positions of both the sn-1 and sn-2 chain), (ii) Symbolic representation.

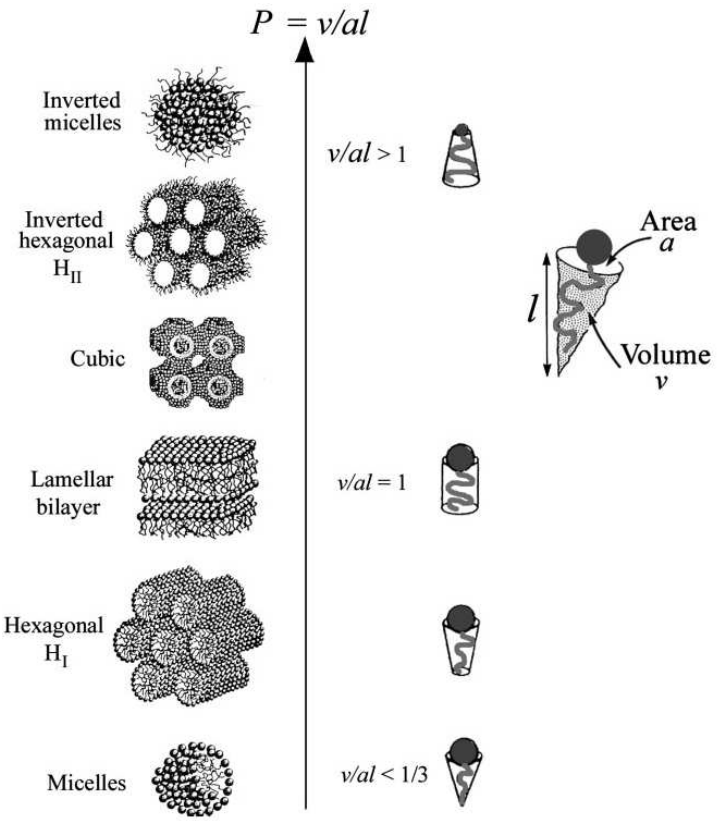

(b) Packing parameter *P* describes the effective shape of molecules in an aggregate, where *v* is the effective chain volume, *a* is the optimal headgroup area, with *l* as effective hydrophobic chain length of the molecule in an aggregate, taken from [2].

Figure 1.1

Lyotropic mesophases Phase-transition from one lyotropic phase to other can be induced by varying the hydration level, changing the temperature, changing the degree of unsaturation in the lipid tails, changing the hydrostatic pressure, screening the charge of headgroup by putting ions in the solvent, *etc.* [2].

Cylindrical molecules form flat bilayers (which consist of two monlayers, arranged such that the hydrophobic tails in each monolayer are facing towards each other). Several bilayers can self-organize to form 3-dimensional bilayer-stacks, a phase called the *lamellar or smectic-like phase*. Lamellar phases are one dimensional "solids" composed of fluid layers exhibiting quasi-long-range order in the direction orthogonal to the layers [3, 4].

A lipid bilayer is a soft fluid interface. In order to confine the lipid molecules within the bilayers various forces act inside the bilayer which are studied by the *lateral pressure or stress profile, p*(*z*) (Fig. 1.2). The interfacial tension of a fluid-bilayer interface is defined as $\gamma = (\partial G/\partial A)_v$ where G is the Gibbs excess free energy required to increase the area of the interface by adding one lipid molecule at constant volume, A is the area of the interface and v is the volume.

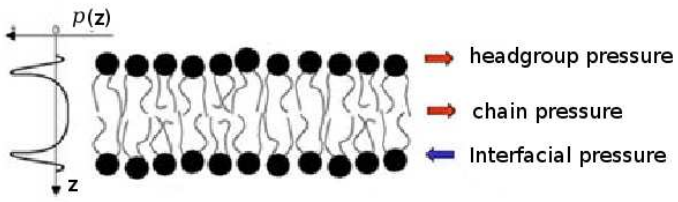

(a)

Figure 1.2: Schematic illustration of $p(z)$ of a lipid bilayer, revealing regions of expansive (positive) pressures and regions of large tensile (negative) pressures.

Due to the motion of the lipid molecules in a bilayer, individually, as well as collectively, the area of a lipid molecule fluctuates from its equilibrium area and costs energy. The time scales of different motions [2] depend on the type of the lipid molecule and the temperature. The spatial rotation of carbon-carbon bonds in the hydrocarbon chains takes time of the order of ps, rotation of a lipid molecule around its own axis takes a few ns.

The hydrocarbon chains can wobble or change direction within the bilayer in a time $\simeq$ 10 ms. A lipid molecule can diffuse in the plane of the bilayer in $\simeq$ 10 ns, and can protrude out of bilayer plane in $\simeq$ 10 ps. It can move from one monolayer to the other monolayer (flip-flop), in the time scale of hours. Typical values of $\gamma \simeq 50$ mN/m, $d_{\mathrm{L}} \simeq 3 - 5$ nm give $p(z) = (2\gamma/d_{\mathrm{L}})_v \simeq 350$ atm [2] within the hydrophobic region.

Lipid aggregates can also undergo internal phase transitions without changing morphology. PC headgroup lipids within a lamellar phase undergo different kinds of such phase transitions. The main transition (or chain-melting phase transition) is associated with two phases, one in which the lipid chains are more ordered- *solid ordered phase,* L_β (gel phase) and second in which are more disordered- *liquid disordered phase,* L_α (fluid phase). The thickness of bilayer d_{L} and area per molecule a_{L} changes in the main transition.

1.2 DOPC phases: structure and properties

DOPC (1,2-dioleoyl-sn-glycero-3-phosphocholine) molecules at room temperature form the L_α phase upon hydration. The $\mathrm{L}_\beta \rightarrow \mathrm{L}_\alpha$ transition temperature for DOPC is 232.7 K [5] in water at ambient pressure and is 240 to 260 K [6] in mixtures of glycerol/water (Fig. 1.3). The experiments are done at room temperature $\simeq 24$ °C (well within the L_α phase).

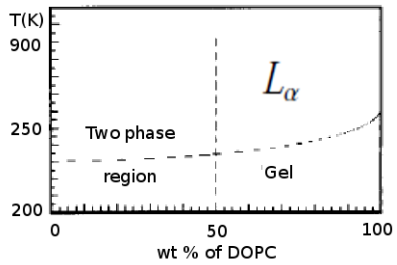

Figure 1.3: Schematic phase diagram of DOPC in glycerol/water mixtures. The phase transitions are illustrated by dotted lines. The vertical line separates two-phase regions from the L_α and gel phases. Taken from [6].

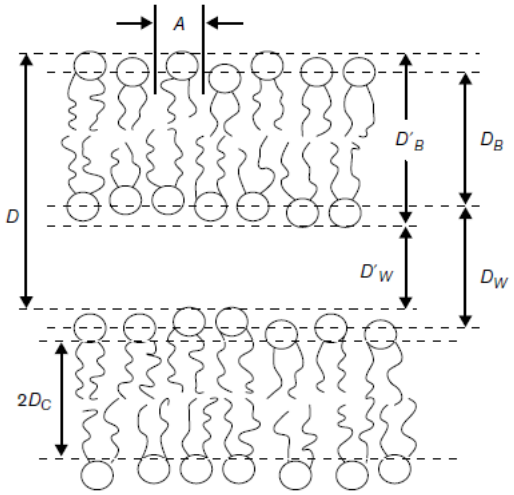

Figure 1.4: Taken from [8].

When aligned/oriented dried lamellar stacks are hydrated, the spacing between bilayers changes and reaches the maximum value at which hydrostatic equilibrium between all the forces [7] within the bilayers can be attained. Beyond this hydration, the bilayers peel off and become free. A phase separation between the fully hydrated bilayers and the excess water is attained. For two neutral bilayers separated by a distance D (Fig. 1.4) with water spacing D_{w} and bilayer thickness D_{B} the total force per unit area as a function of fluctuating water thickness z [8] is given by

$$P(z) = P_{\mathrm{vw}}(z) + P_{\mathrm{h}}(z) + P_{\mathrm{f}}(z) \tag{1.1}$$

Where $P_{\mathrm{vw}} = -(H/6\pi)[1/z^3 + 1/(z + 2d_{\mathrm{L}})^3 - 2/(z + d_{\mathrm{L}})^3)]$ is the Van der Waals pressure (H is the Hamakar's constant), $P_{\mathrm{h}} = A_{\mathrm{h}} \exp(-z/\lambda_{\mathrm{h}})$ is the hydration pressure ($lambda_{\mathrm{h}}$ is the decay length of the hydration pressure), and $P_{\mathrm{f}} = (A_{\mathrm{f}}/\lambda_{\mathrm{f}}) \exp(-z/\lambda_{\mathrm{f}})$ is the fluctuation pressure ($lambda_{\mathrm{f}}$ is the decay length of the fluctuation pressure). Bilayer structural parameters (Fig. 1.5) at different degrees of hydration are studied by mainly two methods, the osmotic pressure method and the hydration method, using x-ray or neutron diffraction techniques. The values for $A_{\mathrm{h}} = 0.55 \times 10^8 \mathrm{J/m}^3$ and $\lambda_{\mathrm{h}} = 2.2\text{Å}$ at 30 °C are reported in [8].

	45°C	30°C	15°C
Volume per molecule($Å^3$)	1318	1303	1288
D-spacing(Å)	63.3*	63.2*	62.8*
Bilayer thickness D_{HH}(Å)	36.1	36.7	37.6
Hydrocarbon thickness $2D_C$(Å)	26.2	26.8	27.7
Area per molecule A($Å^2$)	75.5	72.4	69.1
Interbilayer water spacing D_W' (Å)	19.2*	18.4*	17.1*
Steric bilayer thickness D_B' (Å)	44.2	44.8	45.7
Bending ridigity $K_C(10^{-20}$ J)	7.2	7.6	8.5
Stretch modulus K_A (mN/m)	252	254	264
λ_{fl} (Å)	6.4	5.9	6.4
Hamaker coefficient H (10^{-21} J)	5.4	5.4	5.2

Figure 1.5: Structural and material parameters of DOPC (fully hydrated multi-lamellar sample), taken from [8].

DOPC lamellar phase in glycerol/water 91 : 9 (w/w) mixture reaches its maximum swelling at about 50% (w/w) of DOPC [6]. The refractive index of the L_α phase composed of 80% DOPC in a 91 : 9% mixture of glycerol and water has been determined as a function of temperature [6].

1.3 Rhd-DHPE structure and properties

In our experiments we have used a head-group labelled phospholipid fluorochrome rhodamine-DHPE (lissamine rhodamine B 1,2-dihexadecanoyl-sn-glycero-3-phosphoethanolamine, triethylammonium salt) (Fig. 1.6) with $\lambda_{abs} = 560\,nm$ and $\lambda_{em} = 580\,nm$ for the peak intensity. The absorbance and the emission fluorescence for this probe are discussed in [9]. The fluorescence anisotropy of rhodamine-DHPE in phosphatidylcholine bilayers has been studied in [10] where it is reported that (*i*) the dye does not induce intrinsic curvature in fluid bilayers, and (*ii*) in the fluid phase the in-plane diffusion constant of the dye molecules is the same as that of the lipid molecules in which it is incorporated. The effect of concentration of the probe on fluorescence is studied in [11].

The fluorescence life-time τ_f is defined as the mean time a fluorescent molecule (fluorochrome) spends in the excited state before returning to the ground state. The rota-

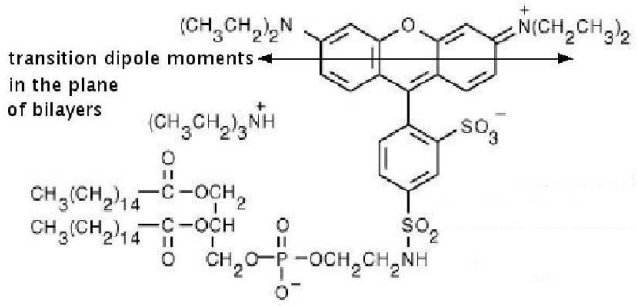

(a) Structure.

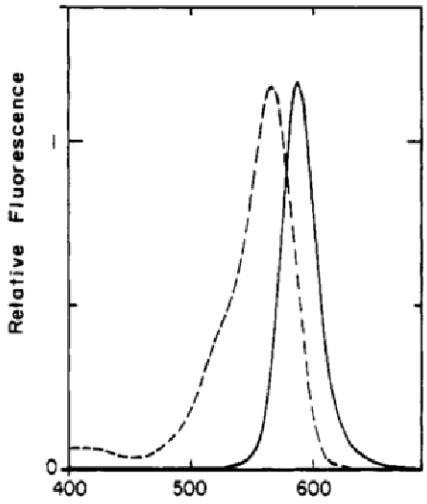

(b) Dotted line shows absorption and continuous line shows emission spectra of the rhodamine probe.

Figure 1.6: rhodamine-DHPE.

tional diffusion time τ_{rd} is the time taken by the fluorochrome to complete one free rotation around its long axis. For $\tau_{rd} > \tau_f$ the emission transition dipole moment can be assumed to be parallel to the absorption transition dipole moment. Effects of pH, temperature, ionic strength, viscosity and the presence of dissolved oxygen on fluorescence have also been studied. The properties of this dye are summarised in Table 1.1.

Table 1.1

λ_{abs} (nm)	λ_{em} (nm)	D_{td} (m^2/s)	τ_f (ns)	τ_{rd} (ns)	V_{th} (mole/mole)
560	580	10^{-10}	4	10	0.005

The amount of probe used in the experiments reported in this thesis is 0.002 mole per mole of DOPC which is much below V_{th} (threshold above which dye molecules self aggregate) [12]. Orientation of this probe in DOPC bilayers [12] has been studied (Fig. 1.7). The experiments are done at room temperature $\simeq 24\ ^{\circ}C$ at which the lipid and the dye are in the fluid phase.

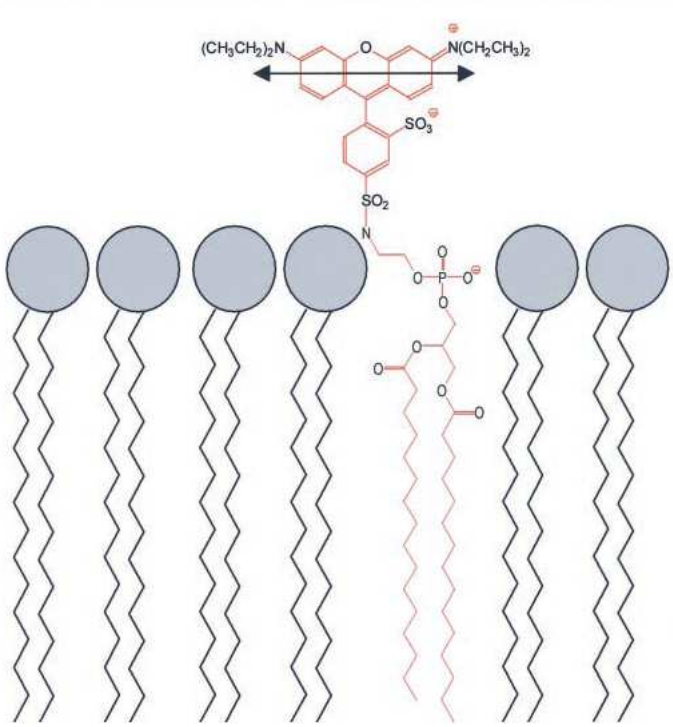

Figure 1.7: Orientation of the fluorescence probe in lipid bilayer, taken from [12].

r_{max}	τ_f/ns	ϕ_c/ns	n_{eo}	n_0	n	S	T/K	$k_e \times 10^{-7}$
0.328	3.9	14.9	1.477	1.458	1.465	−0.36	273.6	4.3[b]
0.294	2.4	5.5	1.469	1.453	1.459	−0.36	294.0	7.4[b]
0.265	1.3	2.1	1.462	1.448	1.453	−0.35	313.6	10.3[b]

Figure 1.8: Taken from [13].

Maximum fluorescence anisotropy r_{max}, fluorescence lifetime τ_f, rotational correlational time ϕ_c, ordinary n_o and extra-ordinary n_{eo} refractive indices and order parameter S (for the

absorption and emission transition dipole moments) of octadecylrhodamine-B/DOPC/water in the L_α phase have been studied [13] at different temperatures (Fig. 1.8).

1.4 Experimental methods

For optical observations we have used (*i*) unpolarized fluorescence microscopy and (*ii*) Fluorescence confocal microscopy (FCM) with He-Ne laser line (543 nm), equipped with emission filter adjusted in the wavelength band for rhodamine dye. The sample is maintained at room temperature ($\simeq$ 24°C).

1.4.1 Fluorescence microscopy

Fluorescence (Fig. 1.9) is a phenomenon in which an electron which is typically in the lowest vibrational level of the ground state absorbs incident light of wavelength λ_{abs} and gets raised to an excited singlet state [14]. The molecule spends $\simeq 10^{-4}$ s in the excited singlet state and dissipates some energy rapidly from a higher vibrational state to the lowest vibrational level within the excited singlet state. If more energy is not dissipated by collisions with other molecules then the electron returns to the ground state with the emission of energy at a longer wavelength λ_{em}. Fluorescence probes (also known as fluorochromes or fluorescent

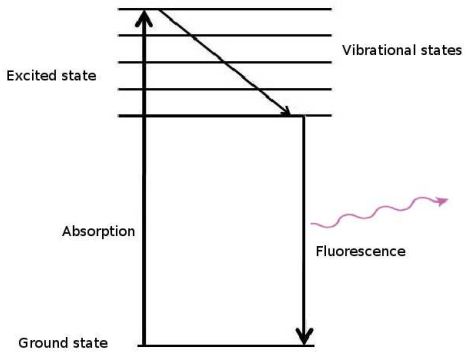

Figure 1.9: Jablonski diagram.

dyes) exhibit this phenomenon. A fluorochrome has two characteristic spectra corresponding to absorption emission.

1.4.2 Fluorescence confocal microscopy

LEICA TCS-SP2 with galvo-scanning mechanism was used [15] in the experiments. A collimated linearly polarized laser beam (Fig. 1.10) passes through the AOTF-(Acousto-Optical-Tunable-Filters), excitation pin-hole (illuminating aperture), AOBS (Acousto-Optical-Beam-Splitters), the scan head, and into the rear of the objective lens that focuses the light on a diffraction limited spot in the specimen (the focal point). Before starting the experiment it is necessary to configure the AOTF and AOBS depending on the dye used. The reflected light from focal point passes back through the same lens, followed by the AOBS, and is focused into the detection pin-hole (PH) in front of the PMT (photo-multiplier tube) such that the focal point and the pin-hole are in conjugate focus (confocal). The pin-hole blocks all light except that which emerges from the focal point.

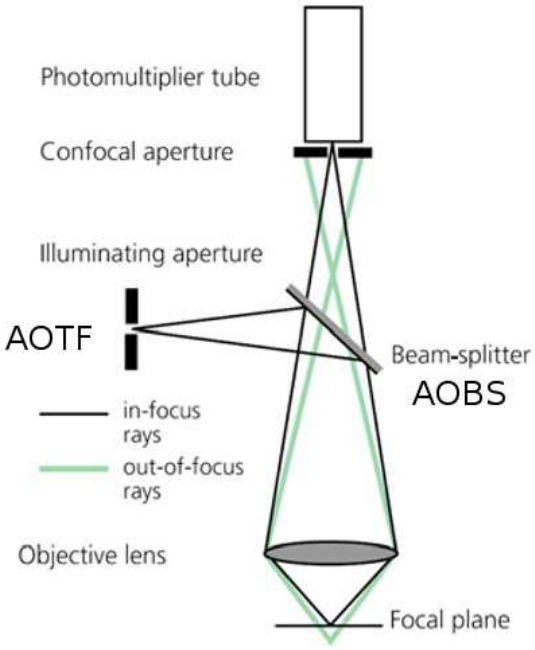

Figure 1.10: Schematic of a point-scanning confocal system in the reflection imaging mode.

Bibliography

[1] S. T. Hyde, *Handbook of Applied Surface and Colloid Chemistry*, (J. Wiley and Sons, pp. 299-332, Chapter 16, 2001).

[2] O. G. Mouritsen, *Life - As a Matter of Fat*, (Springer, 2005).

[3] P. M. Chaikin and T. C. Lubensky, *Principles of condensed matter physics* (Oxford University Press, 1998).

[4] P. G. de-Gennes and J. Prost, *The physics of liquid crystals* (Oxford University Press, 2nd edition, 1994).

[5] Shoji Kaneshina, Hayato Ichimori, Takashi Hata and Hitoshi Matsuki, Biochimica et Biophysica Acta, 1374, 1-8 (1998).

[6] Lennart B. A. Johansson, Bjrn Kalman, Gran Wikander, ke Fransson, Krister Fontell, Bjrn Bergensthl and Gran Lindblom, Biochimica et Biophysica Acta, 1149, 285-291 (1993).

[7] John F. Nagle and Stephanie Tristram-Nagle, Biochimica et Biophysica Acta, 1469, 159195 (2000).

[8] Jianjun Pan, Stephanie Tristram-Nagle, Norbert Kuerka, and John F. Nagle, Biophysical Journal, 94, 117-124 (2008).

[9] Douglas K. Struck, Dick Hoekstra, Richard E. Pagano, Biochemistry 20, 4093-4099, (1981).

[10] S. Massari; R. Colonna; E. Folena, BBA - Biomembranes 940 (1), 149-157, (1988).

[11] R. I. MacDonald, J. Biol. Chem. 265 (23), 13533-13539, 08, (1990).

[12] L. A. Bagatolli and E. Gratton, Biophysical Journal, 78, 290305 (2000).

[13] Jan Karolin, Stein-Tore Bogen, Lennart B. A. Johansson and Julian G. Molotkovsky, Journal of Fluorescence, 5(3), 279-284 (1995).

[14] Joseph R. Lakowicz, *Principles of fluorescence spectroscopy* (Springer, 3rd edition, 2006).

[15] James Pawley, *Handbook of Biological Confocal Microscopy* (Springer, 3rd edition, 2006).

Chapter 2

Materials, calibration and compilation of experimental observations

There has been much interest in structural and dynamical studies of amphiphilic systems driven far from equilibrium by strong external perturbations such as shear [1, 2, 3]. In contrast, there is not much systematic study on the morphology and dynamics of structures following a quench from an equilibrium phase. In this Chapter, we compile some broad experimental results on the dissolution of amphiphiles in contact with excess water and discuss possible mechanisms which can qualitatively interpret these observations.

2.1 Materials

We have used the following materials in the experiments without further purification: DOPC (1,2-dioleoyl-sn-glycero-3-phosphocholine) from Sigma, Egg-PC from Sigma, rhodamine DHPE (lissamine rhodamine B 1,2-dihexadecanoyl-sn-glycero-3-phosphoethanolamine, triethylammonium salt) from Molecular Probes, Fluorescent polystyrene beads (200 nm, λ_{ex} = 488 nm, λ_{em} = 515 nm) from Polysciences. We have used reagent grade glycerol, de-ionized water (millipore), chloroform and methanol from commercial sources.

2.2 Calibration of the optical system

The degree of spreading (blurring) in the image of a point source is a measure of the quality of the optical system and is called the point spread function (psf) of the optical device. The

lateral and axial psf completely specify the response of the confocal microscope to a point source (for a given objective, and at a given wavelength of the confocal microscope to a point source).

2.2.1 Confocal resolution

Two self-luminous points will be seen as two distinct points (Fig. 2.1) only if their psfs are distinct. According to the Rayleigh criterion there is sufficient contrast between two objects if the central maximum of the Airy disc of one object lies on the first minimum of the Airy disc of second object, giving $d_{xy} = (0.61\lambda/\text{NA})$, where NA is the numerical aperture.

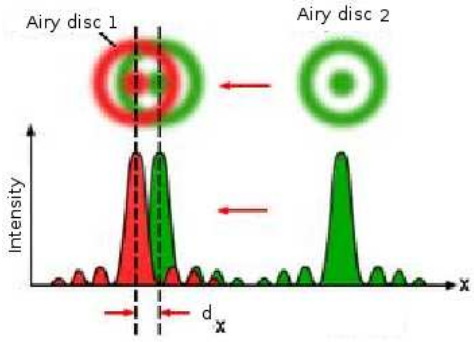

Figure 2.1

Theoretical calculations for confocal resolution [4] with no refractive index mismatch between the bead and the objective front-lens give $d_{xy} = 0.42\,(\lambda_{\text{av}}/\text{NA})$ and $d_z = 0.81\,(\lambda_{\text{av}}/(n - \sqrt{n^2 - \text{NA}^2}))$ for PH = 1 Airy Unit (AU) with $\lambda_{\text{av}} = \sqrt{2}\,\lambda_{\text{em}}\,\lambda_{\text{abs}}/(\sqrt{\lambda_{\text{em}} + \lambda_{\text{abs}}})$, where n is refractive-index of the objective immersion medium.

2.2.2 Measuring psf

Ideally, the measurement of the psf should be made under conditions approximating those in the actual specimen. But injecting the beads into the specimen and then measuring the psf is difficult. The psf was measured by taking xyt- and xyz-scans of 200 nm isolated polystyerene fluorescent beads ($\lambda_{\text{abs}} = 488\,\text{nm}$, $\lambda_{\text{em}} = 515\,\text{nm}$) settled on the cover-slip in water [5]. We follow the following procedure：

- We work with a dilution of 1 : 10000 of beads in water, so that the density of the beads in water is low enough and the Airy pattern of one bead does not overlap with the Airy-pattern of the second bead.

- We pipette about 10 μl of bead solution into a cover-slip cell (two bare cover-slips of thickness 0.15mm glued at two parallel edges) and allow the beads to settle down. We seal the other two open edges of the cell with silicone glue after the solvent fills the whole cell. After half-an-hour we find many beads stuck to the surface of the bottom cover-slip. We have used 40$\times$ dry objective with NA = 0.85 to image the sample.

- The two-dimensional image of a point source (Fig. 2.2) is $I = I_0(2J_1(x)/x)^4$, the Airy pattern with normalised intensity distribution, where J_1 is Bessel function of the first kind, $x = (a\,k\,\sin\theta)$, a is the radius of aperture, I_0 is the peak intensity, θ is the angle of observation and $k = 2\pi/\lambda$ is the wavenumber with λ as the wavelength of observation. The central lobe of the Airy profile can be approximated as a Gaussian $\mathrm{I_G} = A\,\mathrm{e}^{-}(x^2/\sigma^2)$.

- We analyzed the intensity profiles of 10 fluorescence beads. From the Gaussian fit (Fig. 2.3) we get $\mathrm{d}_x = \mathrm{d}_y \simeq 0.56\mu$m and $\mathrm{d}_z \simeq 2.56\mu$m, where d is the fwhm of the Gaussian fit.

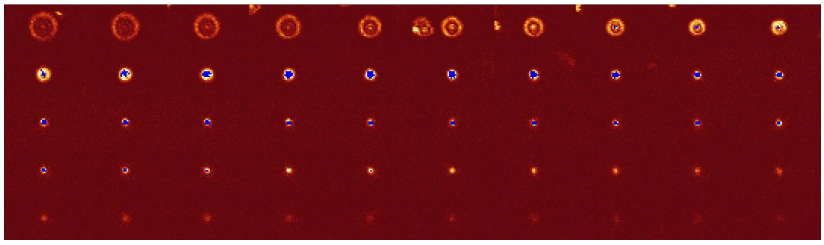

Figure 2.2: Each of the images corresponds to the Airy profile at a different depth (z), starting from the bottom of the bead towards the top. To be seen from top left in rows.

2.2.3 Positional accuracy

Rayleigh criterion considers only the limited NA of the objective to define resolution. Orhaug [6] , Falconi [7] and Fried [8] showed that the uncertainty in determining the position of

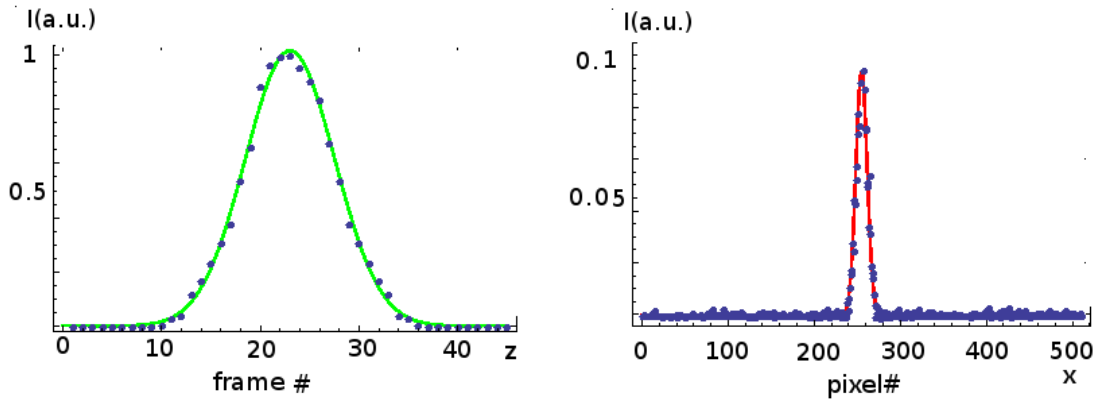

(a) Axial psf, 10 pixels = 2 μm, intensity in arbitrary units (a.u.).

(b) In-plane psf, 30 pixels = 0.92 μm

Figure 2.3: Solid line shows the Gaussian fit.

a point source also depends on the signal to noise ratio (SNR = $I_{\rm av}/\sigma$). The positional uncertainty is defined by [9]

$$\triangle x = \frac{(\sigma/I_{\rm av})}{\sqrt{\left(\sum_k (\Delta I_{\rm k}/\Delta x_{\rm k})\right)^2}}, \tag{2.1}$$

where σ is the root mean square deviation of the noise and has the dimension of intensity, $I_{\rm av}$ is the average intensity, $I_{\rm n}^{\rm k}$ is the normalised intensity at $k^{\rm th}$ point, with N points in the profile.

2.3 Sample preparation

2.3.1 Sample cells

Two types of sample cells are used in the experiments (Fig. 2.4). In the cover-slip sample cell, two cover-slips (one is sample-coated and the other is bare) are separated by a thin layer $\simeq$ 100 μm of silicone glue. In the Pt-wire sample cell, a Pt- wire (length $\simeq$ 10 mm, diameter$\simeq$ 250 μm) is positioned at the center across a chamber of height $\simeq$ 4 mm. The bottom of the chamber is sealed with a glass cover-slip. The gap between the wire and the bottom cover-slip is $\simeq$ 50 μm so that observations under an inverted microscope (Olympus IX70) are facilitated.

Before coating the sample, Pt-wire is carefully cleaned with chloroform/ethanol. The cover-slips are cleaned in an ultrasonic methanol bath for about 10 minutes and sub-

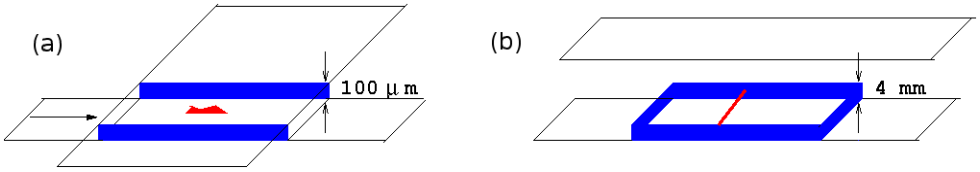

Figure 2.4: (a) The cover-slip, and (b) The Pt-wire sample cell, red and blue colors represent the sample and glue respectively.

sequently rinsed in methanol followed by millipore water. Both cells are dried in nitrogen stream and kept in vacuum overnight.

2.3.2 Sample coating

Smooth cover-slips are selected after scanning under the AFM [10]. Typical histogram of surface height variation of bare coverslips has width of distribution ±3.5 nm. Sample is coated (Fig. 2.5) on cover-slips in two ways; using either Hamilton's syringe or a spin-coater. Syringe-coating is done by pipetting 4 μl of the lipid solution (0.5 mg/ml lipid in chloroform) and deposited on a dried substrate. In spin-coating [11, 12], lipid solution is pipetted and deposited centrally onto the dried substrate spun at 4000 rpm (from the beginning because chloroform in the sample evaporates fast). The coated lipid forms a lipid reservoir which is subsequently hydrated.

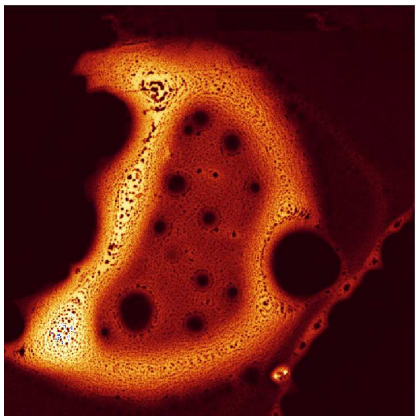

(a) DOPC syringe-coated cover-slip, image size ≃ 1.12 mm.

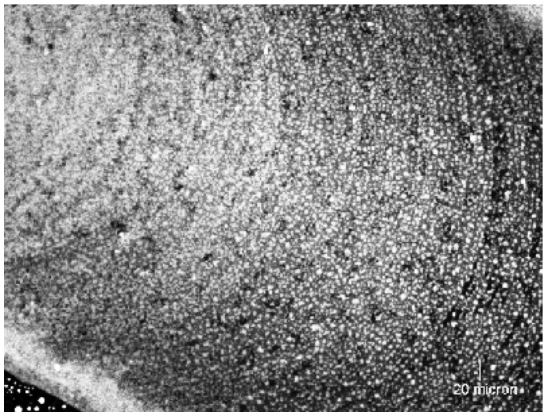

(b) Egg-Lecithin spin-coated cover-slip, image width ≃ 364 μm.

Figure 2.5: Unpolarized fluorescence image of sample before hydration.

2.4 Hydration of the sample

In cover-slip sample cells the solvent (water/water-glycerol mixture) is added at one of the open edges. Hydration takes place due to capillary action. In the Pt-wire sample cell, solvent is pipetted into the chamber from top. After the Pt-wire is fully immersed in the solvent the chamber is covered, but not sealed by a cover-slip at the top to prevent evaporation. Sample cells are then left undisturbed till the completion of the experiment. Syringe-coated cover-slips upon hydration does lead to the formation of multi-lamellar structures (Fig. 2.6) and we do not observe similar structures on spin-coated cover-slips upon hydration.

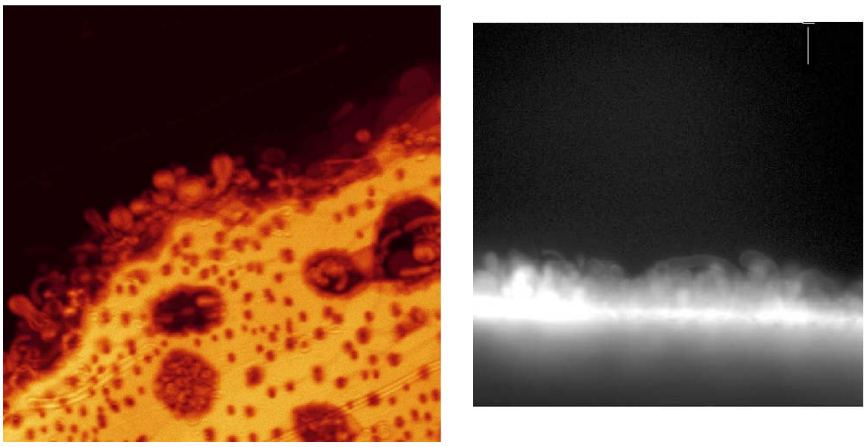

(a) DOPC hydration with glycerol-water $(1:4)$ v/v, image size $331\,\mu\text{m} \times 331\,\mu\text{m}$.

(b) DOPC hydration with water, scale bar = $20\,\mu$m.

Figure 2.6: Upon contact of solvent with the concentrated surfactant, multi-lamellar structures like blobs, thick tubules $\simeq 50\,\mu$m and vesicles start growing from the lipid reservoir.

2.5 An abrupt instability (the burst)

We have seen that subsequent to the nucleation of multilamellar amphiphilic structures the system under study initially evolves slowly and multilamellar structures nucleate (Fig.2.7c), followed by a dramatic and sudden instability (movie 2.5, see the cd inside the back cover). In unsealed cells a sudden explosive event (burst) occurs after about 20 to 40 minutes of hydration and debris of the lipid material gets pitched into the solvent. These lamellar blobs are attached to the lipid reservoir through thin tethers (Fig. 2.7). The burst occurs at arbitrary parts of the reservoir and not everywhere and therefore it is not possible to make any

systematic studies of the time elapsed before the burst. In sealed cells, we do not observe the burst, but we observe structures similar to those seen post-burst in unsealed cells. In sealed cells, the time gap between hydration and observation of the sample is $\simeq$ 30 minutes.

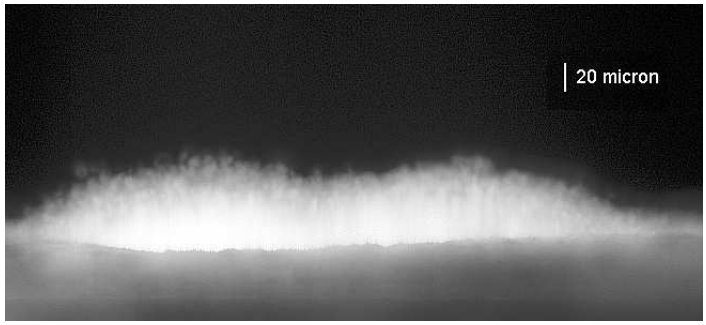

(a) Before burst.

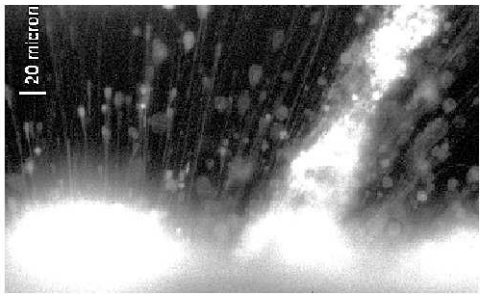

(b) Burst: after about 22 minutes of adding water.

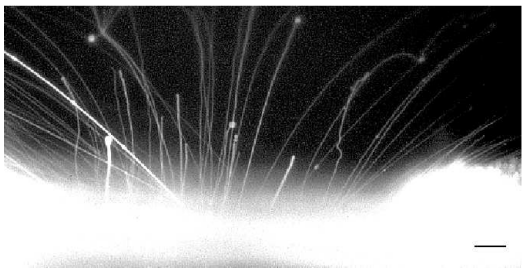

(c) About 20 minutes post-burst.

Figure 2.7: Scale bar = 20μm.

2.5.1 Growth of tubules post-burst

The burst leads to growth of new multi-lamellar tubules (MLTs) (Fig. 2.7(c)) with outer diameter $\simeq 10\,\mu$m. Some of these MLTs retract into the reservoir. The growth and retraction of tubules is discussed in the section 2.6.2. All MLTs retract into the reservoir as the solvent evaporates (it takes 4 to 5 hours for the solvent to evaporate completely). MLTs grow again upon rehydration, but the growth is not preceded by the burst. Some of the cover-slip sample cells are sealed immediately after filling the cell with the solvent. In the sealed chambers post-burst growth and retraction of multi-lamellar structures gets arrested for about a day or so (movie 2.5.1).

2.6 Post-burst observations

Sealing the sample-cell enables us to image the MLTs using confocal microscopy. These quasi-static observations reveal the structure of the MLTs (and that of beads *etc.* see below). Using the unsealed sample-cells we make measurements of dynamical phenomena (such as growth and retraction of tubules, coalescence of beads, *etc*, movie 2.6).

2.6.1 Structural observations

2.6.1.1 Multi-lamellar tubules

The tubules have a jelly-roll structure with a core, they are multi-lamellar (Fig. 2.8 and Fig. 2.9).

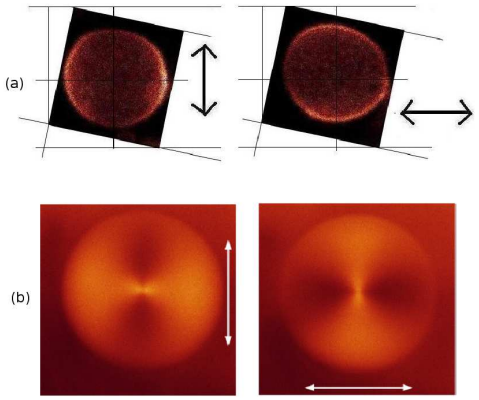

Figure 2.8: FCM observation of (a) Giant-unilameller-vesicle (GUV) (b) cross-sectional view of a tubule showing that the tubules are not unilamellar.

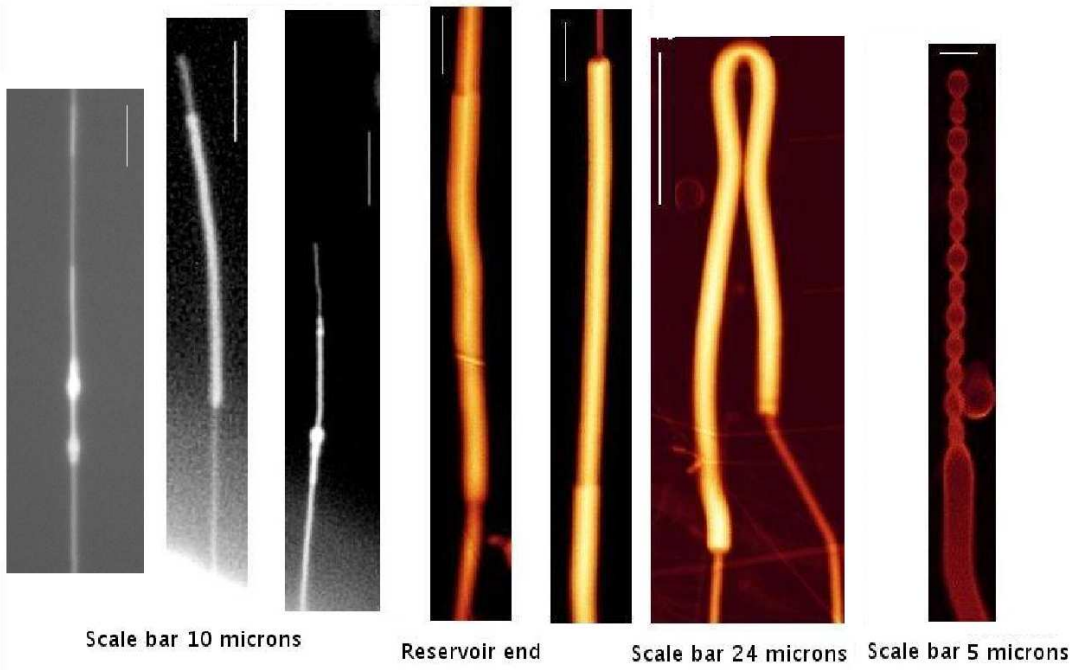

Figure 2.9: Different tubules, fluorescence images.

MLTs are rooted at defects in the lamellar structure in the lipid reservoir (see confocal xyz- scans shown in the series of images (Fig. 2.10 and movies 2.6.1.1).

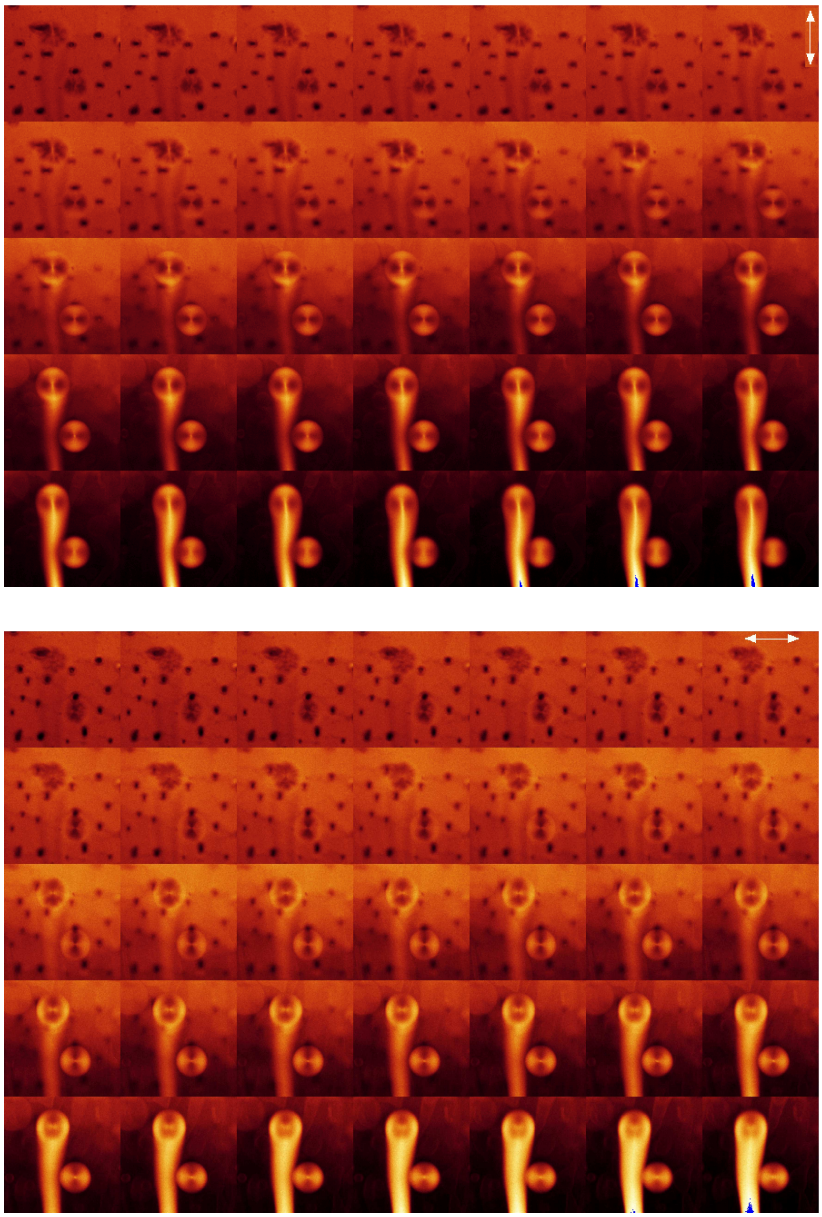

Figure 2.10: Each of the constituted images is $51\,\mu$m $\times$ $51\,\mu$m. Succesive images corespond to increasing z-values.

The roots of tubules which do not grow (most likely because of sealing the cell) are also observed (Fig. 2.11, movie 2.6.1.1).

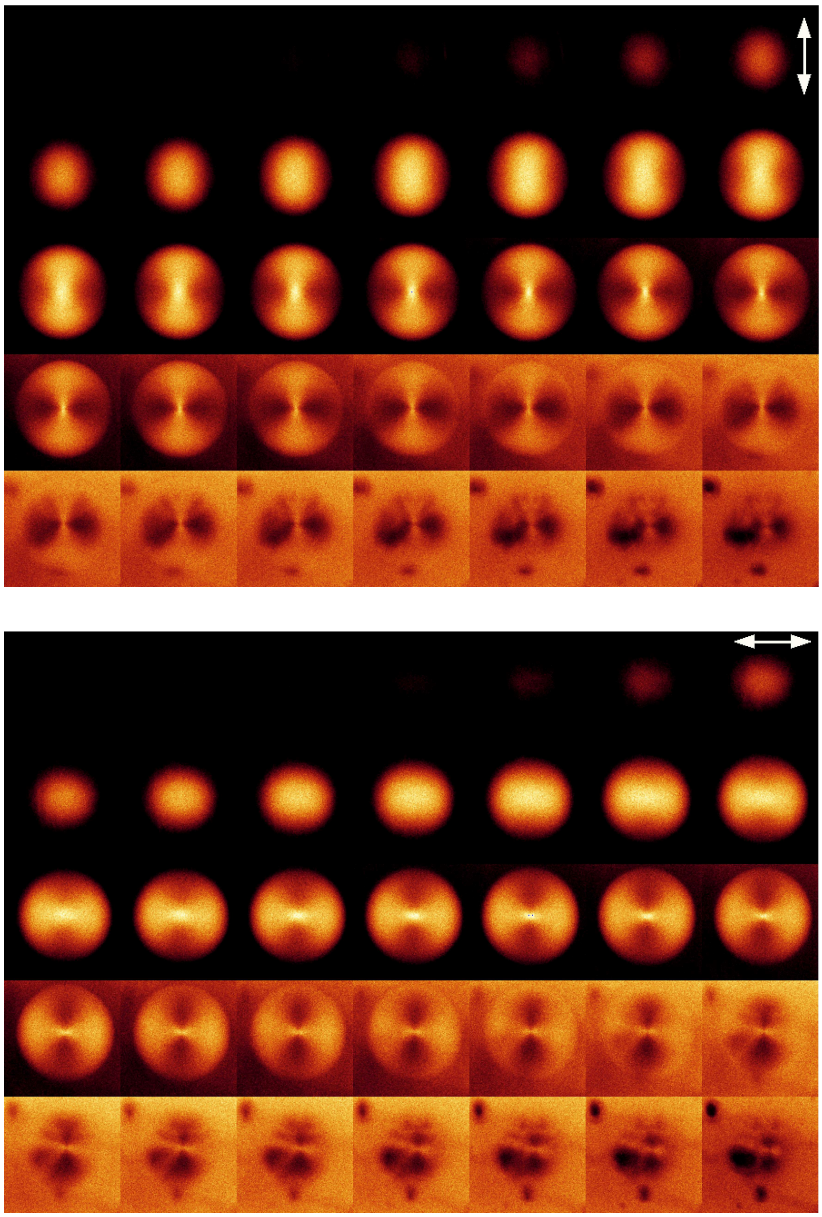

Figure 2.11: Hemispherical capped structures which have not grown, single image size $21\,\mu$m$\times 21\,\mu$m.

2.6.1.2 Another instability - formation of beads

Some MLTs undergo a further instability. Bead-like structures develop on these MLTs (Fig. 2.12). Dynamical measurements on beads are discussed in section 2.6.2.

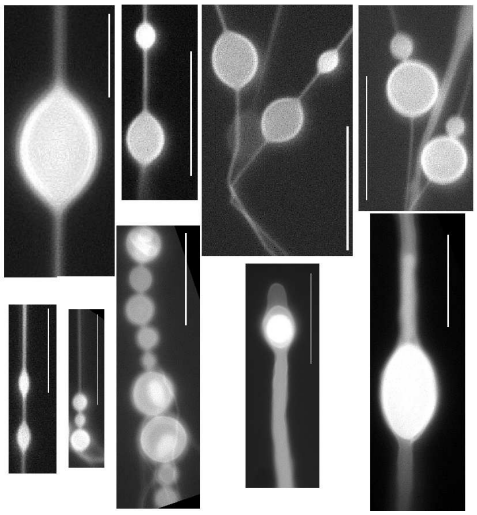

(a) Unpolarized fluorescence microscope images, scale bar = 20μm.

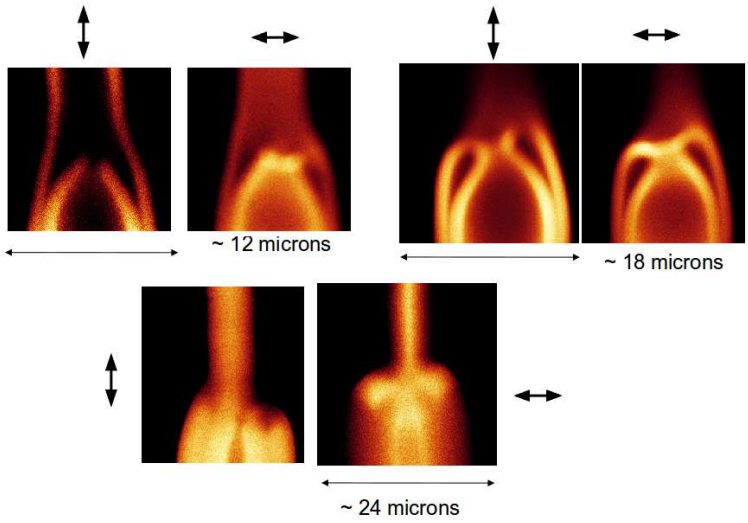

(b) Confocal xyz-scans, at the mid-plane of the beads. Arrows show the direction of incident beam polarization.

Figure 2.12

2.6.1.3 Dense multilamellar structures

After a day or two, the sample cell fills up with dense multi-lamellar structures (Fig. 2.13 and movies 2.6.1.3). After 3 days, further optical observations cannot be made.

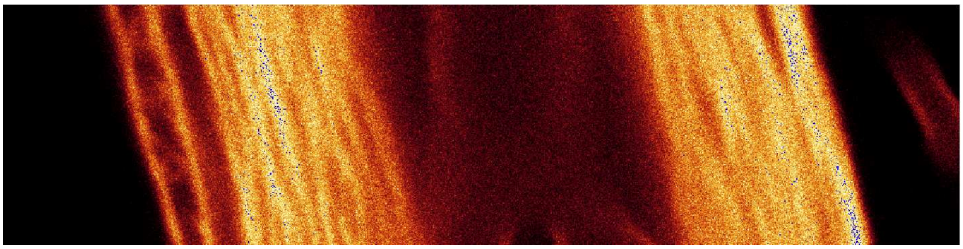

(a) image $40\mu\text{m} \times 10\,\mu\text{m}$.

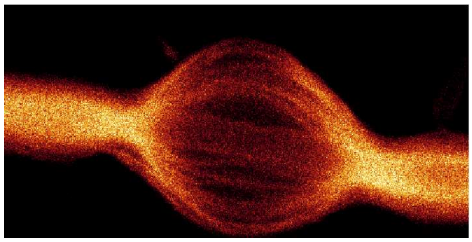

(b) image $\simeq 26\mu\text{m} \times 13\,\mu\text{m}$.

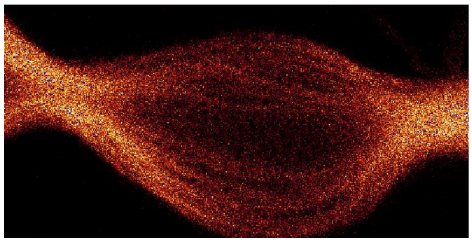

(c) image $\simeq 26\mu\text{m} \times 13\,\mu\text{m}$.

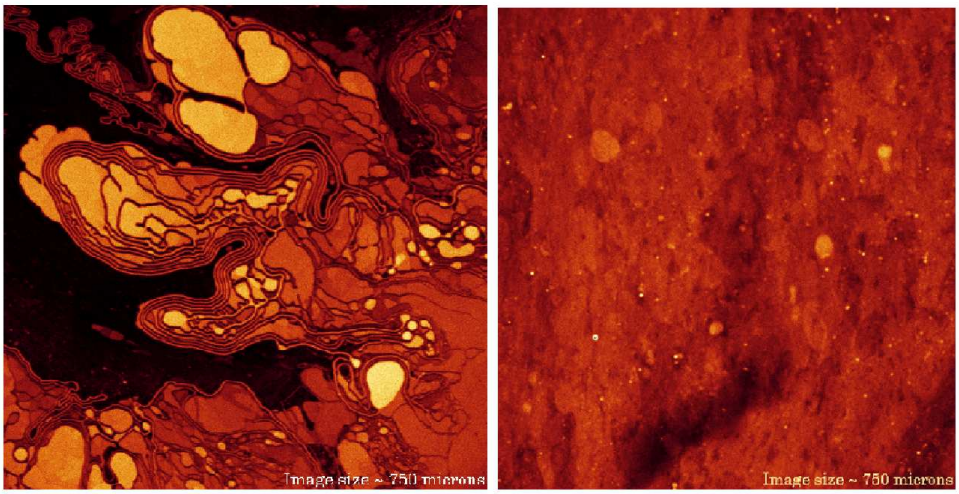

(d) 3rd day, image $\simeq 750\mu\text{m} \times 750\,\mu\text{m}$.

Figure 2.13

2.6.2 Dynamics

We use unsealed sample cells to observe dynamical phenomena. Nucleation of new tubules continues as long as the solvent does not evaporate. We observe many interesting phenomena

such as retraction of MLTs into lipid reservoir, formation of bulges due to retraction, *etc*.

2.6.2.1 Growth and retraction

We track the tip of an appropriately selected tubule and find that growth and retraction speed of tubules ranges roughly from 1 μm/s to about 40 μm/s Figs. (2.14 to 2.16 and movie 2.6.2.1).

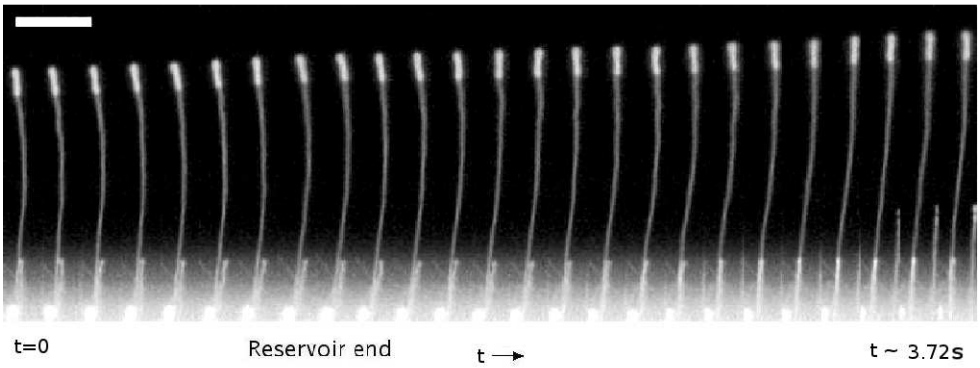

(a) Scale bar = 20 μm.

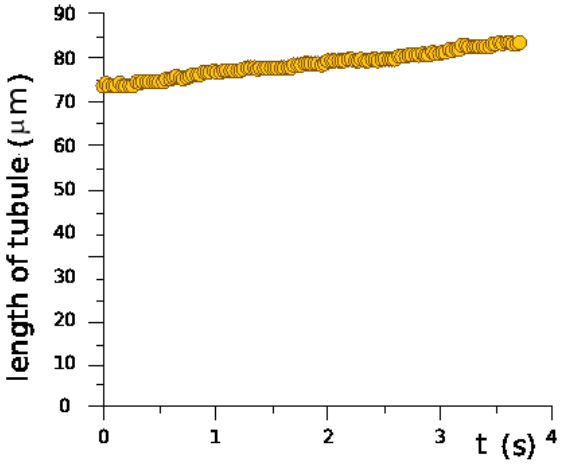

(b)

Figure 2.14: Growth.

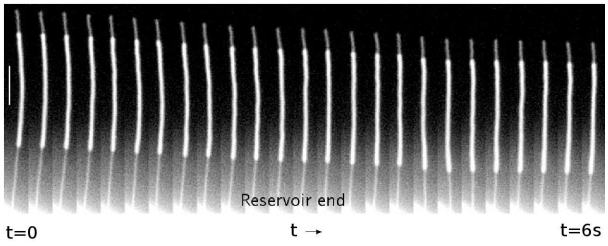

(a) Scale bar = 20 μm.

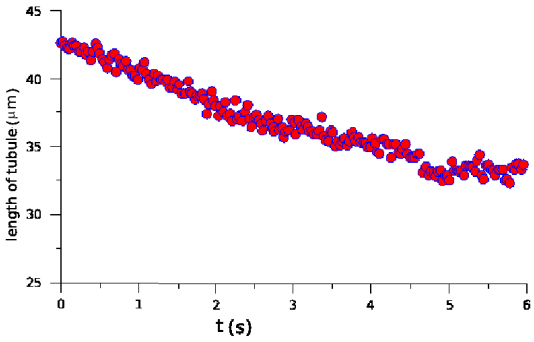

(b) Retraction.

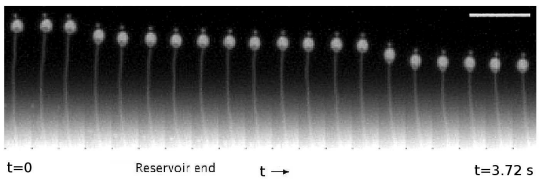

(c) Scale bar = 20 μm.

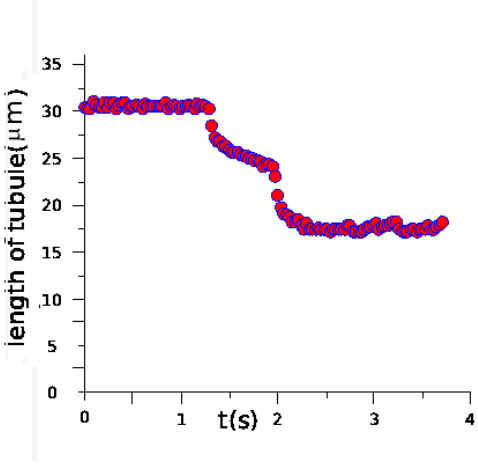

(d) Jerky retraction.

Figure 2.15: Retraction.

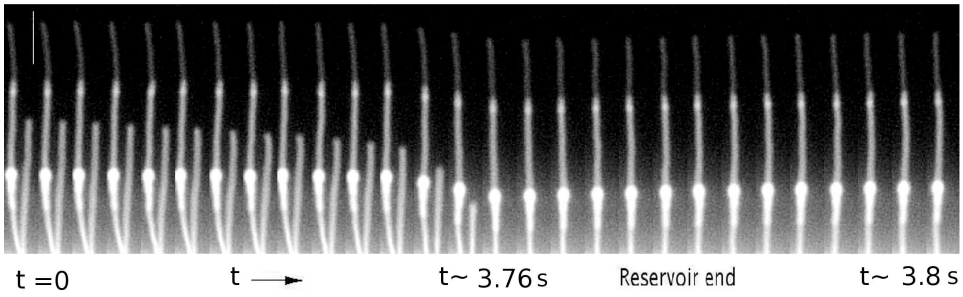

(a) Scale bar = 20 μm.

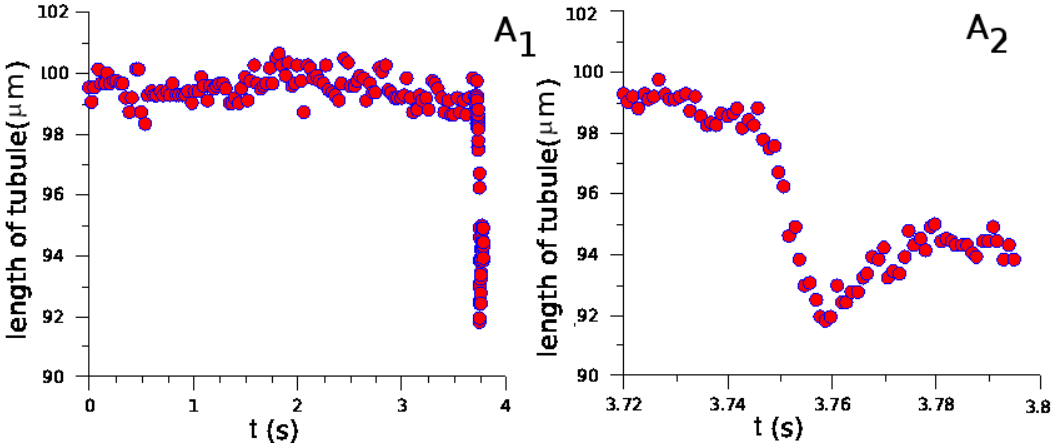

(b) Retraction followed by growth. A_1: 1st tubule from left, A_2 is the enlarged portion of A_1.

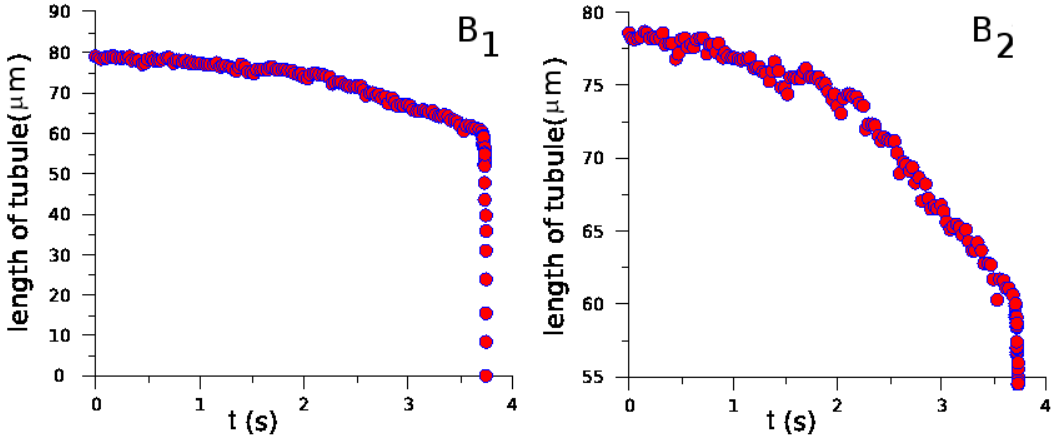

(c) Fast retraction, B_1: 2nd tubule from left. B_2 is the magnified portion of B_1.

Figure 2.16

2.6.2.2 Branching and bulging of tubules

Tubules having branches and bulge are observed (Fig. 2.17 and movies 2.6.2.2).

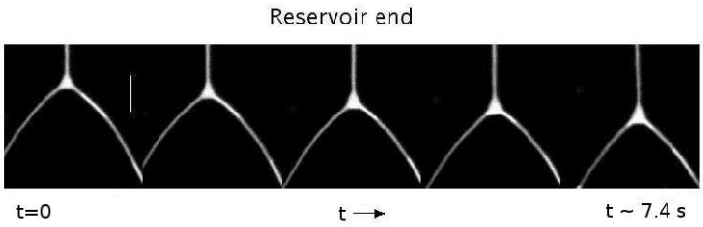

(a) Branching.

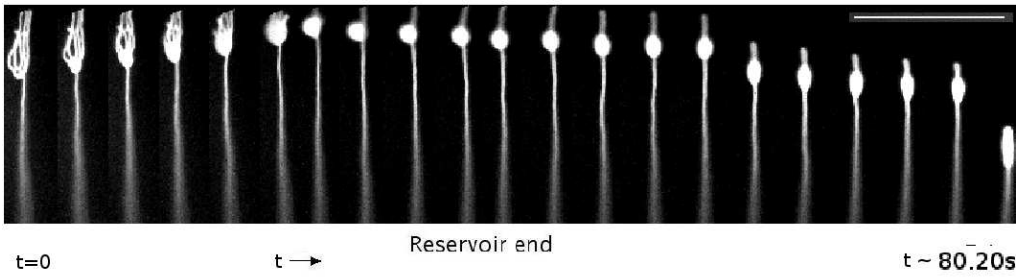

(b) Branch to bead.

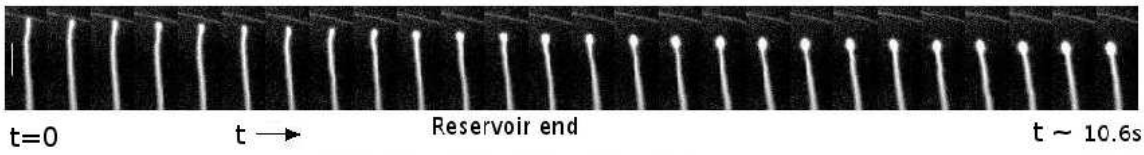

(c) A significant fraction of tubules form a bulge at the tip.

Figure 2.17: Scale bar = 20μm.

2.6.2.3 Bead formation

Beads (Fig. 2.18) form on most MLTs, typically near the reservoir. These beads move away from the reservoir end as the MLT grows. Beads also form between two beads approaching each other.

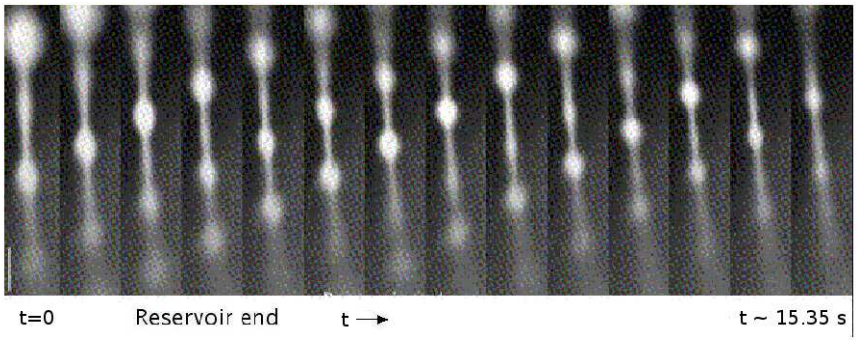

Figure 2.18: Scale bar = 20μm.

2.6.2.4 Dispersion of beads into MLTs

Many of the beads shrink gradually and disappear altogether (Fig. 2.19 and movies 2.6.2.4).

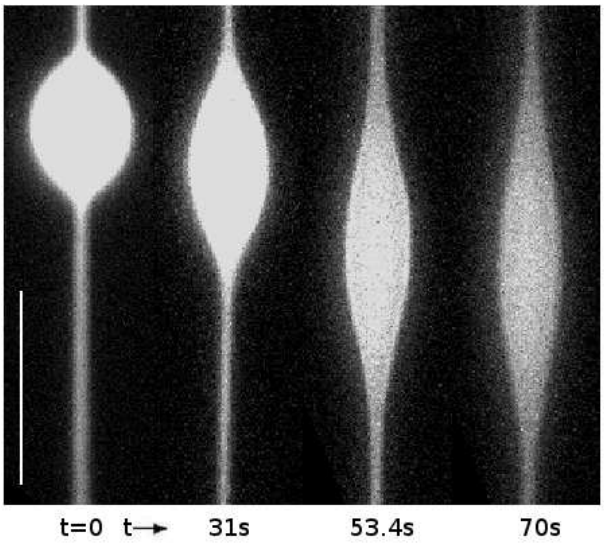

Figure 2.19: Scale bar = 20μm.

2.6.2.5 Coalescence of beads

Some MLTs have multiple beads. These approach each other and coalesce (Fig. 2.20). Beads of different size approach each other at different speed; smaller beads move faster towards larger beads and coalesce. Some larger beads are stationary and fatten by swallowing up smaller beads on the same MLT (movies 2.6.2.5). By sealing the sample-cell, coalescence of beads on the same MLT is not arrested but bead formation from the reservoir end stops.

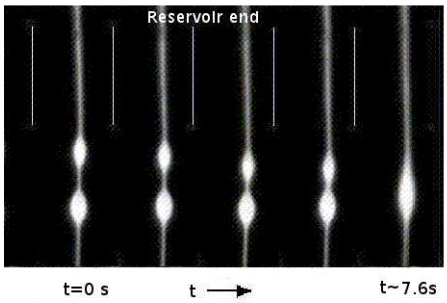

(a)

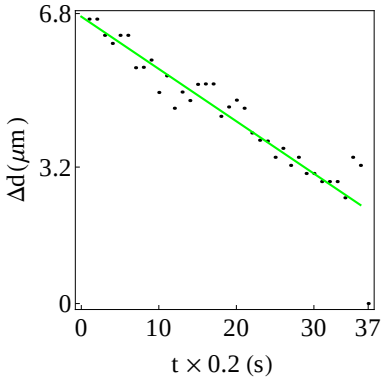

(b) $\Delta d = 6.73 - 0.123\,t$.

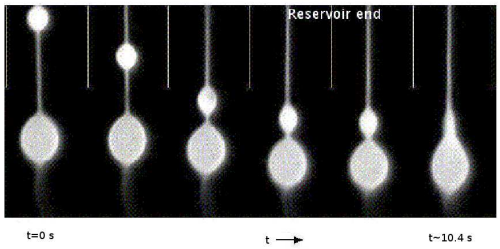

(c)

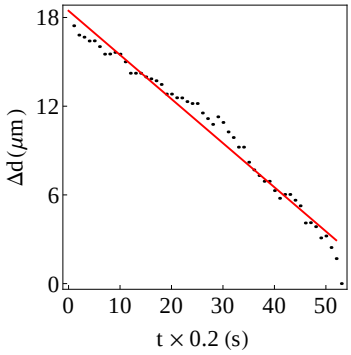

(d) $\Delta d = 18.45 - 0.298\,t$.

Figure 2.20: Δd is the distance between two beads, scale bar = $20\,\mu$m.

2.7 Discussion

It is quite clear that the nonequilibrium morphology of the structures discussed, as well as the dynamics of the process leading to these are very complex and diverse. Because of the complexity of the observed phenomena it is not possible to precisely state the causes leading to the burst. However, some general conclusions can be drawn from our observations.

It is of interest to note that the stability of the cylindrical tubular structures such as myelins (over a considerably long period) is not yet fully understood [13]. The terminology "myelins" is used somewhat loosely in the literature. In this thesis, we use the term multilamellar tubules to avoid possible confusion. In what follows we describe a possible scenario leading to the burst.

At first lipid molecules self-assemble to form a fluid bilayer stack and attain maximum swelling over a long time scale [14]. In the much slower next step the maximally swollen lamellar stack is brought in contact with excess water, so that the lipid film starts to disperse in water in the form of various structures made up of bilayers (Fig.2.7a). This is followed by the burst. We note that evaporation of the solvent plays an important role in the initiation of the burst (Figs.(2.10) and (2.11)). In the language of phase separation kinetics, we make a deep quench across the first-order phase boundary to a phase where swollen lamella coexist with excess water.

The fact that the instability does not occur in spin-coated samples (which are of uniform thickness, in contrast to syringe-coated ones) suggests that the tubules emerge from defects (such as dislocation loops, holes, *etc*.) on the lamellar stack. Growth of tubules in the lipid reservoir has been previously reported [15, 16]. The thickness of the lipid film is not uniform and the lamellar stack has a large number of defects. Thus what we have is essentially a sample full of defects in the fluid lamellar phase with syringe-coated samples., and not a well-defined microstructure of uniform thickness. This explains the occurence of instability

only in syringe-coated samples. That the tubular instability originates from defects on the lamellar sample is further corroborated by images in the Fig.2.10.

The defects locally enhance permeation, and the excess water can cause local unbinding of the layers. This leads to a gradient in tension between reservoir-bound and the unbound parts of the membranes, which in turn causes rapid flow towards the unbound region. These stresses can be relieved by a tubular instability, although the causes for the burst instability are different from discussed in [17].

We believe that the beads are also caused by local dynamic change in tension. In Chapter 5, we show that the solvent cores of beads have diameters different from the core-diameters of the tubues on which they reside. This lends support to the hypothesis that the beads also have a structure which is teeming with defects, particularly near the neck joining the tubule.

There is a large variation in the relatively rapid linear growth and retraction rates of MLTs (ranging from 1 to 40 μ m/s). These rates depend upon the nature of the MLT, and on the environment (such as lipid and solvent supply) in the vicinity of the reservoir-end of the MLT. Coalescence (Fig.2.20) and dispersion (Fig.2.19) of beads is usually a slower process as compared to the growth and retraction of MLTs. These dynamical phenomena are very complex (Figs.2.15c and 2.16). In the chapters to follow, our focus is on morphological studies rather than on the dynamical properties.

In our view, it would be fair to state that the interplay between elasticity, defects and flow plays a major role in initiating the burst as well as the bead formation instabilities.

Bibliography

[1] H. Diamant, M. E. Cates, Eur. Phys. J. E 4, 223 (2001).

[2] M. Buchanan, J. Arrault and M. E. Cates, Langmuir 14, 7371 (1998).

[3] M. Buchanan, S. U. Egelhaaf, and M. E. Cates, Langmuir , 16 (8), 37183726, (2000).

[4] James Pawley, *Handbook of Biological Confocal Microscopy* (Springer, 3rd edition, 2006).

[5] Jean-Baptiste Sibarita, Adv Biochem Engin/Biotechnol, 95, 201-243, (2005).

[6] Torleiv Orhaug, Optica Acta., Vol. 16, No. 1, (1969), 75-84.

[7] Falconi, J. Opt. Soc. Am. 54, 1315 (1964).

[8] David L. Fried, J. Opt. Soc. Am., Vol. 69, No. 3, (1979)

[9] G. S. Downs and P. E. Reichley, The Astrophysical Journal Supplement Series 53, 169-240 (1983).

[10] V. J. Morris, A. R. Kirby and A. Patrick Gunning, *Atomic Force Microscopy for Biologists* (Imperial college press, 1999).

[11] U. Mennicke and T. Salditt, Langmuir 18, 8172 (2002).

[12] Seul and Sammon, Thin Solid Films 185, 187-305 (1990).

[13] Santangelo CD, Pincus P., Phys. Rev. E 66, 061501 (2002).

[14] Pabst, G., J. Katsaras, V. A. Raghunathan, and M. Rappolt. Structure and interactions in the anomalous swelling regime of phospholipid bilayers. Langmuir 19, 1716 - 1722 (2003).

[15] Ling-Nan Zou and Sidney R. Nagel, Phys. Rev. Lett. 96, 138301 (2006).

[16] Ling-nan-Zou, Phys. Rev. E 79, 061502 (2009).

[17] R. Bruinsma, J. Phys. II 1 (8), 995-1012, (1991).

Chapter 3

Modeling FCM images

In this chapter we propose a model to calculate the FCM intensity profile of tubules which are roughly cylindrical in shape. The simplest tubules have a single core. The model has four fitting parameters; the inner and outer radii of the tubule, the confocal slice thickness, and a scaling factor which is related to the lipid density. We show that in devising the model it is essential to account for total internal reflection at the solvent - lamella interfaces, whereas the birefringence of the lamellar structure can be safely ignored. A straightforward generalization of this model can be used to analyze the more complicated structures such as asymmetric tubules, and central sections (the region near the maximum bulge) of beads.

In what follows we set up the model and compare its performance against hypothetical intensity data which is free of noise. In this process we establish the proper procedure to analyze experimental data. Real images are of course contaminated with noise. This aspect (image processing) is discussed in Chapter 4. The method we follow is designed to glean as much information as possible from FCM images.

To our knowledge detailed FCM studies of the kind reported in this thesis have not been made.

3.1 Fluorescence intensity detected from a voxel

The fluorescence intensity detected per unit confocal volume $I_D \propto I_e f_V$, where I_e is the total fluorescence intensity of light emitted isotropically from all excited dye molecules per unit confocal volume, and f_V is the fractional confocal volume from which rays enter the objective.

Let us consider a uniform cylindrical tubule of outer radius r_o and core radius r_c with its axis along $\hat{x}$ (Figs.3.1).

(a) (b)

Figure 3.1: Sections of a simple (single-core) tubule.

Let $\hat{l}, \hat{d}_a$ and $\hat{d}_e$ respectively denote the unit vectors parallel to the long axis, absorption and emission transition dipole moments of the dye molecule. For the dye molecules $\hat{l} = \hat{r} = (0, \cos\theta, \sin\theta)$, $\hat{d}_a$ and $\hat{d}_e$ are in a plane perpendicular to $\hat{r}$, as discussed in section 1.3. Thus the Cartesian molecular frame of reference is $(\hat{x}, \hat{r} \times \hat{x}, \hat{r})$. We define $\cos\phi_1 = \hat{d}_a \cdot (\hat{r} \times \hat{x})$ and $\cos\phi_2 = \hat{d}_e \cdot (\hat{r} \times \hat{x})$. Thus

$$\hat{d}_a = \cos\phi_1 \hat{x} + \sin\phi_1 \sin\theta \hat{y} - \cos\theta \sin\phi_1 \hat{z}, \tag{3.1}$$

$$\hat{d}_e = \cos\phi_2 \hat{x} + \sin\phi_2 \sin\theta \hat{y} - \cos\theta \sin\phi_2 \hat{z}, \tag{3.2}$$

The incident laser beam is linearly polarized with $\hat{E}_i = \cos\psi \hat{x} + \sin\psi \hat{y}$. In our experiments we use giant unilamellar vesicles (GUVs) to determine $\hat{E}_i$ (Fig.3.2).

The probability that an incident photon is absorbed by a dye molecule $P_a \propto I_0\langle(\hat{d}_a \cdot \hat{E}_i)^2\rangle$, where the angular brackets denote the average over ϕ_1 (since all possible orientations of the dye molecule are equally likely), and I_0 is the normalized intensity of the incident beam. The fluorescence intensity detected is $I_d \propto P_a f_V$, where f_V is the fractional confocal volume. The confocal slice Δ_z contains a large number of fluorescent molecules. Fig.3.3 shows the *yz*-section of the tubule.

In order to obtain the detected intensity we divide Δ_z into hypothetical blocks of width equal to the pixel width in the *xy*-plane and sum the intensities from each of these blocks.

3.1.1 Calculation of f_V and ray tracing

We consider a sphere of unit radius centred at P (Fig. 3.4). In the absence of any refractive index mismatch between the objective and the sample, $f_V = \int_0^{2\pi}\int_0^{\delta_{max}} \sin\delta\, d\delta\, d\phi$. We need to modify this to account for the different refractive indices of the cover slip (n_c), solvent (n_s), and the lamellar structure (n_l). For the sake of simplicity, we consider uniformly spaced lamellae and assume n_l = constant. In addition, we need to account for total internal reflection at lamella - solvent interfaces. We have written a computer code to compute f_V based upon the above considerations (which, although straightforward, are tedious to implement). In what follows, we discuss the roles of birefringence and total internal reflection in devising our model.

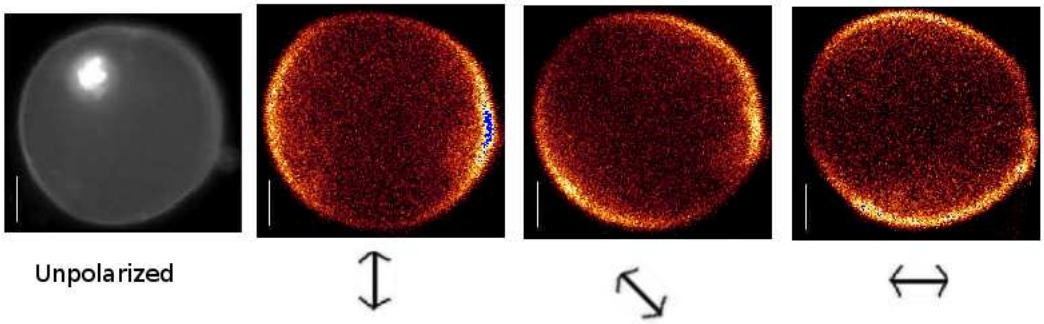

Figure 3.2: Arrows indicate $\hat{E}_i$, Scale bar = 20μm.

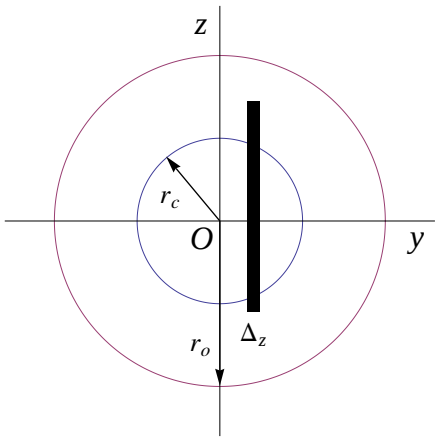

Figure 3.3: r_c, r_o, and Δ_z denote the core radius, the outer radius, and the confocal slice thickness respectively.

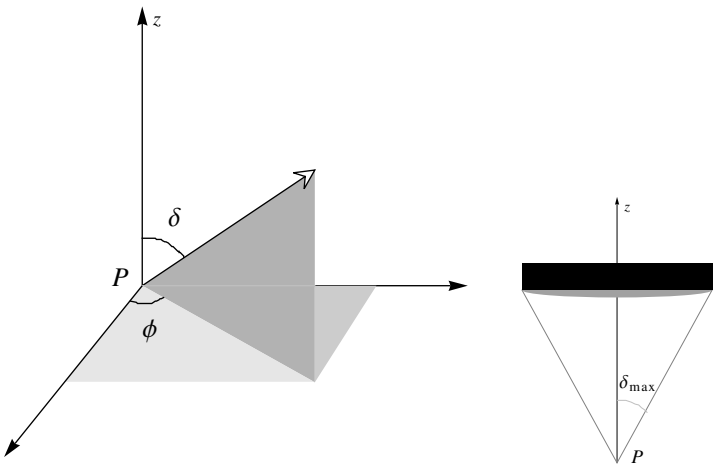

(a) (b)

Figure 3.4

3.1.1.1 Refractive index of the lamellar phase

Since the concentration of the dye is small, we can safely ignore the contribution of dye molecules to the lamellar refractive index. As discussed in [1], ordinary refractive index of the lamellar phase decreases linearly with increase in the solvent volume fraction. The ordinary refractive index of DOPC lamellar phase $n_{lo} = n_o\phi_l + n_s\phi_s$, where n_o and n_s are respectively the ordinary refractive index of DOPC and the refractive index of the solvent, and ϕ_l and ϕ_s stand for the volume fractions of the lipid and solvent. DOPC has positive birefringence with $\Delta n \simeq 0.026$ [2]. The effective refractive index n_l of the lamellar phase

[3, 4, 5] is

$$\frac{1}{n_l^2} = \frac{\cos^2 t}{n_{\text{le}}^2} + \frac{\sin^2 t}{n_{\text{lo}}^2}, \tag{3.3}$$

where n_{lo} and n_{le} are respectively the ordinary and extraordinary refractive indices of the lamellar phase, and $\cos t = \hat{E}_{\text{i}} \cdot \hat{r}$. We discuss the effect of ignoring birefringence in section 3.2.3.

3.1.1.2 Total internal reflection (TIR) at the lamella - solvent interface

Rays incident on both inner as well as outer lamella - solvent interfaces undergo TIR if the angle of incidence exceeds the critical angle θ_c. Moreover, a ray can bounce off the inner interface, undergo refraction at the outer interface and reach the objective. To compute f_V, we need to trace the rays emanating from a point P in the lamellar bulk and account for only those rays which reach the objective. Although essential for the computation of f_V, ray tracing is somewhat tedious when TIR is taken into account. The effect of ignoring TIR are discussed in section 3.2.4. In order to simplify the discussion, we first consider the *yz*-cross-section of the tubule at $x = 0$ (Fig. 3.5), and then consider rays not restricted to the *yz*- plane.

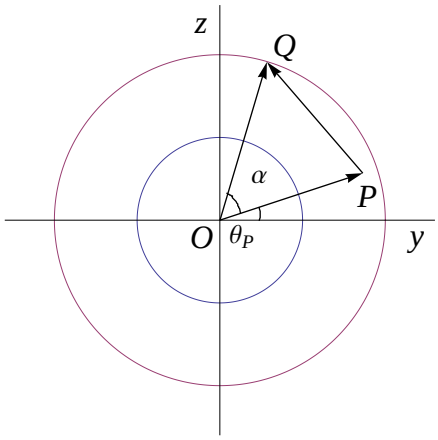

Figure 3.5

The unit vector along OP is $\hat{r}_{\text{P}} = (0, \cos\theta_{\text{P}}, \sin\theta_{\text{P}})$. The rays $\hat{R}_{\text{PQ}}$ emanating from P and lying in the *yz*-plane can be represented as $\hat{R}_{\text{PQ}} = (0, \cos(\theta_{\text{P}} + \alpha), \sin(\theta_{\text{P}} + \alpha))$. The angle

of incidence θ_i is given by the relation $\cos\theta_i = \hat{R}_{\mathrm{PQ}} \cdot \hat{n}_Q$, where $\hat{n}_Q = (0, \cos\theta, \sin\theta)$ is the unit normal to the interface at Q (which always lies in the *yz*- plane). The condition for TIR ($\theta_i \geq \theta_c$) can then be tested and the ray- path traced further.

For rays not necessarily lying in the *yz*- plane, $\hat{R}_{\mathrm{PQ}} = (\cos\theta\cos\phi, \cos\theta\sin\phi, \sin\theta)$ (note that these are not the standard spherical polar coordinates, in particular, θ is the complement of the usual azimuthal angle used in spherical polar coordinates) with $0 \leq \phi \leq 2\pi$. As before, the angle of incidence is defined via $\cos\theta_i = \hat{R}_{\mathrm{PQ}} \cdot \hat{n}_Q$.

With these considerations in mind, straightforward use of the laws of reflection and refraction gives us the dependence of the angle of the marginal rays on the position of the point *P*. We take successive *z*- scans with sampling widths Δ_x, Δ_y such that we oversample the object of interest (in this instance, the tubule). Because of aberration caused by the refractive index of the medium and the shape (curvature) of the tubule, $\Delta_z \neq d_z$, furthermore, the shape-aberration in the *xy*- plane is less than that along *z* [6]. Therefore, in addition to r_{c} and r_{o} we include Δ_z as an additional fitting parameter in our model.

Aberration due to curvature is the least when Δ_z is centered at the $z = 0$ plane. For this reason we use this *z*- scan to measure the radii of the tubule. Most objects of interest (simple tubules, multi-core tubules, beads, *etc.*) are not cylindrically symmetric. The manner in which we address the asymmetry is discussed in the section 3.2.1.

3.2 Assessment of the model using hypothetical intensity profiles

In order to gauge the performance of the model we check it against hypothetical intensity profiles (Figs. 3.6) which are free of noise. We test the model for the (*i*) effect of birefringence, and (*ii*) effect of total internal reflection (TIR).

In contrast to hypothetical profiles, real images are not cylindrically symmetric, and are polluted with noise. The analysis of hypothetical intensity profiles allows us to formulate

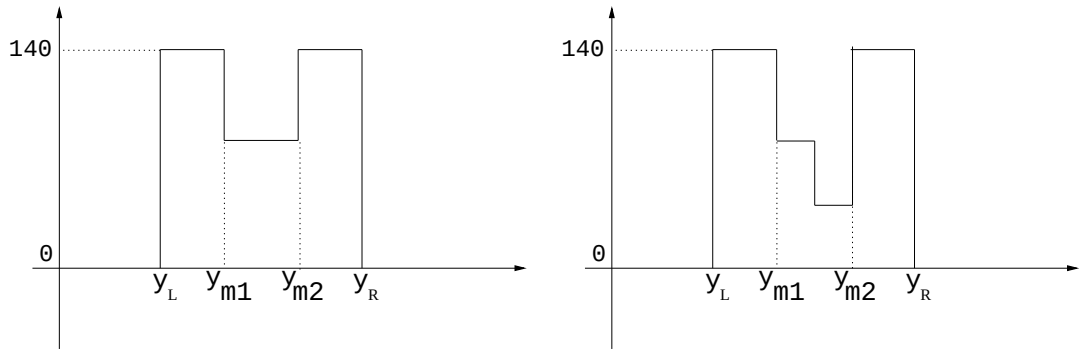

(a) Symmetric hypothetical data. (b) Asymmetric hypothetical data.

Figure 3.6

the standard procedure that we adopt to analyze real intensity data. In what follows we first discuss the determination of the symmetry axis of the intensity profile, followed by (*i*) and (*ii*), described above.

3.2.1 Determination of the symmetry axis of a tubule

The images of structures of interest (tubules, beads, *etc.*) are not rotationally symmetric about an axis. Shape as well as the density of molecules contribute to the asymmetry in the intensity profile. In order to optimize the position of the symmetry axis we first notice that scrutinizing the images obtained by changing the confocal slice thickness Δ_z gives us rough estimates of the position of the axis of symmetry as well as r_c, r_o, and Δ_z. This initial choice of the symmetry axis allows us to divide the image into two halves, right (R), and left (L). Using the initial choices for the symmetry axis and the confocal slice thickness we maximize the intensity cross-correlation function (overlap function) discussed below.

For the sake of simplicity we first restrict ourselves to the discussion of simple tubules, *i*.e. those with a single core. The analysis of the more complicated structures is a straightforward generalization of the procedure discussed above section 3.3. The intensity cross-correlation function is defined as $\phi_(j, r_c, r_o, \Delta_z) = \sum_{k=1}^{N} I_L(j+k, r_c, r_o, \Delta_z) I_R(k, r_c, r_o, \Delta_z)$, where j is the pixel number corresponding to the initial choice for the symmetry axis, N is the number of pixels in each half, after padding the profile with pixels with zero intensity so that both halves

of the intensity profile have the same number of pixels, I is the intensity (the subscripts L and R stand for folded left half and right half respectively with the initial choice of the symmetry axis) . The "symmetry axis" of the intensity profile is then positioned at $j = j_0$ at which $\phi_(j, r_c, r_o, \Delta_z)$ is maximum (Fig. 3.7).

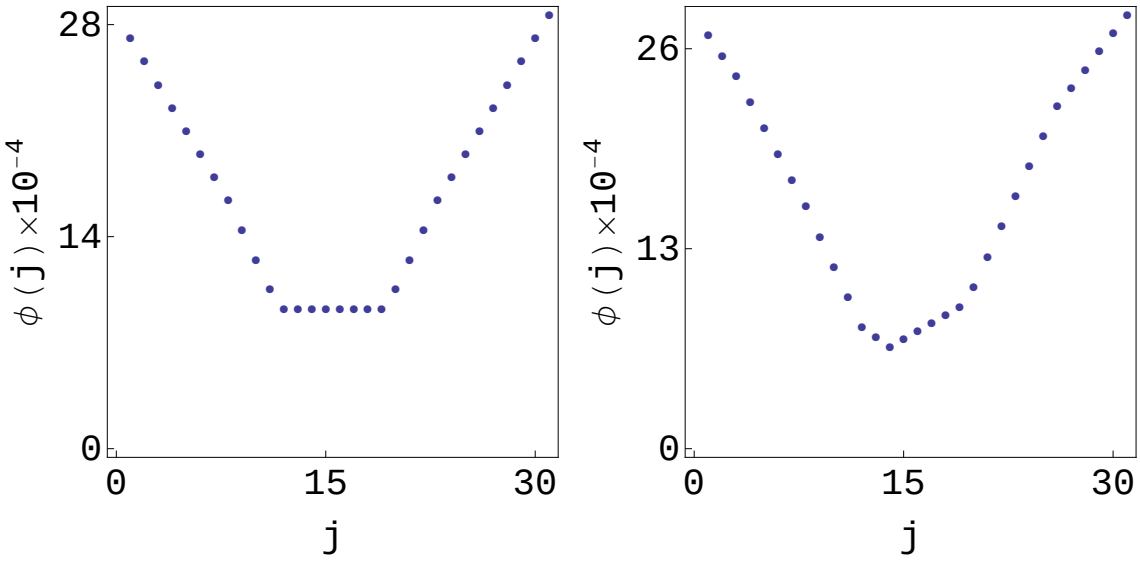

(a) For symmetric data. (b) For asymmetric data.

Figure 3.7: Cross-correlation function $\phi_(j, r_c, r_o, \Delta_z)$.

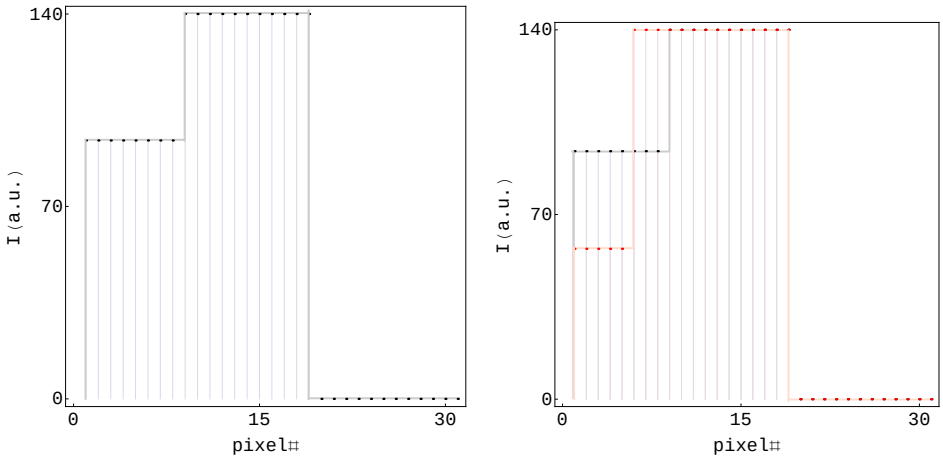

(a) For symmetric data. (b) For asymmetric data.

Figure 3.8: Folded left (L) (black) and right (R) (red) halves of the hypothetical data with the symmetry axis given by maximum of the cross-correlation function.

To assess the result of cross-correlation, we plot the folded left-half and right half on top of each other (Fig. 3.8) after finding the symmetry axis. Determination of the symmetry axis of the structure gives us estimates of the core radius r_c, the outer radius r_o, and the confocal slice thickness Δ_z. Using these estimates as initial values in the model yields the model intensity profile $I_M(i)$.

3.2.2 Further analysis of the intensity data

We evaluate

$$\chi^2(\alpha, r_c, r_o, \Delta_z) = \sum_{i=1}^{N} [I_O(i) - \alpha I_M(i, r_c, r_o, \Delta_z)]^2, \tag{3.4}$$

where $I_O(i)$ is the observed intensity profile. The best fits (Fig. 3.9) are obtained by minimizing $\chi^2(\alpha, r_c, r_o, \Delta_z)$ with respect to the parameters of the model α, r_c, r_o, and Δ_z). In the analysis of real, noisy data

$$\chi^2(\alpha, r_c, r_o, \Delta_z) = \frac{\sum_{i=1}^{N} (1/\sigma_i^2)[I_O(i) - \alpha I_M(i, r_c, r_o, \Delta_z)]^2}{\sum_{i=1}^{N} (1/\sigma_i^2)}, \tag{3.5}$$

where σ_i^2 is the noise variance (see Chapter 4) associated with each pixel.

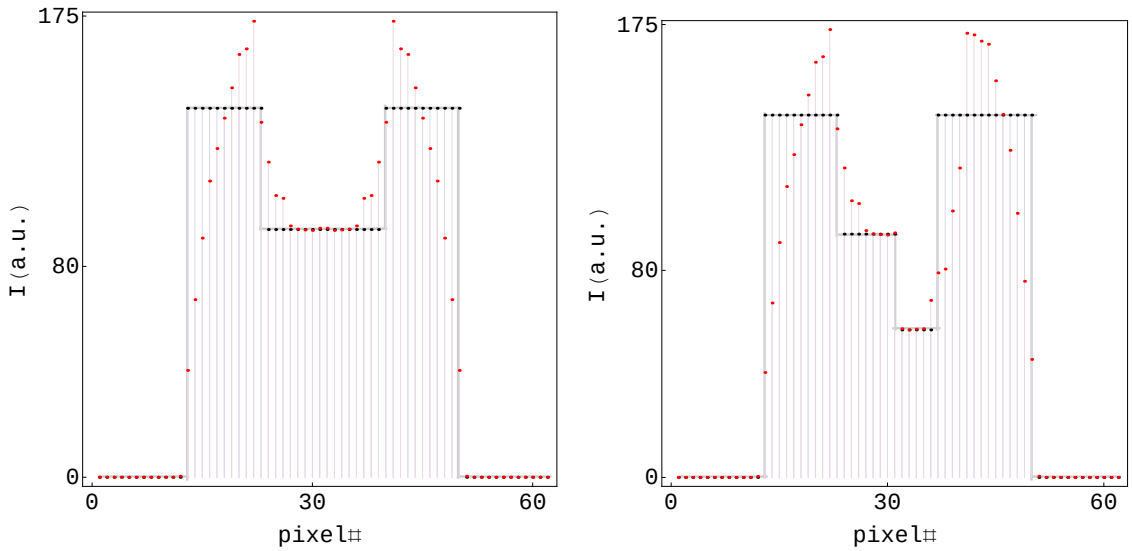

(a) $\alpha \simeq 173$, $\Delta_z = 50$ pixels.

(b) $\alpha_L = 1.003\alpha_R$, $\Delta_z = 50$ pixels for left half and $\Delta_z = 30$ pixels for right half.

Figure 3.9: Hypothetical data (black), best fit model intensity profile $I_M(i)$ (red), $r_c = 10$ pixels, $r_o = 20$ pixels and $\alpha_L \simeq 173$.

We note that the parameter α is a measure of the density of the fluorescent dye molecules, which in turn depends upon the lamellar spacing. However, α does depend upon Δ_z, and it is not possible to cleanly separate the shape- asymmetry from that due to asymmetry in density from the observed intensity profiles (although this can be done for the simple hypothetical intensity profiles discussed here).

3.2.3 Effect of birefringence of dye molecules

For $\psi = 0$ birefringence has no effect. Fig.3.10 demonstrates that for $\psi = \pi/2$, the change in the calculated fluorescence intensity due to birefringence is small. Moreover, ignoring birefringence does not lead to significant errors in determining r_c and r_o. Thus the effect of birefringence can be safely ignored.

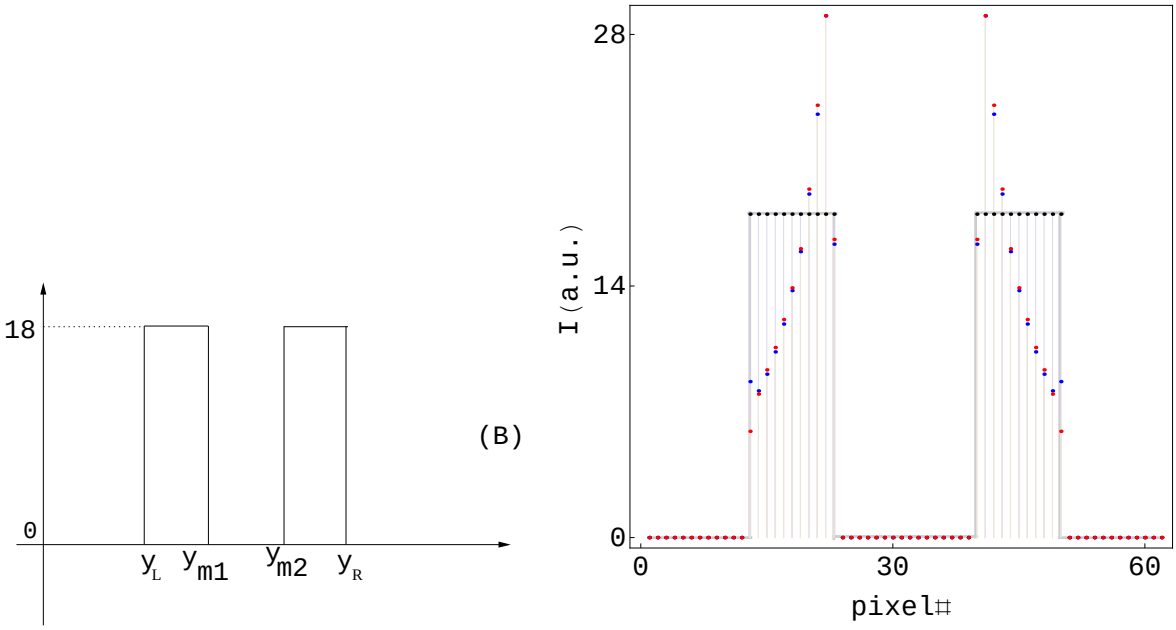

(a) hypothetical data

(b) $\Delta_z = 10$ pixels, $r_c = 10$ pixels, $r_o = 20$ pixels and $\alpha \simeq 29$.

Figure 3.10: Best fit considering birefringence (red), without birefringence (blue) with hypothetical data (black).

3.2.4 Effect of total internally reflected rays

The rays that undergo total internal reflection (TIR) at the core interface can enter the objective if these do not undergo TIR again at the cylinder outer solvent-lamella interface. Figs.3.11 show that the core diameter increases when TIR at the core interface is not taken into account. Thus it is essential to incorporate the effect of TIR at the interfaces in setting up the model, particularly for detecting features such as very small r_c.

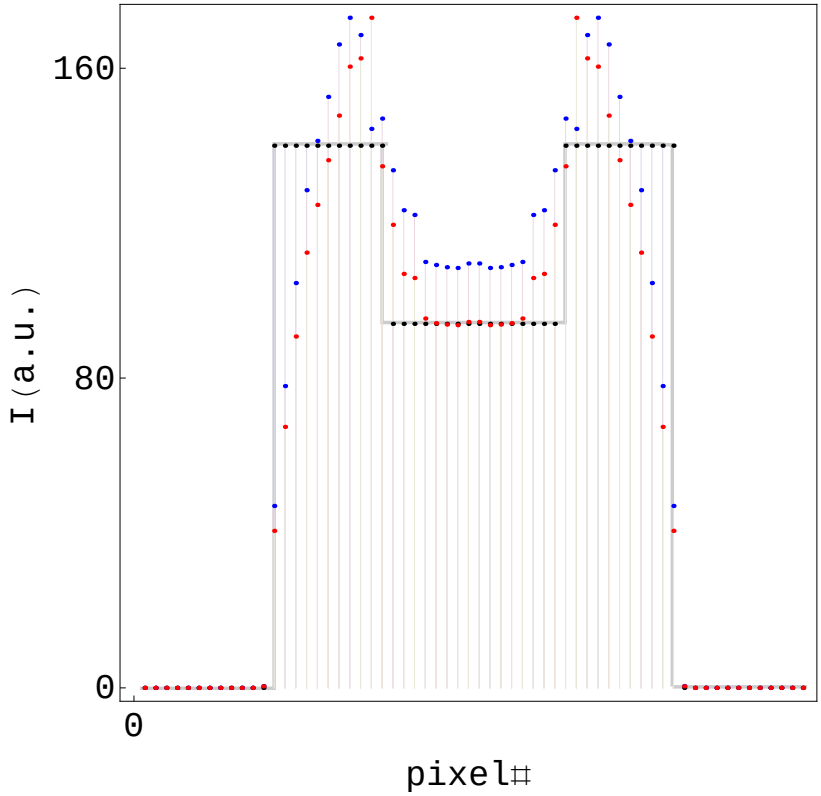

Figure 3.11: Best fit considering TIR (red), without TIR (blue) with the hypothetical data (Fig. 3.6(a)). The peak to peak distance for the blue curve is increased by 4 pixels compared to the red curve. r_c = 10 pixels, r_o = 20, Δ_z = 50 pixels and $\alpha \simeq 173$.

3.2.5 Effect of changing d_z in the model

Fig.3.12 show the effect of changing d_z by 20 pixels in the model.

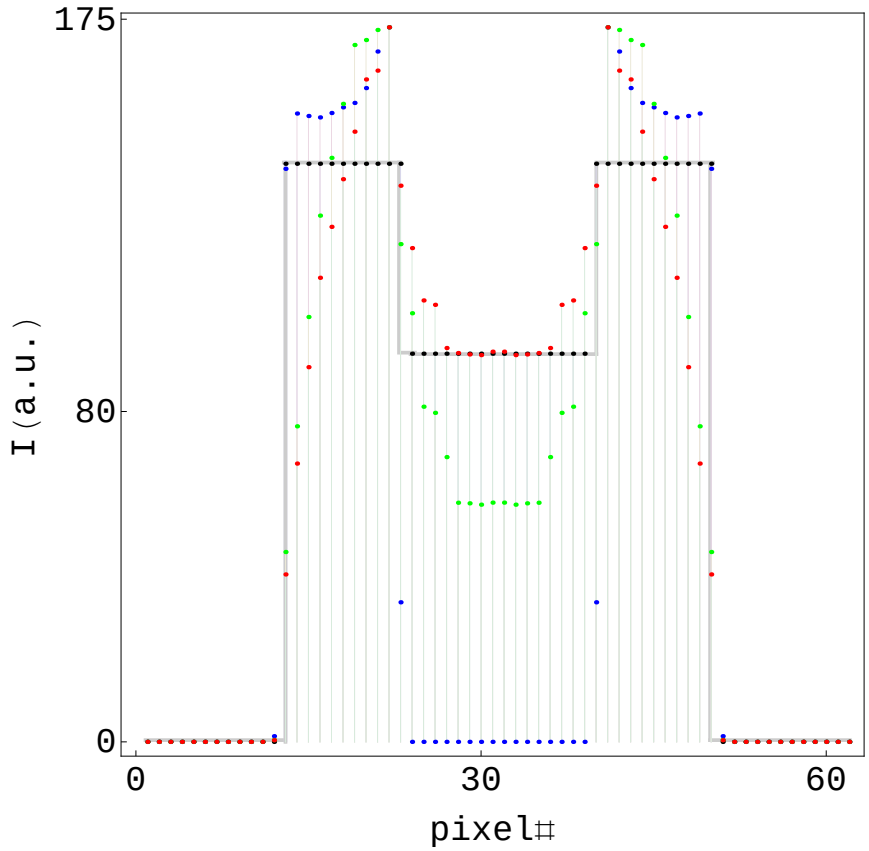

Figure 3.12: Hypothetical data (black), $\Delta_z = 50$ pixels (red), $\Delta_z = 30$ pixels (green) and $\Delta_z = 10$ pixels (blue) with $r_c = 10$ pixels, $r_o = 20$ pixels and $\alpha \simeq 173$.

3.3 Modeling multiple tubules

A multi-lamellar tubule consists of q number of tubules within and can be modeled as $\mathrm{I_m} = \left(\rho_1 \mathrm{I_{m1}} + \rho_2 \mathrm{I_{m1}} + ... + \rho_q \mathrm{I_{mq}}\right)$ where $\mathrm{I_{mk}}$ and ρ_k are the intensity and density of lamella for the k^{th} tubule. We estimate $\chi^2 = \sum_{i=1}^{\mathrm{N}} (1/\sigma_i^2)\left[\left(\alpha_1 \mathrm{I_{m1}^i} + \alpha_2 \mathrm{I_{m2}^i} + ... + \alpha_q \mathrm{I_{mq}^i}\right) - \mathrm{I_e^i}\right]^2 / \sum_{i=1}^{\mathrm{N}} (1/\sigma_i^2)$, where σ_i^2 is the variance [7] of the noise (see Chapter 4). By minimizing the χ^2 with respect to all the α_q we get q simultaneous equations in q variables which in matrix form can be written as;

$$\begin{pmatrix} \mathrm{x_{11}} & \mathrm{x_{12}} & \cdots & \mathrm{x_{1q}} \\ \mathrm{x_{21}} & \mathrm{x_{22}} & \cdots & \mathrm{x_{2q}} \\ \vdots & \vdots & \vdots & \vdots \\ \mathrm{x_{q1}} & \mathrm{x_{q2}} & \cdots & \mathrm{x_{qq}} \end{pmatrix} \quad \begin{pmatrix} \alpha_1 \\ \alpha_2 \\ \vdots \\ \alpha_q \end{pmatrix} \quad = \quad \begin{pmatrix} \mathrm{C_1} \\ \mathrm{C_2} \\ \vdots \\ \mathrm{C_q} \end{pmatrix}$$

where

$$\mathrm{x_{jk}} = \sum_{i=1}^{\mathrm{N}} \mathrm{I_{mj}^i I_{mk}^i}$$

$$\mathrm{C_j} = \sum_{i=1}^{\mathrm{N}} \mathrm{I_e^i I_{mj}^i}$$

Solving for q variables gives scaling for the q tubules for minimum χ^2. α_q is the intensity scaling of individual tubules such that α_q is a function of (ρ_q).

3.4 Discussion

We have proposed a simple model to calculate fluorescence intensity profile of a tubule as observed in the FCM. The nature of the intensity profiles obtained for the hypothetical data closely resembles the observed intensity data shown in the Chapter 5. Our model can successfully detect a core smaller as well as larger than d_z. Incident beam is linearly polarized and fluorescence intensity is collected from all the excited molecules with all polarizations. Confocal volume can change due to birefringence of molecules. We find that the change in the calculated fluorescence intensity due to birefringence is very small and therfore we can neglect it for data analysis. It is important to consider rays that are reflected at the core interface to find the correct intensity profile around the core.

Bibliography

[1] R. Gomati, M. Gharbia and A. Gharbi, Optics Communications, 111, 71-74 (1994).

[2] Lennart B. A. Johansson, Bjrn Kalman, Gran Wikander, ke Fransson, Krister Fontell, Bjrn Bergensthl and Gran Lindblom, Biochimica et Biophysica Acta, 1149, 285-291 (1993).

[3] S. Ohki, J. Theoret. Biol. 19, 97-115, (1968).

[4] S. Ohki, J. Theoret. Biol. 23, 158-168, (1969).

[5] S. Ohki, J. Theoret. Biol. 26, 277-287, (1970).

[6] T. D. Visser, J. L. Oud and G. J. Brakenhoff, Optik, 90 (1), 17-19, (1992).

[7] Philip R. Bevington and D. Keith Robinson, *Data Reduction and Error Analysis for The Physical Sciences* (McGraw-Hill, 3rd edition, 2002) .

Chapter 4

Image processing

4.1 Understanding noise in the measurements

Accurate quantitative analysis of image-data requires that we distinguish between the fluorescence intensity (true signal) and the noise inherent to its measurements [1, 2] to the extent possible. Understanding the nature of this noise also helps in optimizing image processing to detect features (such as very small cores) in the observed multi-lamellar objects, which would otherwise remain hidden.

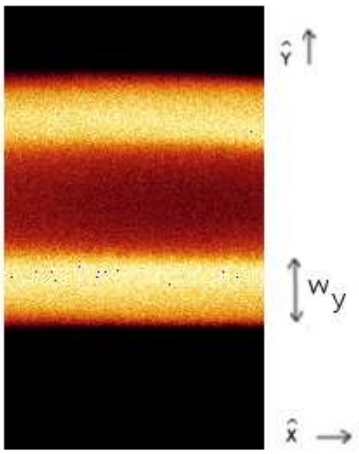

Figure 4.1: A uniform tubule with fixed r_c and r_o. The image size is (140×256) pixels, or $6.4\,\mu$m $\times$ $11.7\,\mu$m with sampling pixel width $\Delta x = \Delta y = 0.046\,\mu$m.

For simplicity, let us consider a uniform tubule (Fig.4.1). The observed fluorescence intensity $I(x,y)$ at a pixel location (x,y) has contributions from the entire confocal slice of thickness d_z. $I(x,y)$ shows significant structural variation along y for a fixed x, in contrast to

the very small variation along x for a fixed y. Hence we estimate the common intensity profile $\langle I(y)\rangle$ by averaging along x: $\langle I(y)\rangle = \sum_{j=1}^{N_x} I(x_j, y)/N_x$, with $N_x = 140$ in this case. Then intensity deviation from the mean, $I_{\mathrm{N}}(x, y) = [I(x, y) - \langle I(y)\rangle]$ gives the noise distribution across the image.

In confocal microscopy, noise contaminating the intensity measurement can be classified into three categories :

(i) Noise with its root-mean-square deviation (r.m.s.) proportional to $\langle I(y)\rangle$: The noise generated in system electronics falls into this class. It is also called the Johnson, Nyquist or thermal noise (σ_{t}), and originates from thermal random motion of charged particles within a material. The variance of this noise is proportional to the mean square fluorescence intensity: $(\sigma_{\mathrm{t}})^2 \propto \langle I^2(y)\rangle$ [3].

(ii) Noise with r.m.s. proportional to the $\sqrt{\langle I(y)\rangle}$: Photon counting noise, which arises from random fluctuations in photon arrival time at the detector, belongs to this class. It is also referred to as Poisson noise (σ_{p}) because the number of photons that arrive over a fixed period of time (given the mean) follows the Poisson distribution [4]. Photons associated with the true signal as well as those from the backround contribute to this noise. Thus variance of the Poisson noise is proportional to the observed mean fluorescence intensity: $\sigma_{\mathrm{p}}^2 \propto \langle I(y)\rangle$.

(iii) Noise which is independent of the fluorescence intensity: Dark noise (σ_{d}) which is the random signal produced by photosensitive devices such as PMTs, photodiodes, or CCDs (charge-coupled devices) in the absence of any incident signal falls into this class. Noise generated in the process of analog-to-digital conversion in the instrumentation also generates noise with this statistics. The variance of this noise is therefore independent of the fluorescence intensity; *i.e.*, σ_{d} = constant.

We estimate the variance of the fluctuations in fluorescence intensity $\sigma^2(y) = \sum_{j=1}^{N_x}[I(x_j, y) - \langle I(y)\rangle]^2/N_x$ in the image and perform minimum χ^2 fitting to assess the following dependences

on $\langle I(y)\rangle$ separately, namely $\sigma^2(y) = [a\langle I(y)\rangle + b]$ and $\sigma^2(y) = [c\langle I^2(y)\rangle + d]$ (Fig.4.2) with respective minimum χ^2 values χ^2_{lin} and χ^2_{sq}. The Poissonian noise model appears to fit the data better as $\chi^2_{\text{lin}} \simeq \chi^2_{\text{sq}}/2$ (Table4.1), although less dominant contribution from σ_t cannot be ruled out.

$\sigma^2(y) = a\langle I(y)\rangle + b$			$\sigma^2(y) = c\langle I^2(y)\rangle + d$		
a	b	χ^2_{lin}	c	d	χ^2_{sq}
2.3×10^{-3}	1.04×10^{-4}	2.8×10^{-6}	7.3×10^{-3}	1.43×10^{-4}	5×10^{-6}

Table 4.1

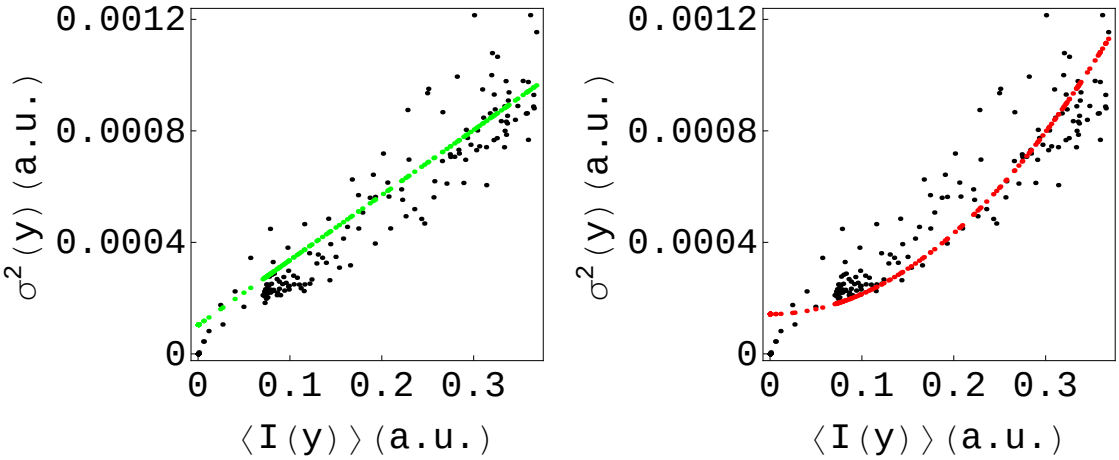

(a) Linear fit to noise variance.

(b) Quadratic fit to noise variance.

Figure 4.2

4.2 Image processing methods

As seen from our noise modeling, for cases in which Poission noise dominates, higher signal-to-noise-ratio SNR ($\propto \sqrt{\langle I(y)\rangle}$) is obtained at high values of fluorescence intensity. High SNR renders desired positional accuracy with which we can resolve features of interest [5]. We use the following image processing methods to improve SNR without smearing the details of features of interest. For example, one of the bright bands in the image (Fig.4.1) has a width $w_y \simeq 36\,\text{pixels} = 1.65\,\mu\text{m}$ with peak mean intensity $\langle I(y)\rangle \simeq 0.37$ (Fig.4.3(a)) and $\sigma(y) \simeq 0.007$ (Fig.4.3(b)). Thus the peak SNR of this particular feature is $\langle I(y)\rangle/\sigma(y) \simeq 53$.

We have improved the SNR of this feature upto 175 (Fig.4.5a) by using optimum smoothening. We describe the details of our procedures in the following Section.

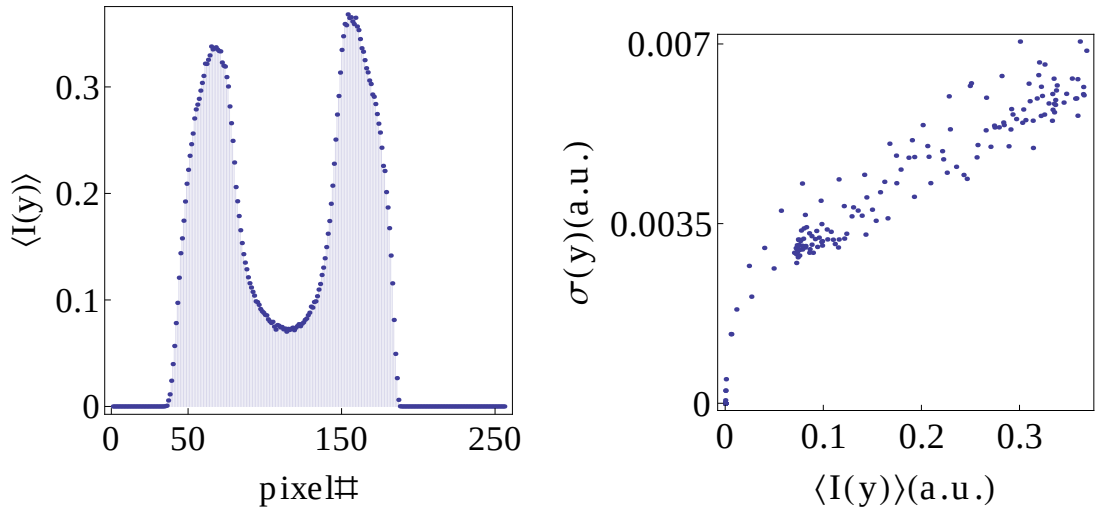

(a) $\langle I(y)\rangle$. (b) $\sigma(y)$ *vs.* $\langle I(y)\rangle$.

Figure 4.3

4.2.1 Optimum smoothening

In most, if not all, of our images, we have sampled some of the narrow features with adequate fineness. With this oversampling in our images we explore the possibility of smoothening the images optimally. The justification for this exploration stems from the fact that the random fluctuations in the observed intensities are uncorrelated from one pixel to another, and this implies a statistically uniform spread of noise across spatial frequencies, i.e. in Fourier domain of the data. Thanks to our finer than Nyquist sampling the Fourier components corresponding to the "signal " in our images are expected to be confined to lower spatial frequencies, as the signal features have width larger than spatial sampling interval. Hence, the noise in the higher spatial frequencies can preferentially be attenuated (without of course affecting the signal contribution), using suitable spatial frequency filter (low-pass), amounting to smoothening in the image domain. Although one could have increased the sampling interval after smoothening , we retain the images with their original sampling which offers advantage at the model fitting stage. We have used a 1−d Hann filter $H_{2n}(q_y) = \cos^{2n}(\pi q_y/q_{ys})$

for $|q_y| \leq q_{ys}/2$ and $H_{2n}(q_y) = 0$ for $|q_y| > q_{ys}/2$ in Fourier domain to smoothen our images where n is a positive integer, wherein the smoothening is optimized for a particular feature of interest (e.g. one of the bright bands in the image). This filter response smoothly goes to 0 at $|q_y| = q_{ys}/2$ and beyond. q_{ys} defines the extent of the Fourier domain window and corresponds to $m_q = (q_{ys}/\Delta_{q_y})$ spectral points (m_q is rounded off to nearest integer). We restrict our discussion to 1−d variation of the fluorescence intensity along y at fixed x. Let y_s be the scale of smoothening in the image domain (corresponding to q_{ys}) with $m = (y_s/\Delta_y)$ pixels (m is rounded off to nearest integer). For an image having N_y pixels (or data points) along y, the m and m_q are related as $m_q = (N_y/m)$. If Δ_{q_y} is the sampling width in the Fourier domain (where $\Delta_{q_y} = 1/[N_y\Delta_y]$), the window function at discrete values of q_y can be expressed as $H_{2n}(q_y = t_q\Delta_{q_y}) = \cos^{2n}(\pi t_q/m_q)$ for $|t_q| \leq m_q/2$ and 0 otherwise, where $t_q \in [-(N_y/2), (N_y/2) - 1]$. $H_2(t_q)$ and $H_4(t_q)$ are shown in Fig.4.4(a) for $m_q = 160$. In the image domain the associated smoothening function of $H_4(t_q)$ has lower side-lobe levels than for $H_2(t_q)$. This reduces possible "ringing "effect in the image, however the effective smoothening scale is relatively larger than for $H_2(t_q)$ for a given m_q.

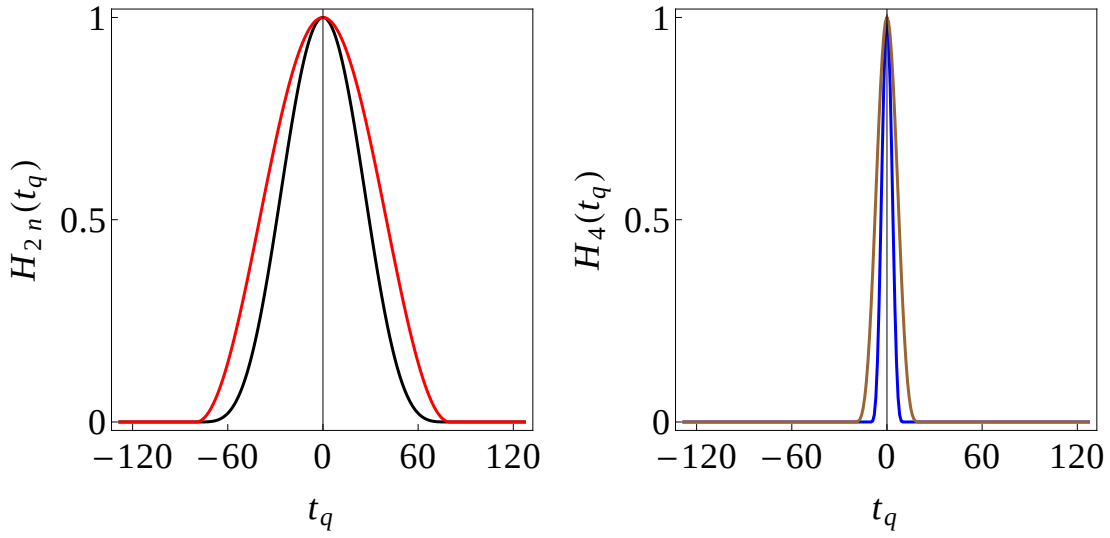

(a) $H_2(t_q)$ (red) and $H_4(t_q)$ (black) for $m_q = 160$.

(b) $H_4(t_q)$ plotted for $m = d_{yp}/2$ (brown), $m = d_{yp}$ (blue).

Figure 4.4

We have used $H_4(t_q)$ for Fourier domain windowing to smoothen our data. With $d_{yp} = d_y/\Delta y$ as the confocal psf width in pixels along y, Fig. (4.4(b)) show $H_4(t_q)$ for $m = d_{yp}/2$ and $m = d_{yp}$.

To assess the optimum smoothening scale for a given image or feature, we systematically vary trial values of m and examine the resultant SNR, as well as the profile. Fig.4.5a shows SNR as a function of m for a selected feature in a sample.

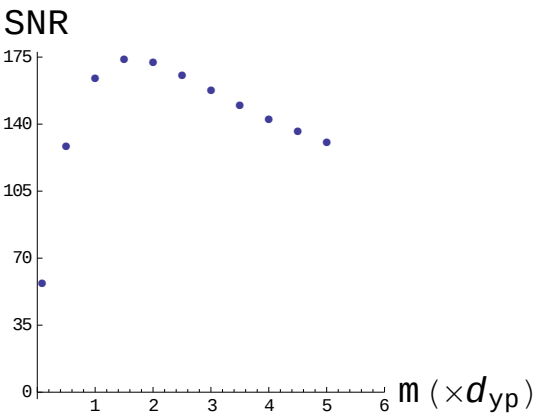

(a) SNR as a function of m.

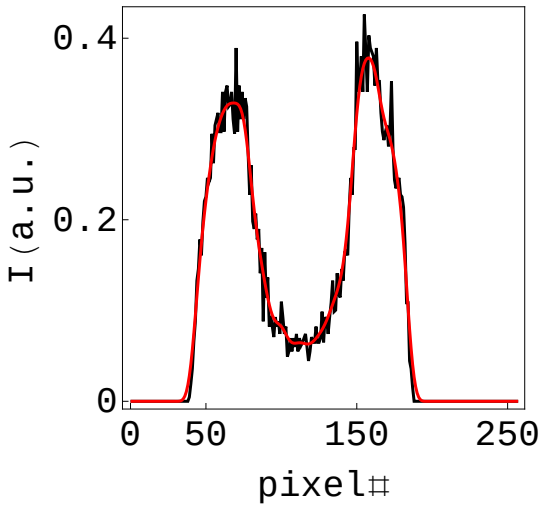

(b) $m = 0.5\ d_{yp}$ (red), raw image (black).

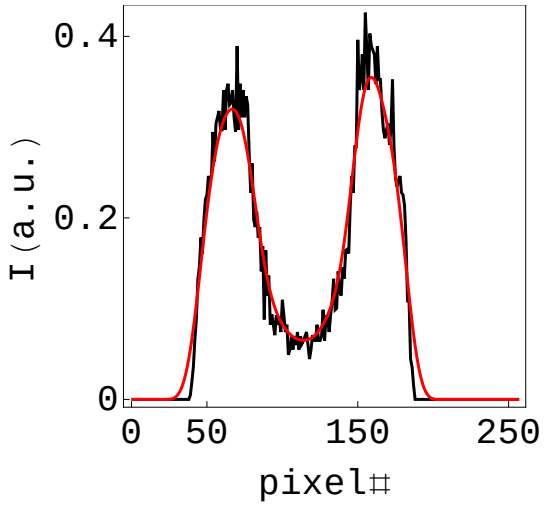

(c) $m = d_{yp}$ (red), raw image (black).

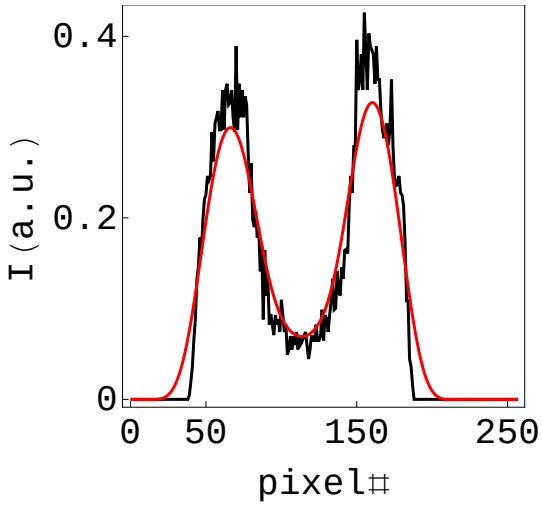

(d) $m = 1.5\ d_{yp}$ (red), raw image (black).

Figure 4.5

As we increase m, the SNR initially increases, reaches a maximum, and reduces due to excess smoothening of the feature. For the data shown in the plot (Fig.4.5a) we find that the best SNR$\simeq$ 175 for $m = 1.5\,d_{\mathrm{yp}}$. However, at the m suggested by maximum SNR, the smoothening smears the feature more than desired . Hence, at the expense of (i.e. with less) SNR we choose conservative smoothening, to retain the feature shape as intact as possible. For this purpose, we always compare the raw intensity profile of the tubule with the smoothened intensity profile (Fig.4.5 (b)-(d)). As can be seen, the peak (or knee) intensity of the selected feature starts to come down for $m > 0.5\,d_{\mathrm{yp}}$, and hence $m = 0.5\,d_{\mathrm{yp}}$ would be considered optimum for this feature, with SNR$\simeq$ 130.

We discuss below an image processing method that has the potential to correct for the blur caused by the microscope optics (during image formation) and the effect of these methods on the SNR of features of our interest. The results from application of these deconvolution methods were not used for further modelling etc., for reasons discussed in Section 4.2.2 and 4.3.

4.2.2 Deconvolution

Deconvolution in our context would involve correcting for the blur/spread (noise) caused by microscope optics in the process of image formation of an object and hence offers a way of recovering finer details in the images, which are otherwise lost due to available finite resolution of the measurements. The deconvolution operation requires adequate knowledge of the response of the measuring system (including optics etc.) which is often specified in terms of "point spread function"(psf). If a point object denoted by $\delta(\mathbf{r})$ (at $r = 0$) is imaged, the observed pattern would be so called psf, *i.e.,* $p(\mathbf{r})$ (Fig.4.6(a)). In general, for an object $f(\mathbf{r})$ the observed image is the convolution of the object with the psf, i.e. $h(\mathbf{r}) = f(\mathbf{r}) \otimes p(\mathbf{r})$ where $h(\mathbf{r})$ represents the image formed by microscope optics as a function of the position $\mathbf{r}$ (Fig.4.6). Given $h(\mathbf{r})$ and $p(\mathbf{r})$, the process of finding $f(\mathbf{r})$ is called **deconvolution**.

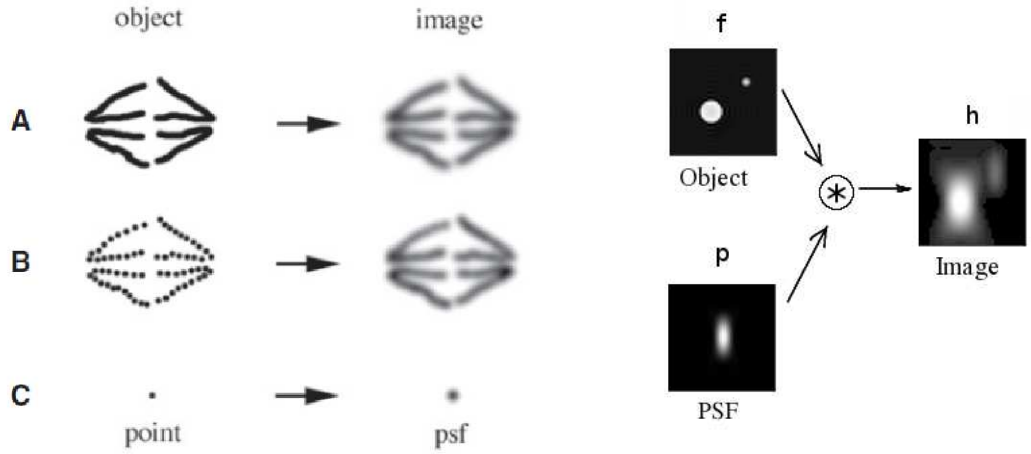

(a) Microscope image of a point and extended objects. Taken from [1].

(b) http://en.wikipedia.org/wiki/Point-spread-function. ⊛ denotes convolution

Figure 4.6

For the image (Fig.4.1) let $h(x_0, y)$, $f(x_0, y)$ and $p(x_0, y)$ respectively represent the 1−d "image" formed by microscope optics (before detection), object (tubule) and the psf as a function of the position y at fixed $x = x_0$, with their respective FTs denoted by $H(x_0, q_y)$, $F(x_0, q_y)$ and $P(x_0, q_y)$. In our case the psf along y does not depend on x therefore $p(x_0, y) = p(y)$ for all x. We discuss two methods of implementing deconvolution below.

4.2.2.1 Direct deconvolution

Direct deconvolution involves computing $F(x_0, q_y) = [H(x_0, q_y)/P(q_y)]$. FT of $F(x_0, q_y)$ yields $f(x_0, y)$. The difficulties in computing $F(x_0, q_y)$ are :

(i) The division $H(x_0, q_y)/P(q_y)$ cannot be performed blindly without assessing possible blowing up of noise at Fourier components for which $P(q_y) \to 0$,

(ii) In reality the detected image is $\tilde{h}(\mathbf{r}) = h(\mathbf{r}) + \eta$, where $h(\mathbf{r}) = f(\mathbf{r}) \otimes p(\mathbf{r})$ is the image formed by the microscope optics before it is detected and η is the noise (as described in the Section 4.1) contributed to the image subsequent to the microscope optics (Fig.4.7) and therefore has not undergone convolution. In Fourier domain we have $\tilde{H}(\mathbf{q}) = H(\mathbf{q}) + \eta_q$ where $\tilde{H}(\mathbf{q})$, $H(\mathbf{q})$ and η_q are respectively the FTs of $\tilde{h}(\mathbf{r})$,

$h(\mathbf{r})$ and η. Thus deconvolution operation amounts to computing $\tilde{H}(x_0, q_y)/P(q_y) =$

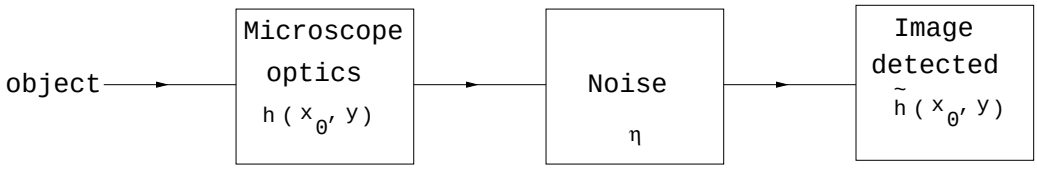

Figure 4.7

$[F(x_0, q_y) + (\eta_q/P(q_y))]$, and the noise η_q gets amplified even when $P(q_y)$ is not $\rightarrow 0$, in particular, for $P(q_y) < 1$.

4.2.2.2 Deconvolution using a low pass step-filter

To address some of the difficulties with direct deconvolution, we can use a one-step filter $S(q_y)$ (Fig.4.8) of width $2q_c$ such that we perform the division $\tilde{H}(x_0, q_y)/P(q_y)$ for $q \in [-q_c, q_c]$. q_c can be determined as follows. $S(|q_y| < |q_c|) = 1$ and $S(|q_y| > |q_c|) = 0$. If $\langle\tilde{H}(q_y)\rangle$ is the mean signal of the tubule as a function of q_y and $\sigma(q_y) =$

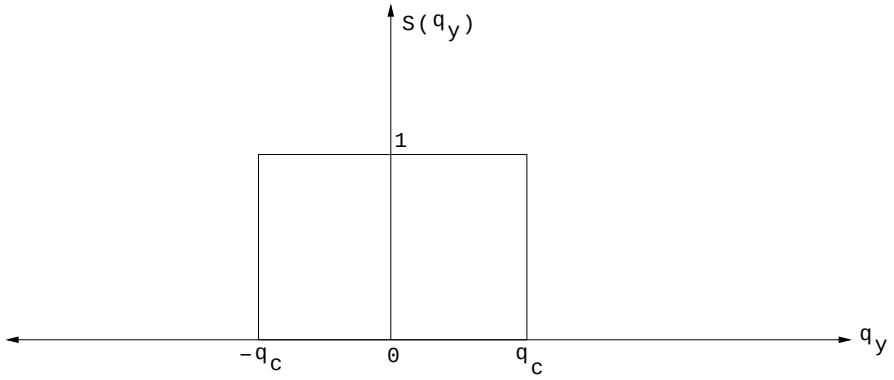

Figure 4.8: Low pass step-filter.

$\sqrt{\sum_{j=1}^{N_x}[\tilde{H}(x_j, q_y) - \langle\tilde{H}(q_y)\rangle]^2/N_x}$ is the r.m.s. value of noise as a function of q_y, then we determine the cut-off q_c at which $P(q_c) \rightarrow (|\sigma_{\max}|/|\langle\tilde{H}_{\max}\rangle|)$. In the illustrative example (Fig.4.1), we get $|\langle\tilde{H}_{\max}\rangle| \simeq 0.12$ (Fig.4.9(a)) and $|\sigma_{\max}| \simeq 0.0019$ (Fig.4.9(b)) giving $|(\sigma_{\max}|/|\langle\tilde{H}_{\max}\rangle)| \simeq 0.016$. $P(q_y)$ obtained from our calculation (described in Section 2.2) is shown in Fig.4.10. We estimate cut-off $t_{qc} = (q_c/\Delta_{q_y})$ such that $P(t_{qc}) = |(\sigma_{\max}|/|\langle\tilde{H}_{\max}\rangle|)$ which in our case gives $|t_{qc}| \simeq 11$.

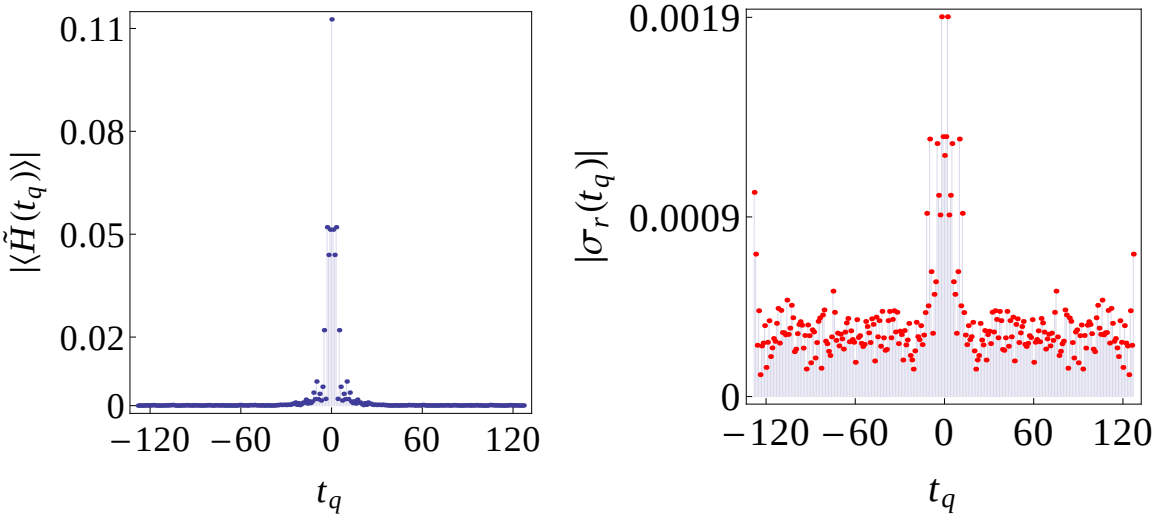

(a) (b)

Figure 4.9

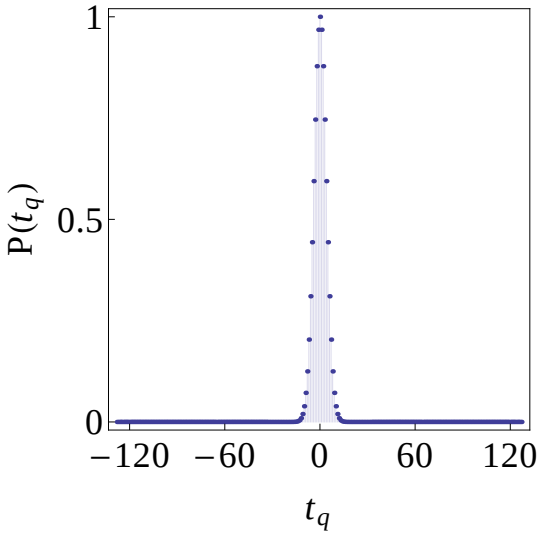

Figure 4.10: Point spread function in the Fourier domain with $d_{yp} \simeq 12$ pixels.

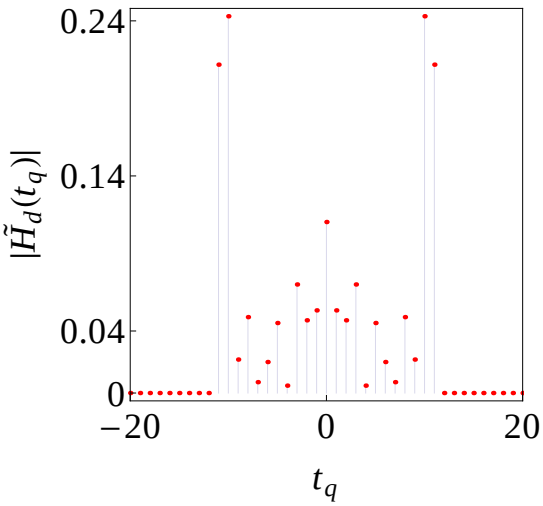

Figure 4.11: $|\tilde{H}_{\rm d}(t_q)|$ after deconvolution.

The $|\tilde{H}_{\rm d}(t_q)|$ (after deconvolution) as a function of t_q is shown in Fig.4.11. $|\tilde{H}_{\rm d}(t_q)|$ is high at $|t_{qc}| \simeq 11$. This happens because we perform the division $\tilde{H}(x_0, t_q)/P(t_q)$ upto $|t_{qc}|$. At $|t_{qc}|$, $|\tilde{H}_{\rm d}(t_{qc})|$ is enourmously high. One may opt for a smaller value of cut-off $|t_{qc}|$ (larger $P(t_{t_{qc}})$), or consider conservative windowing rather than the sharp truncation, while still retaining the same cut-off $|t_{qc}|$, as described below.

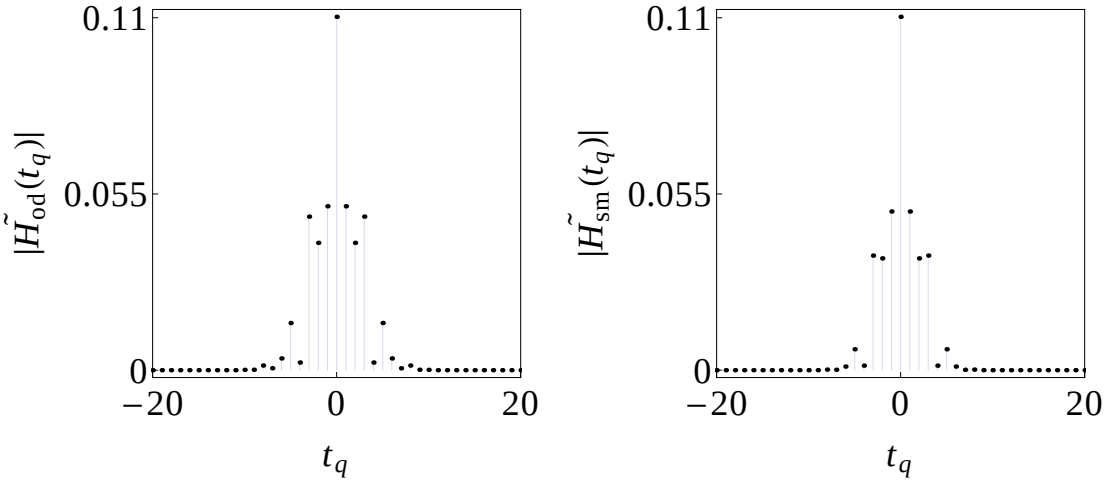

(a) $|\tilde{H}_{\rm od}(t_q)|$ after optimum deconvolution.

(b) $|\tilde{H}_{\rm sm}(t_q)|$ after optimum smoothening.

Figure 4.12

4.2.2.3 Optimum deconvolution

Here we use a smooth truncation of intensities in the Fourier domain instead of sudden truncation. In optimum deconvolution, in addition to the division by $P(q_y)$, we use the Hann filter (Fig.4.6) as a window function which smoothly goes to 0 at $|q_c|$ and beyond. We perform the correction with Hann window $H_{2n}[q_c = (t_{qc}\Delta_{q_y})] = \cos^{2n}(\pi t_q/2t_{qc})$ and $P[q_c = (t_{qc}\Delta_{q_y})]$ for $t_q \in [-t_{qc}, t_{qc}]$. Fig.4.12 shows $|\tilde{H}_{\rm od}(t_q)|$ (with optimum deconvolution) and $|\tilde{H}_{\rm sm}(t_q)|$ (with optimum smoothening) as a function of t_q.

4.3 Discussion

With the image we estimate the noise power ($\int_0^\infty |\sigma_(q_y)|^2 {\rm d}q_y$) as a result of one-step deconvolution $\left(\int_0^\infty |\sigma_d(q_y)|^2 {\rm d}q_y = 3.5 \times 10^{-3}\right)$, optimum deconvolution $\left(\int_0^\infty |\sigma_{od}(q_y)|^2 {\rm d}q_y = 1.5 \times 10^{-5}\right)$ and optimum smoothening $\left(\int_0^\infty |\sigma_{sm}(q_y)|^2 {\rm d}q_y \simeq 10^{-5}\right)$.

Thus noise power increases as a result of deconvolution. Clearly, for the image shown in Fig.4.1, where the feature width is (3×) larger than our psf width, it is sufficient to perform optimum smoothening, as the width estimates are not significantly affected by the blur. We estimate the blur caused by the convolution operation (microscope imaging). For simplicity let us assume that $h(x_0, y)$ for this feature is a Gaussian function $h(x_0, y) = \exp(-y^2/w_h^2)$. Then using $h(x_0, y) = f(x_0, y) \otimes p(y)$, we get $f(x_0, y) = \exp[-y^2/w_f^2]$ where $w_f^2 = (w_h^2 - w_p^2)$ and $w_p = d_y$. We know $w_p = 0.56\mu$m, $w_h = 1.65\mu$m, which gives $w_f \simeq 1.6\mu$m. Therefore, if we do not perform deconvolution for this feature then we make an error of $(w_h - w_f) \simeq 0.05\mu$m in estimating the true width which corresponds to 1 pixel of the image.

For features narrower than that shown in Fig.4.1, the observed width (say after optimum smoothening) can be significantly affected by the uncorrected blurring. However by using the relation $w_f^2 = (w_h^2 - w_p^2)$ we can estimate the true width. Of course, the deconvolution could provide us refined image that has the potential of revealing features otherwise hidden due to blurring.

Bibliography

[1] James Pawley, *Handbook of Biological Confocal Microscopy* (Springer, 3rd edition, 2006).

[2] E. H. I. Stelzer, Journal of Microscopy 189, 15-24 (1998).

[3] R. Nityananda, IAU, 11-17, (1994).

[4] R. J. Barlow, *Statistics : a guide to the use of statistical methods in the physical sciences* (John-Wiley and Sons, 1999).

[5] G. S. Downs and P. E. Reichley, The Astrophysical Journal Supplement Series 53, 169-240 (1983).

Chapter 5

Analysis of representative structures

In this chapter we fit the model (Chapter 3) by analyzing the processed image profile (as discussed in the Chapter 4) of representative observed structures. The simplest observed structures are simple tubules which have uniform inner and outer radii and small asymmetry. We also study more complicated asymmetric structures and describe the salient features of these structures.

5.1 Tubules

5.1.1 Simple tubule

We first consider the simple tubule (Fig. 5.1). We find that the tubule consists of a single core. The best fit is summarized in the Table 5.1 and shown in the Fig.(5.2). The jump in intensity at the central pixel is an artifact; the best fits to the two halves of the intensity profile yield slightly different values of α because of asymmetry. Since the best fit assigns only one value of α to each region, this jump is inevitable. In principle, it is possible to make α a function of the pixel number, but this does not lead to significant qualitative information, as witnessed by the fits given below.

We have analyzed the image profiles of a large number of tubules. We find that almost all tubules have a core, with very few tubules with core diameter close to the resolving limit. This is unlike the structure of "onions" which have a lamellar structure with singular density at the core [1]. Some discussions on myellae assume the core radius to be half the layer

spacing [2]. The tubules that we observe have much longer cores.

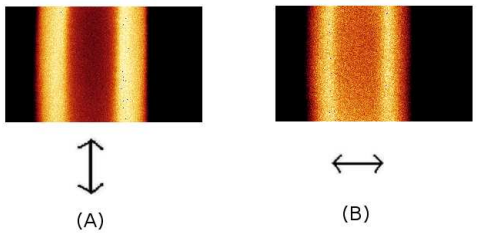

Figure 5.1: Confocal xyt-scan of a simple tube at the mid-z plane. The image size is $6.4\,\mu\text{m} \times 11.7\,\mu\text{m}$ (140×256) pixels. Arrows indicate polarization settings for the incident beam.

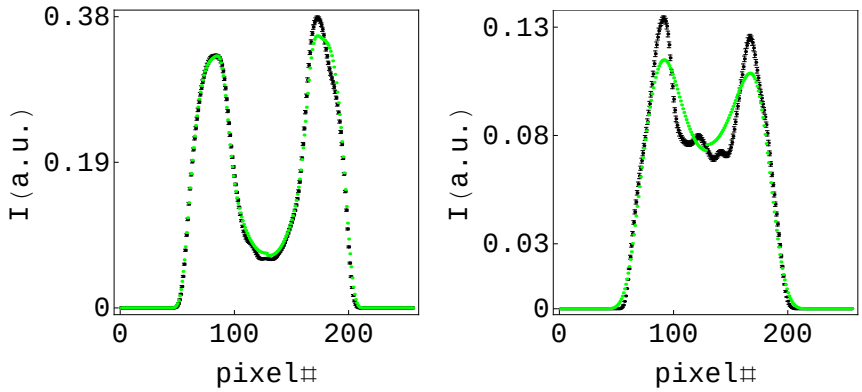

(a) $\shortparallel$ polarization best fit (green). (b) $\perp$ polarization best fit (green).

Figure 5.2

Table 5.1

Best Fit, $\Delta_z = (4.5 - 5)\mu$m,								
	$\shortparallel$ polarization				$\perp$ polarization			
	$2r_c(\mu\text{m})$	$2r_o(\mu\text{m})$	r_o/r_c	α	$2r_c(\mu\text{m})$	$2r_o(\mu\text{m})$	r_o/r_c	α
L	3.48	6.87	1.97	0.33	3.75	6.87	1.83	0.12
χ^2	$2 \times 10^{-}5$				$3 \times 10^{-}6$			
R	3.48	6.87	1.97	0.36	3.94	6.87	1.74	0.11
χ^2	$5 \times 10^{-}5$				$2 \times 10^{-}6$			

5.1.2 Asymmetric tubules

5.1.2.1 Asymmetric coaxial tubule - I

We now describe the structure of some asymmetric tubules. As discussed in Chapter (3), these tubules have asymmetry in shape as well as in density. Although the shape and density asymmetry cannot be fully separated, these can be reasonably characterized in terms of the sizes (given here in terms of the radii) and the parameter α. The image shown in the Fig.5.3 (movie xyz-scans 5.1.2.1) is that of a tubule which requires two distinct values of radii and α for a proper fit. The parameter values of best fit are summarized in the Table 5.2 where the different cross-sections of the tubule are denoted by T_1, T_2 *etc.* The radii of various regions are denoted by r_1, r_2 *etc.* Fig.(5.4) shows the best fit.

Some comments regarding these fits are in order, apply to all subsequent figures in this Chapter, and should be borne in mind: (*i*) we choose the parallel setting of polarization in all the following figures because we find that this setting is superior to the perpendicular setting in detecting lamella - solvent interfaces (edge detection). In the parallel polarization (parallel to the long-axis of the tubules) setting the dipole moment of dye molecules is predominantly in the plane of polarization, and (*ii*) the reason for the jump in intensity at the central pixel, as discussed above.

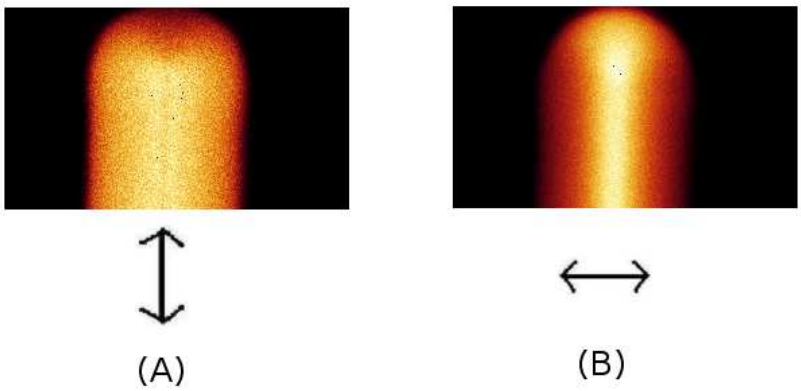

Figure 5.3: Confocal xyt-scan at the mid-z plane. The image size is $11.8\,\mu$m $\times$ $6.87\,\mu$m (256×150) pixels.

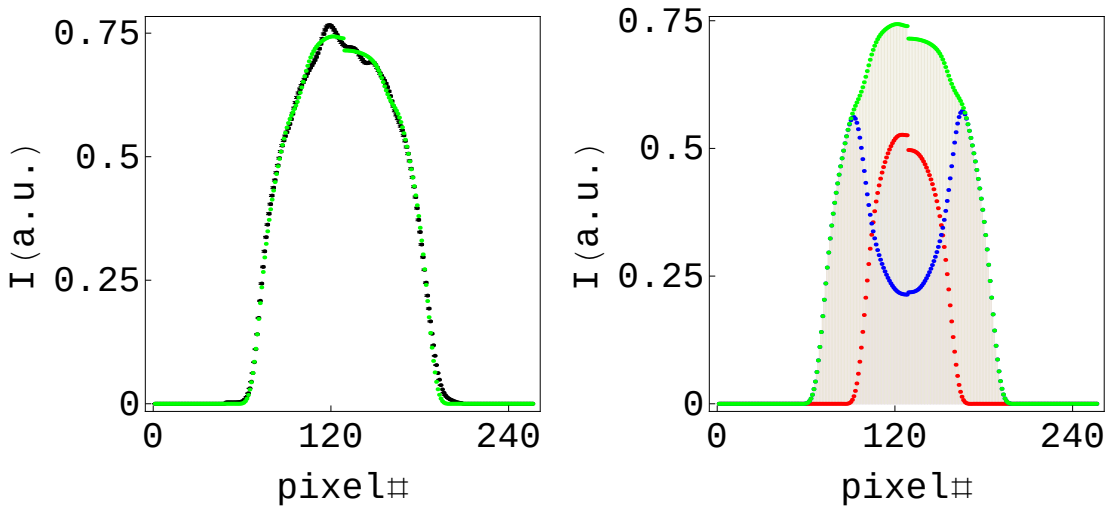

(a) Best fit (green). (b) Tubule structure decomposed into regions.

Figure 5.4: ∥ polarization.

Table 5.2

Best Fit, $\Delta_z = 5\mu$m					
		∥ polarization			
		$2r_1(\mu\text{m})$	$2r_2(\mu\text{m})$	r_2/r_1	α
L	T_1	0.28	3.07	11	0.53
	T_2	3.07	5.68	1.85	0.56
	χ^2	$5.6 \times 10^{-}11$			
R	T_1	0.18	3.07	17.1	0.5
	T_2	3.07	5.68	1.855	0.57
	χ^2	$\sim 10^{-}10$			

5.1.2.2 Asymmetric coaxial tubule - II

For the image shown in the Fig.5.5, best fit requires four values of α. The best fit is summarized in the Table 5.3 where different cross-sections of the tubule are denoted as T_1, T_2, *etc*. Fig.(5.6) shows the best fit.

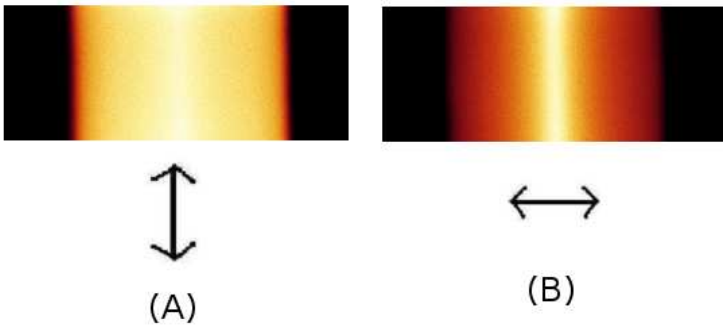

Figure 5.5: Confocal xyt-scan at the mid-z plane. The image size is $11.8\,\mu$m $\times$ $4.58\,\mu$m (256×100) pixels.

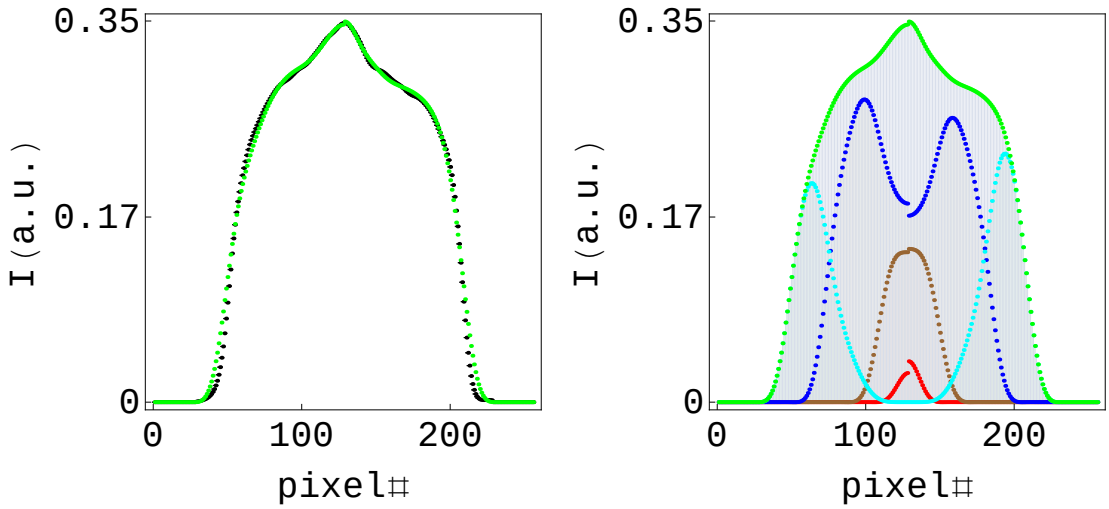

(a) Best fit (green). (b) Tubule structure decomposed into regions.

Figure 5.6: ⫴ polarization.

Table 5.3

Best Fit, Δ_z = 5.04μm					
		∥ polarization			
		$2r_1(\mu m)$	$2r_2(\mu m)$	r_2/r_1	α
L	T_1	0.18	0.6	3.3	0.027
	T_2	0.6	2.25	3.75	0.138
	T_3	2.25	5.49	2.44	0.278
	T_4	5.49	7.78	1.42	0.201
	χ^2	$2.3 \times 10^{-}9$			
R	T_1	0.18	0.55	3.1	0.038
	T_2	0.55	2.29	4.16	0.141
	T_3	2.29	5.49	2.4	0.261
	T_4	5.49	7.78	1.42	0.228
	χ^2	$1.7 \times 10^{-}9$			

5.1.2.3 Asymmetric coaxial tubules - III

The parameters for the image Fig.(5.7) for the indicated cross-sections are shown in Table 5.4. Figs.(5.8 and 5.9) show the best fit.

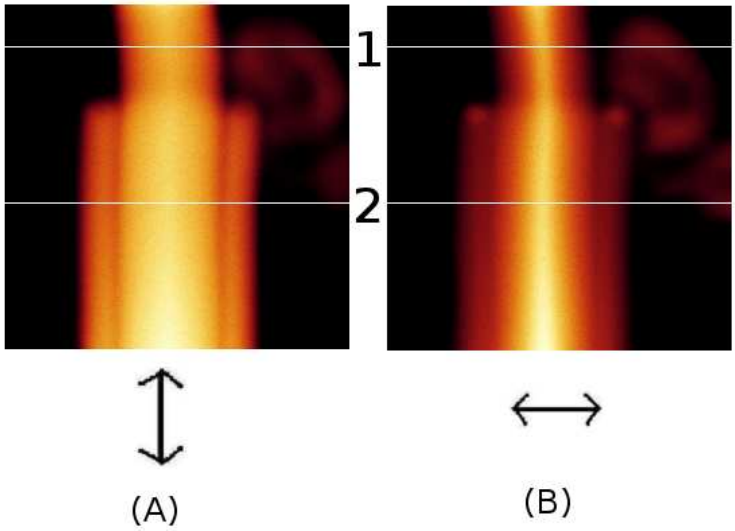

Figure 5.7: Confocal xyt-scan at the mid-z plane. The image size is 11.7μm $\times$ 11.7μm (512 $\times$ 512) pixels.

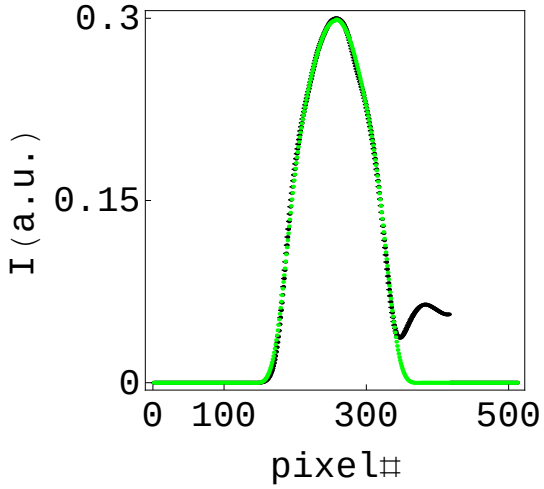

(a) Best fit (green).

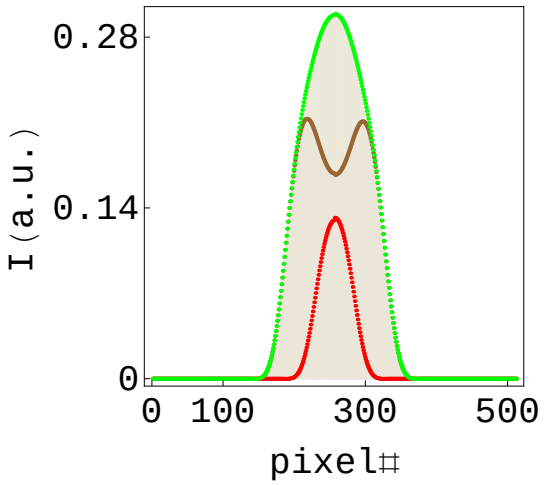

(b) Structure of the tubule decomposed into regions.

Figure 5.8: ∥ polarization, cross-section (1).

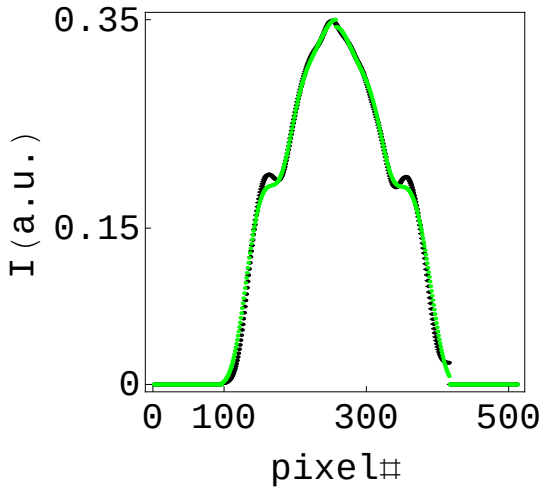

(a) Best fit (green).

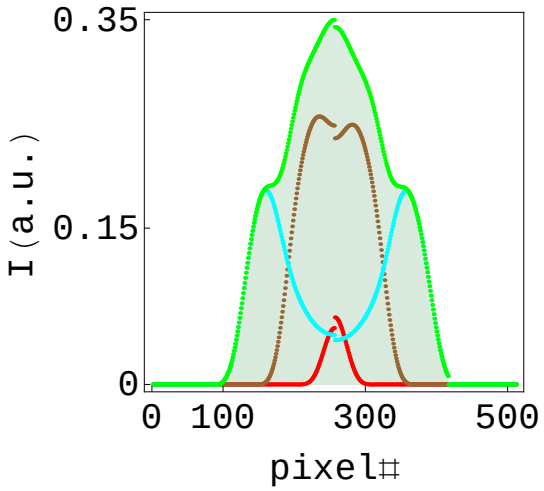

(b) Structure of the tubule decomposed into regions.

Figure 5.9: ∥ polarization, cross-section (2).

Table 5.4

Best Fit, Δ_z = 5.04μm						
			∥ polarization			
			$2r_1(\mu\text{m})$	$2r_2(\mu\text{m})$	r_2/r_1	α
1	L	T_1	0.1	1.56	15.6	0.13
		T_2	1.56	3.57	2.3	0.21
		χ^2	$\simeq 10^-10$			
	R	T_1	0.1	1.56	15.6	0.13
		T_2	1.56	3.66	2.35	0.21
		χ^2	5×10^-8			
2	L	T_1	0.1	0.73	7.3	0.27
		T_2	0.73	3.78	5.2	0.26
		T_3	3.78	6.27	1.66	0.19
		χ^2	7×10^-10			
	R	T_1	0.1	0.82	8.2	0.06
		T_2	0.82	3.85	4.7	0.25
		T_3	3.85	6.64	1.73	0.19
		χ^2	8×10^-10			

5.1.2.4 Asymmetric tubule - IV

The tubule depicted in Fig.5.10 (movie xyz-scans 5.1.2.4) is very asymmetric. The parameters for the image for the indicated cross-sections are given inTable 5.5 where different cross-sections of the tubule are denoted as T_1, T_2, *etc*. Figs.(5.11 to 5.13) show the best fit.

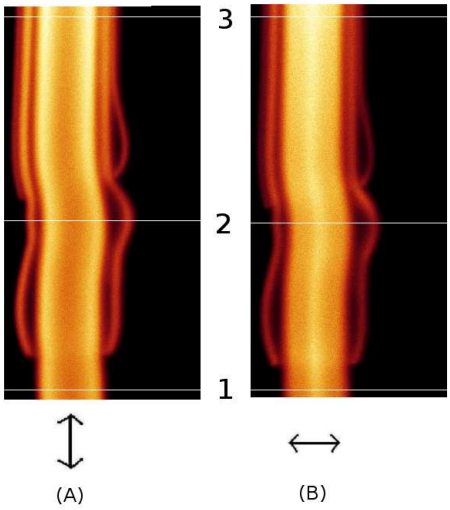

Figure 5.10: Confocal xyt-scan at the mid-z plane. The image size is $13.5\,\mu\text{m} \times 27\,\mu\text{m}$ (256×512) pixels.

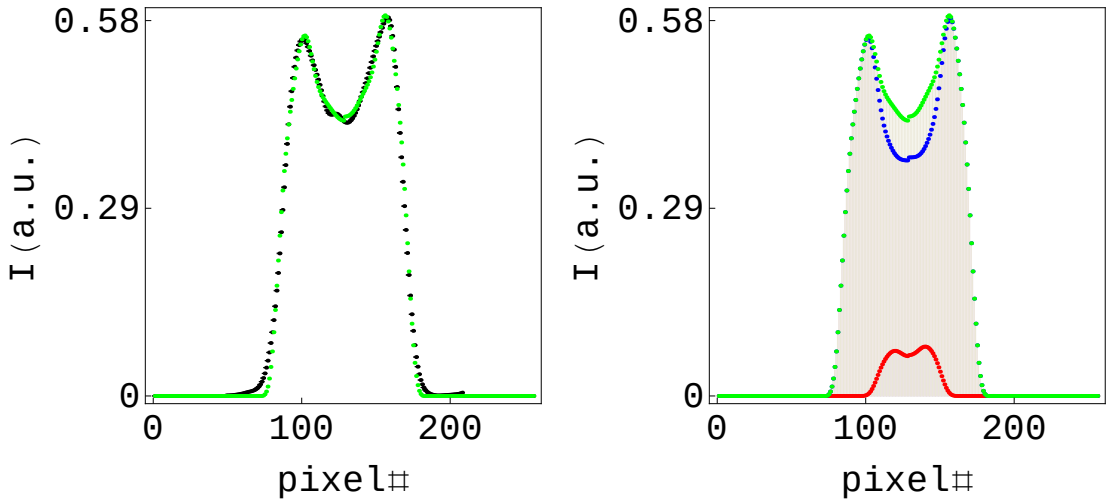

(a) Best fit (green).

(b) Tubule structure decomposed into regions.

Figure 5.11: ∥ polarization, cross-section (1).

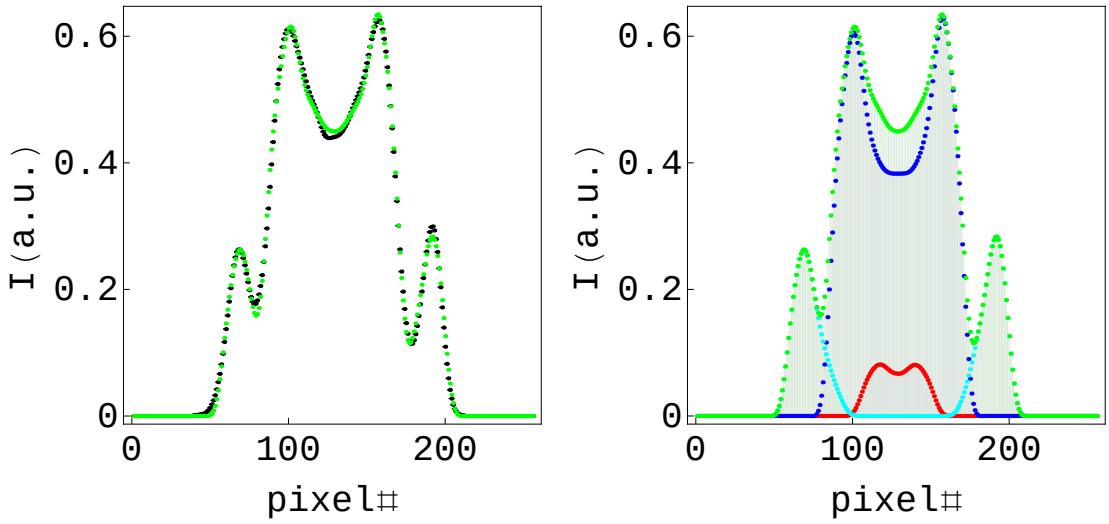

(a) Best fit (green). (b) Tubule structure decomposed into regions.

Figure 5.12: ∥ polarization, cross-section (2).

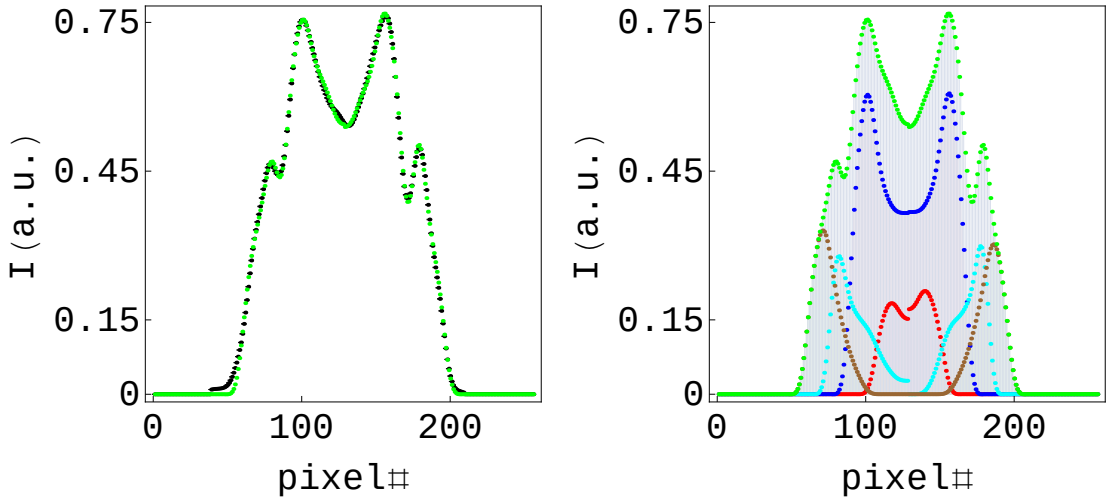

(a) Best fit (green). (b) Tubule structure decomposed into regions.

Figure 5.13: ∥ polarization, cross-section (3).

Table 5.5

Best Fit, $\Delta_z = 5.04\mu$m						
			∥ polarization			
			$2r_1(\mu\text{m})$	$2r_2(\mu\text{m})$	r_2/r_1	α
1	L	T_1	0.84	2.56	3.1	0.07
		T_2	2.56	5.05	1.97	0.55
		χ^2	6.5×10^-11			
	R	T_1	1.05	2.7	2.57	0.08
		T_2	2.7	4.84	1.79	0.58
		χ^2	4×10^-11			
2	L	T_1	1.05	2.73	2.6	0.08
		T_2	2.73	4.84	1.77	0.61
		T_3	6.1	7.68	1.26	0.26
		χ^2	7×10^-11			
	R	T_1	1.05	2.8	2.67	0.08
		T_2	2.8	4.73	1.69	0.63
		T_3	6.52	7.78	1.19	0.28
		χ^2	4×10^-11			
3	L	T_1	1.05	2.67	2.54	0.184
		T_2	2.67	4.94	1.85	0.604
		T_3	4.94	5.94	1.2	0.278
		T_4	5.94	7.57	1.27	0.33
		χ^2	8×10^-11			
	R	T_1	1.05	2.73	2.6	0.208
		T_2	2.73	4.9	1.8	0.607
		T_3	4.9	5.8	1.18	0.299
		T_4	5.8	7.36	1.275	0.302
		χ^2	3×10^-11			

Fig.(5.15) shows the intensity profile of a very asymmetric tubule at the marked cuts in the Fig. 5.14.

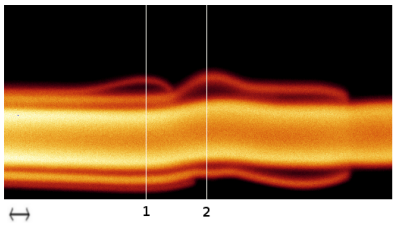

Figure 5.14

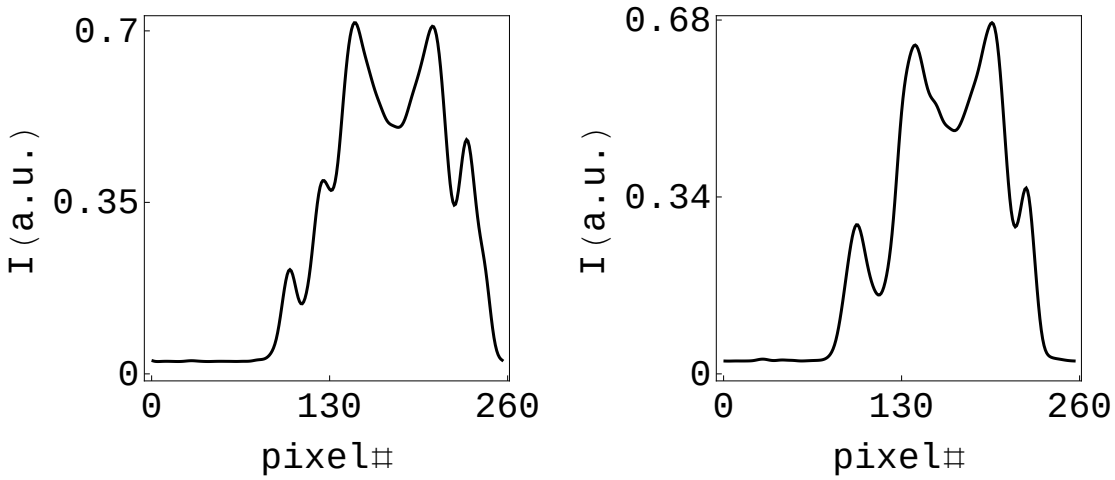

(a) (1). (b) (2).

Figure 5.15: ∥ polarization.

5.2 Beads

As described in (2), beads are prolate-ellipsoidal structures which appear on some tubules. In what follows, we study four types of archetypal beads. We note that the model developed in Chapter (3) does not apply to objects having two nonzero principal curvatures such as a bead. For this reason, we analyze the images in cross-sections which are flat, with some exceptional cross-sections (see below). The quantitative data obtained for the exceptional cross-sections taken at regions which are not flat are not reliable, however, these do provide important qualitative information.

We have analyzed several beads, and find that near the neck of beads the inner core of the tubules is not blocked by lipid material, *i.e.*, the inner core runs continuously through the tubules and the beads. Beads do not contain structures akin to multi-lamellar vesicles within them. However, the core radii of the tubule and the bead are different. Some beads trap the solvent in significantly large regions near their neck (see Figs. 5.18 and 5.22).

5.2.1 Bead on tubules

5.2.1.1 Bead on a tubule - I

The parameters for the bead shown in the Fig.5.16 (movie xyz-scans 5.2.1.1) are summarized in Table 5.6 for the cross-sections shown and Fig.(5.17) shows the best fit.

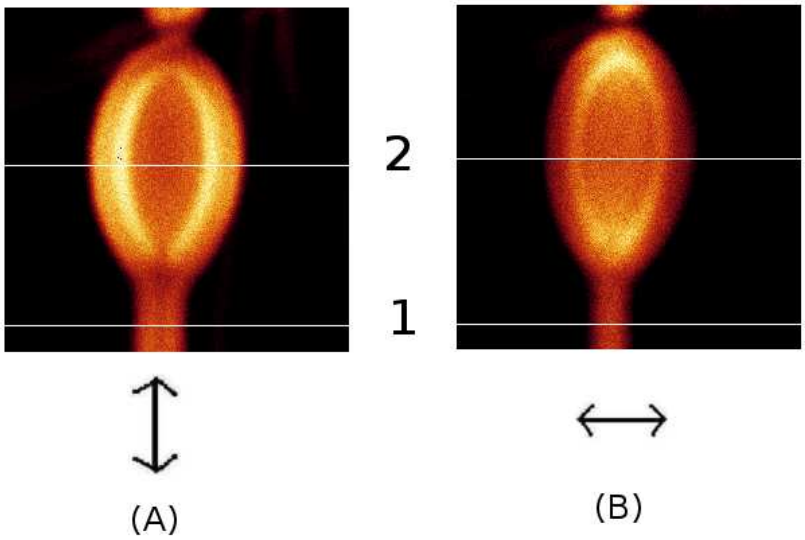

Figure 5.16: Confocal xyt-scan at the mid-z plane. The image size is $11.8\,\mu$m $\times$ $11.8\,\mu$m (256×256) pixels.

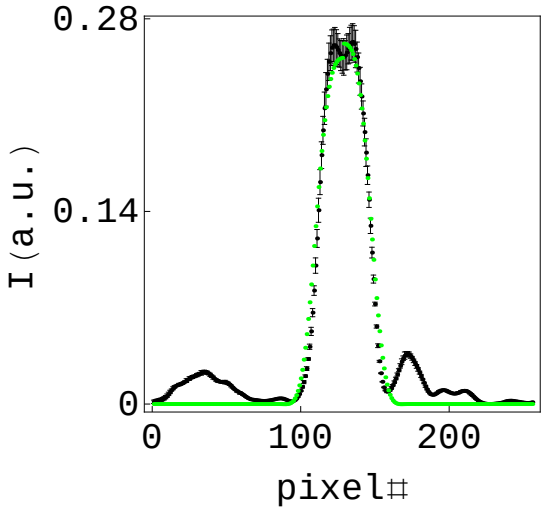

(a) ∥ polarization, cross-section (1)

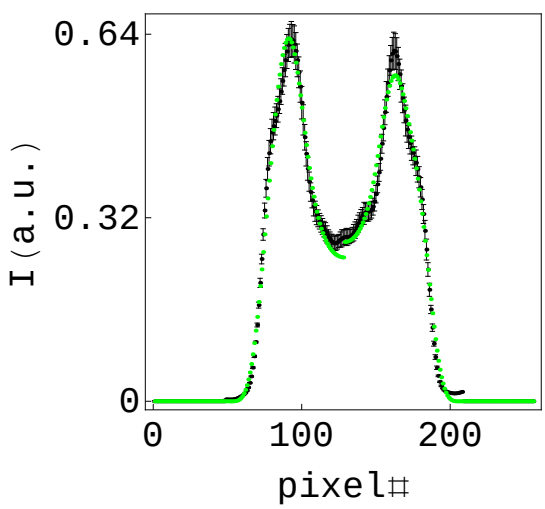

(b) Best fit (green).

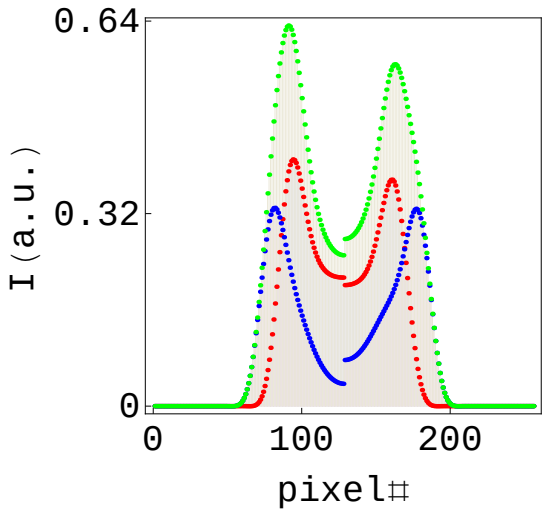

(c) Bead structure decomposed into regions, cross-section (2).

Figure 5.17: ∥ polarization.

Table 5.6

Best Fit, Δ_z = 5.04μm						
			∥ polarization			
			$2r_1(\mu m)$	$2r_2(\mu m)$	r_2/r_1	α
1	L		0.46	2.11	4.6	0.25
	χ^2		3×10^-5			
	R		0.46	2.11	4.6	0.26
	χ^2		5×10^-5			
2	L	T_1	3.2	4.4	1.38	0.41
		T_2	4.4	5.49	1.25	0.33
		χ^2	8.6×10^-8			
	R	T_1	2.93	4.6	1.57	0.38
		T_2	4.6	5.59	1.225	0.33
		χ^2	4.5×10^-8			

5.2.1.2 Bead on a tubule - II

Parameters for the bead shown in Fig.5.18 (movie xyz-scans 5.2.1.2) (with labeled cross-sections) are summarized in Table 5.7. Figs.(5.19) show the best fit.

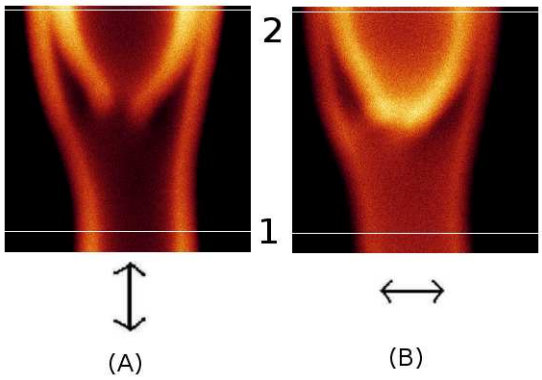

Figure 5.18: Confocal xyt-scan at the mid-z plane. The image size is $11.9\,\mu$m $\times$ $11.9\,\mu$m (512×512) pixels.

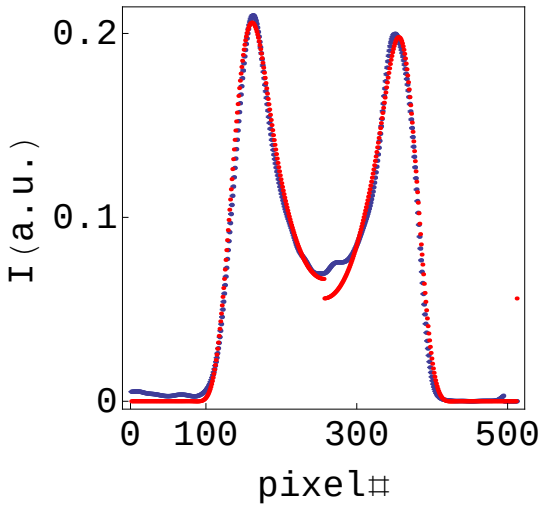

(a) Best fit (green) for the tubule cross-section (1).

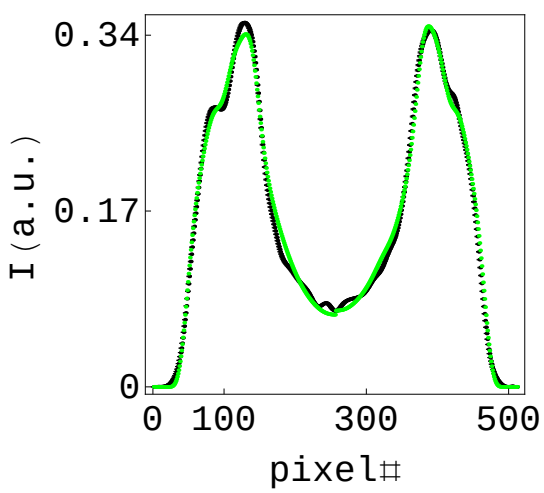

(b) Best fit (green).

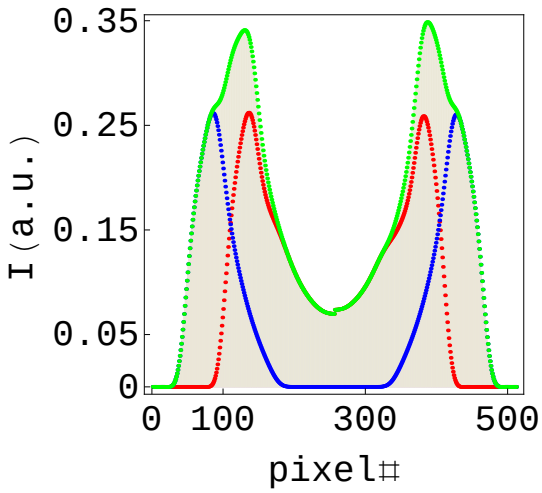

(c) Bead structure decomposed into regions, for the bead cross-section (2).

Figure 5.19: ⫴ polarization.

Table 5.7

Best Fit, Δ_z = 6.5 – 6.7μm(bead), 5.4 – 5.5μm(tubule)						
			∥ polarization			
			$2r_1(\mu m)$	$2r_2(\mu m)$	r_2/r_1	α
1	L		4.19	6.28	1.5	0.21
	χ^2		6×10^-6			
	R		4.42	6.28	1.42	0.2
	χ^2		2×10^-7			
2	L	T_1	5.35	7.56	1.41	0.26
		T_2	7.56	10	1.32	0.26
		χ^2	7×10^-9			
	R	T_1	5.58	7.56	1.36	0.26
		T_2	7.56	10	1.325	0.26
		χ^2	4×10^-9			

The intensity profiles for the bead shown in the Fig.5.20 are given in Fig.5.21.

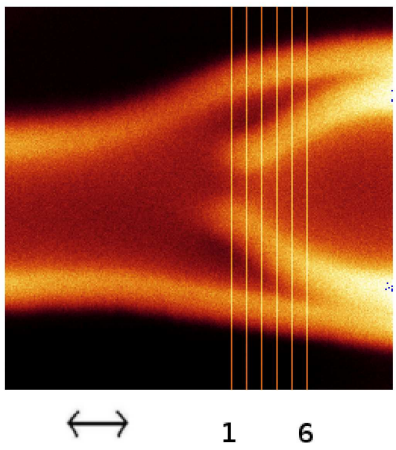

Figure 5.20

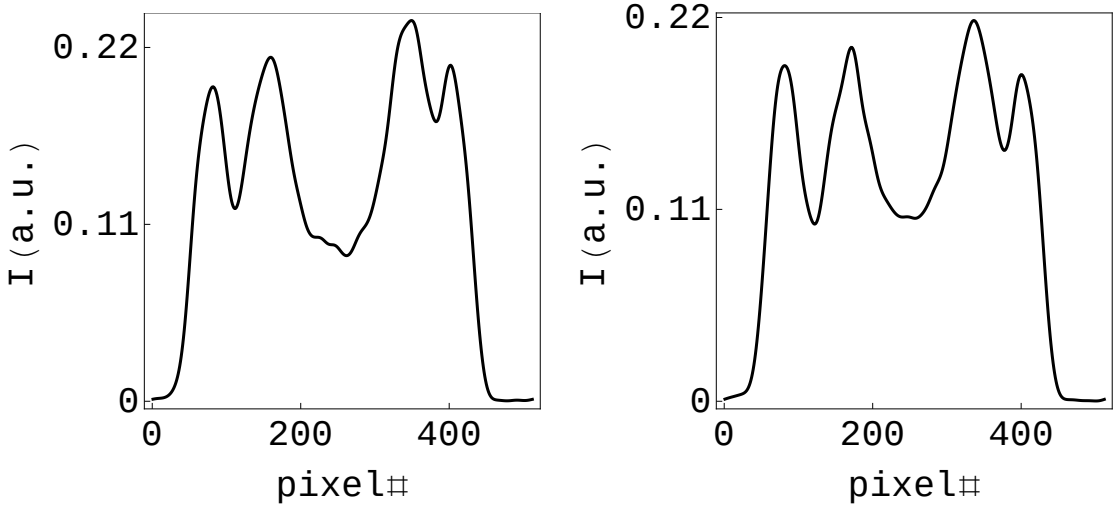

(a) (1).

(b) (2).

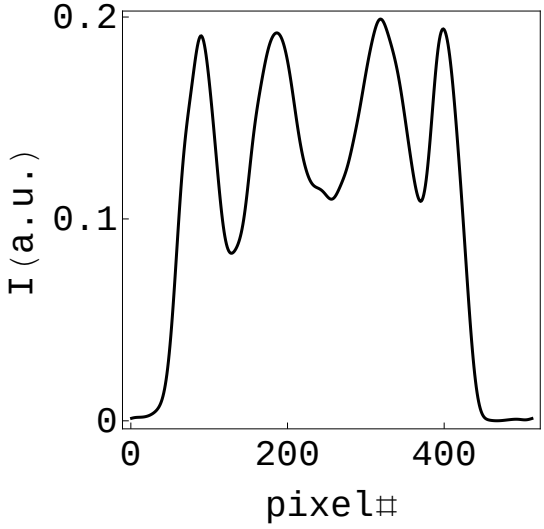

(c) (3).

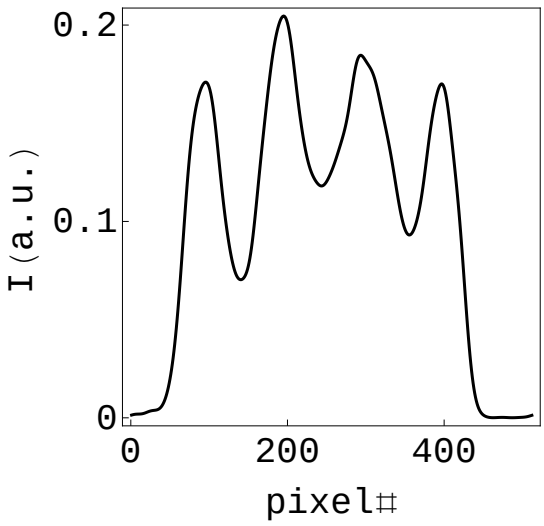

(d) (4).

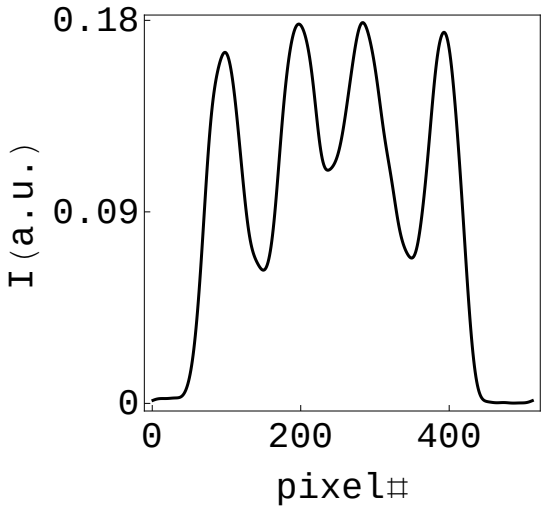

(e) (5).

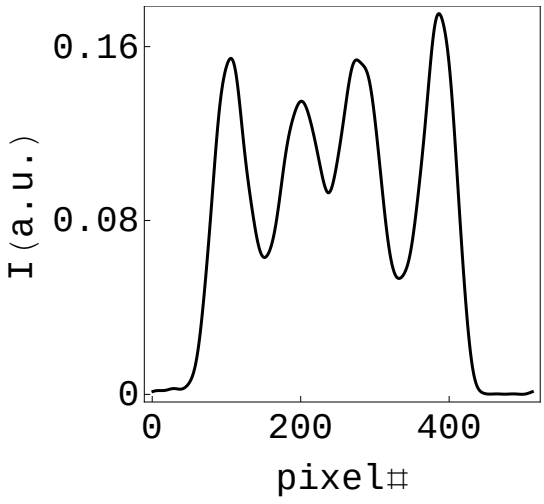

(f) (6).

Figure 5.21: ∥ polarization.

5.2.1.3 A bead which shows trapped solvent near the neck

Fig.5.22 (movie xyz-scans 5.2.1.3) depicts a bead where the region in which the solvent is trapped is clearly visible. The best fit is summarized in Table 5.8 and shown in the Fig.(5.23).

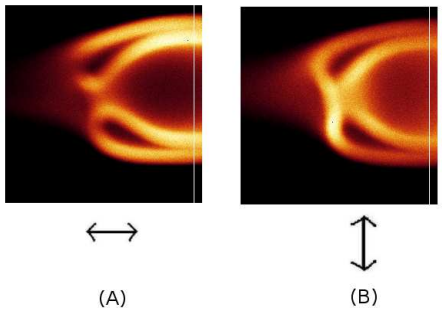

Figure 5.22: Confocal xyt-scan at the mid-z plane. The image size is $18.1\,\mu$m $\times$ $18.1\,\mu$m (256×256) pixels.

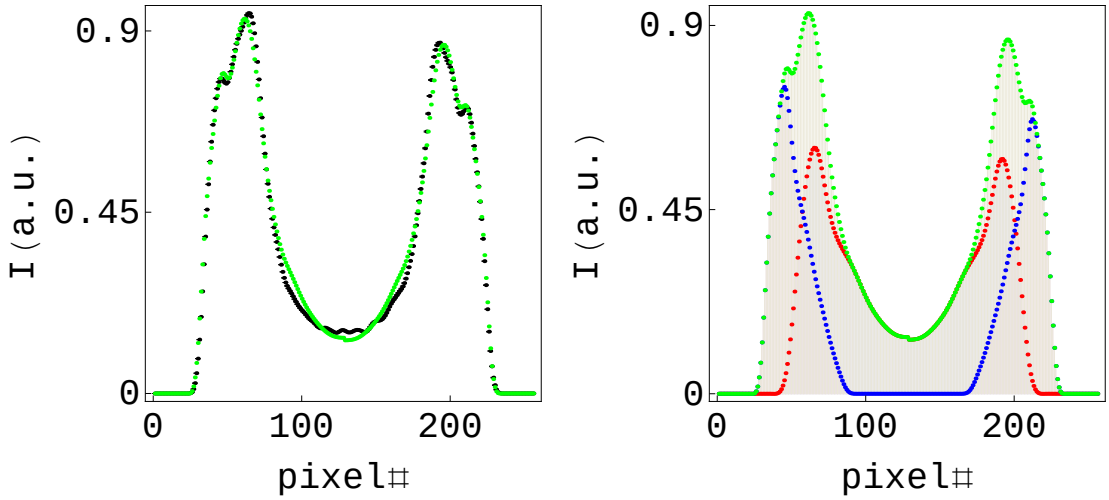

(a) Best fit (green). (b) Structure of the bead decomposed into regions.

Figure 5.23: ∥ polarization.

Table 5.8

Best Fit, $\Delta_z = 10 - 12\mu$m					
		$\shortparallel$ polarization			
		$2r_1(\mu\text{m})$	$2r_2(\mu\text{m})$	r_2/r_1	α
L	T_1	8.64	11.5	1.33	0.6
	T_2	11.5	14	1.22	0.75
	χ^2	$4.3 \times 10^{-}10$			
R	T_1	8.64	11.5	1.33	0.57
	T_2	11.5	14	1.225	0.67
	χ^2	$3 \times 10^{-}10$			

Figs.(5.25) shows the intensity profile at the marked cuts in the Fig. 5.24.

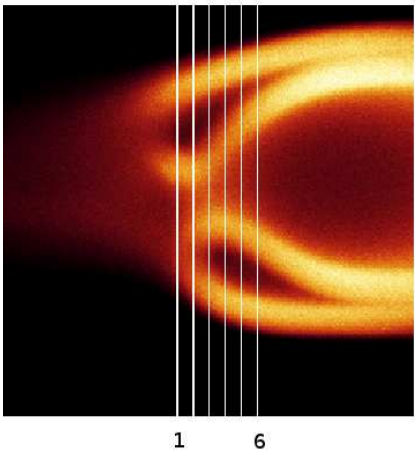

Figure 5.24

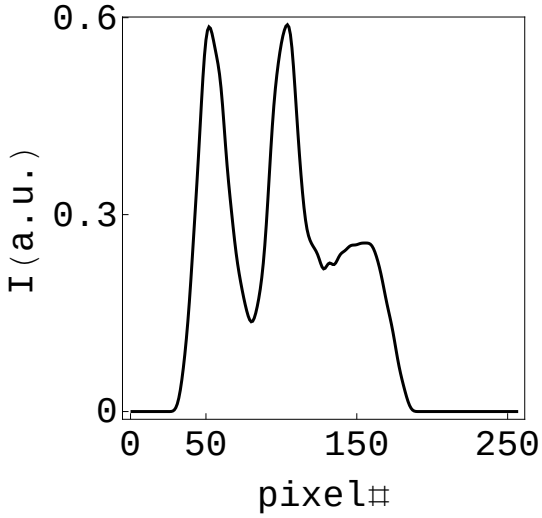

(a) (1).

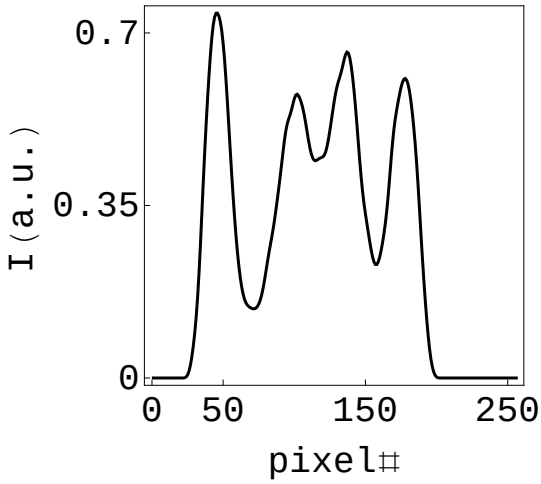

(b) (2).

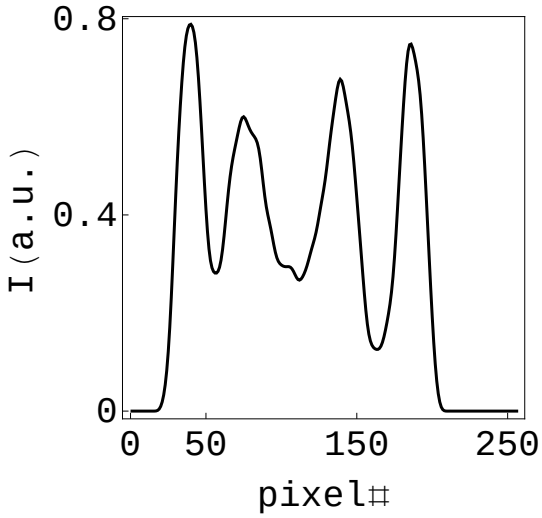

(c) (3).

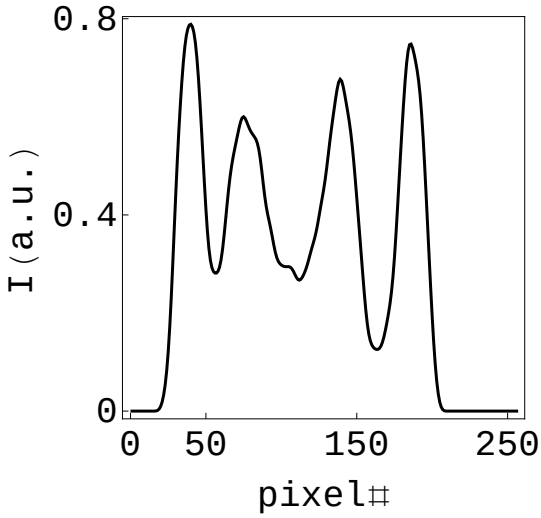

(d) (4).

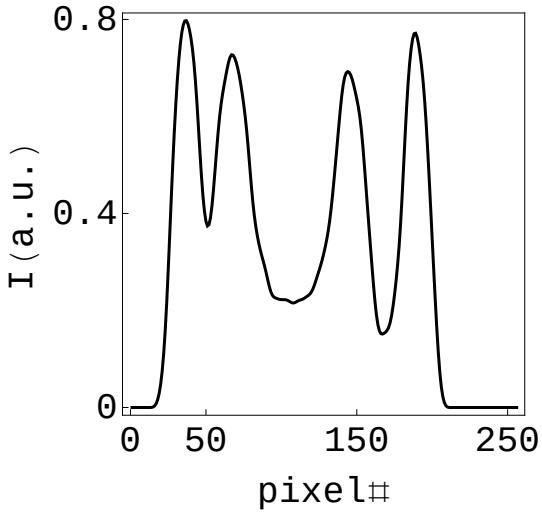

(e) (5).

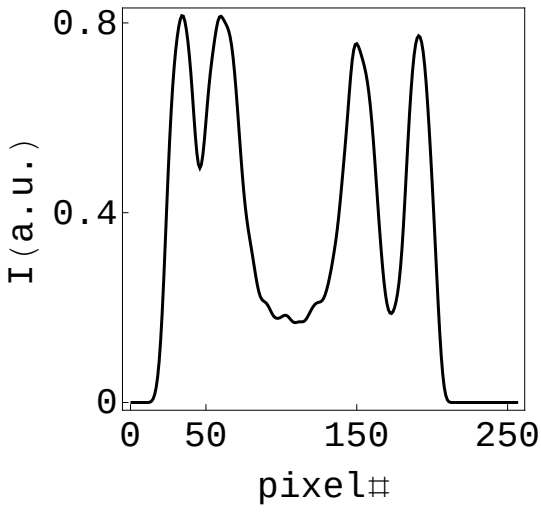

(f) (6).

Figure 5.25: ∥ polarization.

5.2.1.4 Bead on an asymmetric tubule

The parameters for Fig.5.26 (movie xyz-scans 5.2.1.4) are summarized in Table 5.9. Figs.(5.27 and 5.28) show the best fit.

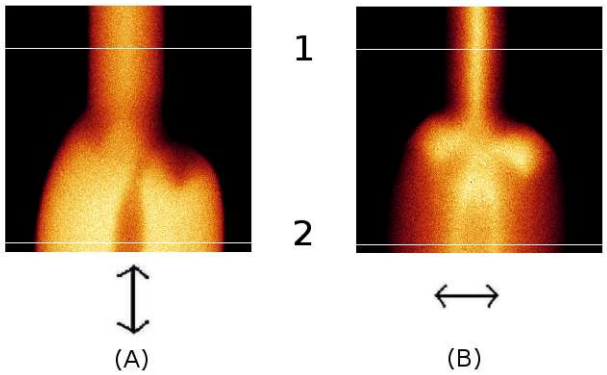

Figure 5.26: Confocal xyt-scan at the mid-z plane. The image size is $11.8\,\mu$m $\times$ $11.8\,\mu$m (256×256) pixels.

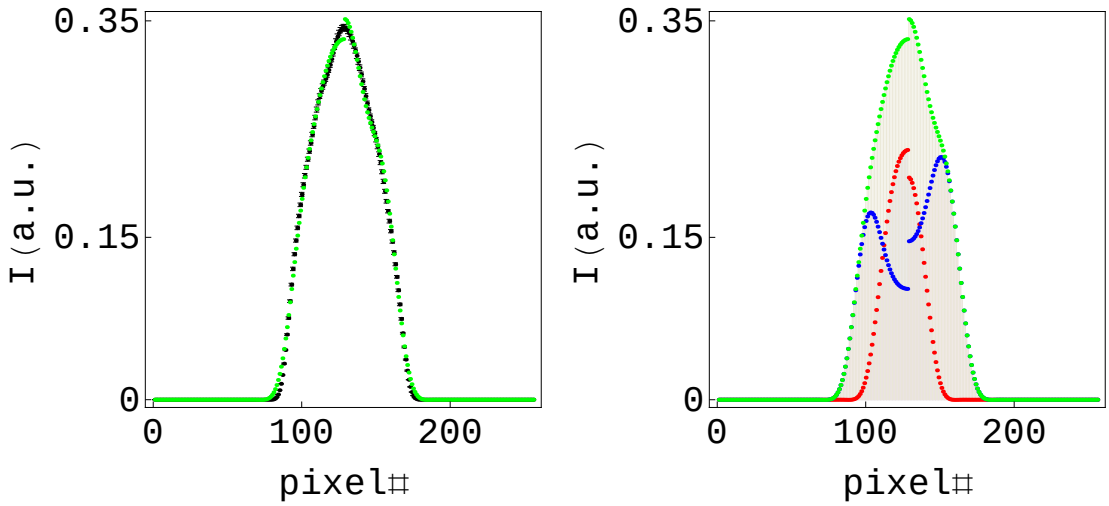

(a) Best fit (green).

(b) Tubule structure decomposed into regions, for the cross-section (1).

Figure 5.27: $\shortparallel$ polarization.

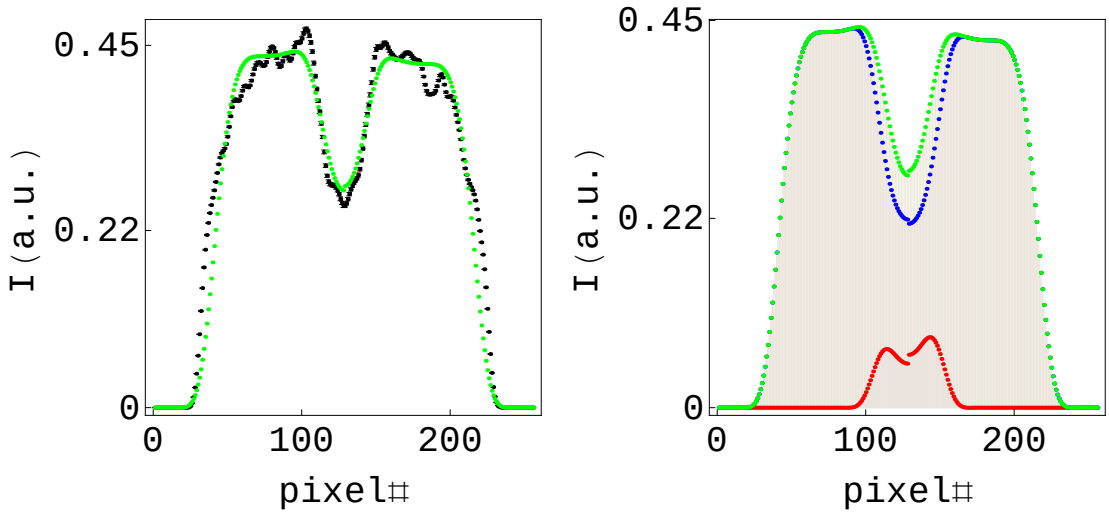

(a) Best fit (green).

(b) Bead structure decomposed into regions, for the cross-section (2).

Figure 5.28: ∥ polarization.

Table 5.9

Best Fit, $\Delta_z = 5.04\mu$m						
			∥ polarization			
			$2r_1(\mu\text{m})$	$2r_2(\mu\text{m})$	r_2/r_1	α
1	L	T_1	0.18	2.25	12.5	0.23
		T_2	2.25	3.66	1.63	0.17
		χ^2	$2 \sim 10^{-}10$			
	R	T_1	0.18	1.37	7.6	0.21
		T_2	2.29	3.66	1.6	0.22
		χ^2	$2 \times 10^{-}10$			
2	L	T_1	1.65	2.29	1.4	0.068
		T_2	2.29	8.7	3.8	0.44
		χ^2	$2.4 \times 10^{-}8$			
	R	T_1	1.65	2.29	1.4	0.08
		T_2	2.29	8.7	3.8	0.43
		χ^2	$2 \times 10^{-}8$			

Bibliography

[1] H. Diamant, M. E. Cates, Eur. Phys. J. E 4, 223 (2001).

[2] J. R. Huang, L. N. Zou, and T.A. Witten, Eur. Phys. J. E 18, 279-285 (2005).

Chapter 6

A phenomenological model for the stability of simple tubules

6.1 Introduction

Based upon our experimental observations (Chapter 2) and the elasticity theory of smectic-A liquid crystals (L_α phase of lyotropics, and the thermotropic smectic-A phase have the same symmetry) we propose a phenomenological model to analyze the stability of simple cylindrical MLTs with uniform cross-section.

We list the pertinent experimental observations upon which our analysis is based:

1. After the sample cell is sealed the tubules and beads are stable for over one day (Section 2.6.1.3).

2. The tubules are capped at the end (Fig.6.1).

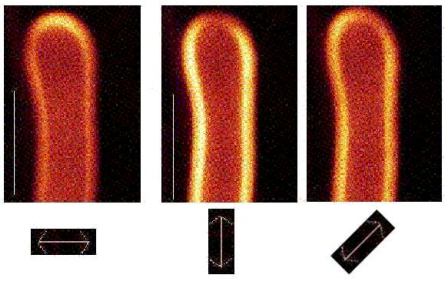

Figure 6.1: The end-cap of an MLT. Double arrow shows the incident laser polarization. Scale bar= 10μm.

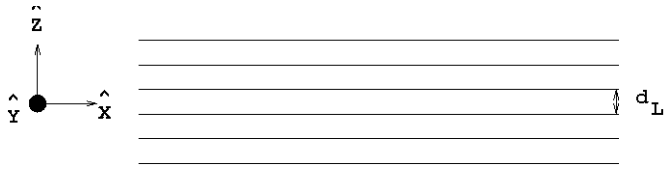

Figure 6.2: Schematic of the undistorted L_α phase, each line represents a bilayer.

3. Tubules emanate from defects in the lipid reservoir (Section 2.6.1.1).

4. Tubules have a broad range of r_c and r_o (see values in the tables, Chapter 5).

Given the above observations, in particular the long life-time of the structures, it is reasonable to consider these as quasi-equilibrium structures. We can therefore utilize elasticity theory in order to understand the stability and structure of MLTs.

Spin-coating spreads the sample much more uniformly than syringe-coating [1, 2]. We have discussed (Section 2.4) that MLTs do not grow if spin-coated samples are hydrated in excess water. Further, we have seen that MLTs originate from defects on the reservoir. MLTs are capped. It is therefore possible that the solvent gets trapped in some MLTs from both ends. The solvent pressures (including the osmotic pressure) inside and outside the tubule can then be different. We note that the lamellar curvature at inner and outer interfaces of MLTs are different. The curvature- stress at the outer interface $r_o > r_c$ is clearly smaller than that at the core. The pressure difference across the MLTs can be stabilized by the solvent trapped within closed regions at the reservoir end. Our analysis must therefore allow for this possibility as well as the fact that MLTs have widely different core- and outer radii.

In the present treatment we do not address the question as to why the tubules are cylindrical (this is not known), rather, we assume the shape to be cylindrical and find the conditions for stability.

6.2 Elasticity of lyotropic smectics

Smectic liquid crystals are one dimensional “solids” composed of fluid layers exhibiting quasi-long-range order in the direction orthogonal to the layers [3, 4]. For small distortions, the elastic free energy (in Cartesian coordinates) is [3, 4]

$$F_{\mathrm{el}} = \int \left[\frac{B}{2}\left(\partial_z u\right)^2 + \frac{\kappa}{2}H^2 + \kappa_{\mathrm{G}} K\right] dx\, dy\, dz, \tag{6.1}$$

where z is the "solid- like" layering direction (Fig.6.2), $u(x, y, z)$ is the layer displacement field. $(B/2)\left(\partial_z u\right)^2$ is the energy density for compression (or extension) of the layer spacing, $H = (1/2)(1/R_1 + 1/R_2)$ is the mean curvature and $K = (1/R_1 R_2)$ is the Gaussian curvature, with principal radii of curvature R_1 and R_2 (Fig.6.3). B is the compression modulus. $(\kappa/2)H^2$ is the energy density for bending the layers, with bend modulus κ. The Gaussian curvature term contributes to the energy only if the system under study has a boundary, or undergoes change in topology (number of handles) [5].

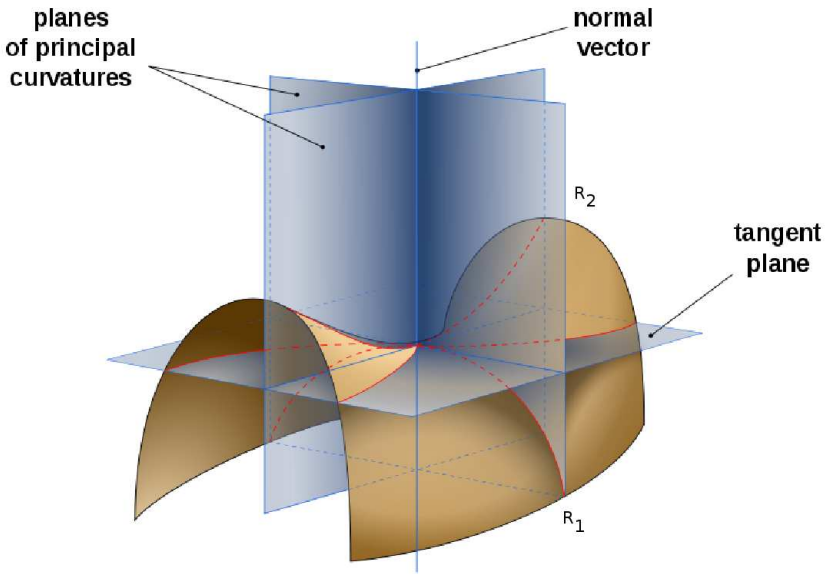

Figure 6.3: Principle radii of curvature R_1 and R_2 for a surface.

It is convenient to use cylindrical polar coordinates. The elastic free energy in cylindrical polar coordinates is

$$F_{\mathrm{el}} = \int \left[\frac{B}{2}\left(\partial_r u\right)^2 + \frac{\kappa}{2}\left(\partial_r^2 u + \frac{1}{r^2}\partial_\phi^2 u + \frac{1}{r}\partial_r u\right)^2\right] r\mathrm{d}r\,\mathrm{d}\phi\,\mathrm{d}z \tag{6.2}$$

where the symbols have their usual meaning and ∂_r stands for the differential operator $\mathrm{d}/\mathrm{d}r$. For cylindrically symmetric MLTs with uniform cross-section, $\partial_z u = \partial_\phi u = 0$. Thus the elastic free energy reduces to

$$F_{\mathrm{el}} = \frac{B}{2}\int\left[\left(\partial_r u\right)^2 + \lambda^2\left(\partial_r^2 u + \frac{1}{r}\partial_r u\right)^2\right] r\mathrm{d}r\,\mathrm{d}\phi\,\mathrm{d}z \tag{6.3}$$

where $\lambda^2 = \kappa/B$. Note that B has the dimension of pressure, and λ has the dimension of length. Although the term with the coefficient λ^2 is sub-dominant, it is crucial in stabilizing cylindrical MLTs (see below).

6.3 Condition for stability

In equilibrium the Euler-Lagrange equation $\delta F_{\mathrm{el}}/\delta u = 0$ [6] holds within the bulk of the lamellar region of the MLT:

$$\frac{2\pi B\left((\lambda - r)\,u'(r) + r\left(\left(-\lambda^2 - r^2\right)u''(r) + \lambda^2 - r^2\left(ru^{(4)}(r) + 2u^{(3)}(r)\right)\right)\right)}{r^3} = 0, \tag{6.4}$$

where the order derivatives of $u(r)$ is denoted by the superscript of u. The solution to the Euler-Lagrange equation is given by

$$u(r) = c_1\log(r) + c_2\lambda^2\left(I_0\left(\frac{r}{\lambda}\right) - 1\right) + c_3\lambda^2 Y_0\left(-\frac{ir}{\lambda}\right) + c_4, \tag{6.5}$$

where $I_n(x)$ and $Y_{\mathrm{n}}(x)$ [7] respectively represent modified Bessel function of the first kind and Bessel function of the second kind and order n, and the four constants of integration are denoted with the symbol c. The layer displacement $u(r)$ is real. We therefore drop the term proportional to $Y_0\,(-ir/\lambda)$ that is pure imaginary.

It now remains to find the constants of integration. In order that the MLT be stable, the radial elastic stresses at inner and outer interfaces must balance the respective pressures. The Euler-Lagrange equation has to solved using this stress- balance boundary conditions. Thus $\sigma_{\mathrm{i}} = -p_{\mathrm{i}}$, and $\sigma_{\mathrm{o}} = -p_{\mathrm{o}}$.

The radial stress $\sigma(r)$ is extracted by noting that in cylindrical polar coordinates the Euler-Lagrange equation can be written as $(1/r)\partial_r[r\sigma(r)] = 0$. This yields

$$\sigma(r) = \frac{2\pi B\left(\left(-\lambda^2 - r^2\right)u'(r) + \lambda^2 r\left(ru^{(3)}(r) + u''(r)\right)\right)}{r^2}. \tag{6.6}$$

Using the stress- balance boundary conditions at the interfaces [6] we obtain

$$c_1 = r_\mathrm{i}\left(\frac{p_\mathrm{i} r_\mathrm{i}^2}{4\pi B\lambda^2 + 2\pi B r_\mathrm{i}^2} + c_2\lambda\left(\frac{\lambda r_\mathrm{i} I_0\left(r_\mathrm{i}/\lambda\right)}{2\lambda^2 + r_\mathrm{i}^2} - I_1\left(r_\mathrm{i}/\lambda\right)\right)\right), \tag{6.7}$$

and

$$c_2 = \frac{p_\mathrm{i} r_\mathrm{i}^3\left(2\lambda^2 + r_\mathrm{o}^2\right) - p_\mathrm{o} r_\mathrm{o}^3\left(2\lambda^2 + r_\mathrm{i}^2\right)}{2\pi B\lambda\left(\left(2\lambda^2 + r_\mathrm{i}^2\right)\left(\left(2\lambda^2 + r_\mathrm{o}^2\right)\left(r_\mathrm{i} I_1\left(r_\mathrm{i}/\lambda\right) - r_\mathrm{o} I_1\left(r_\mathrm{o}/\lambda\right)\right) + \lambda r_\mathrm{o}^2 I_0\left(r_\mathrm{o}/\lambda\right)\right) - \lambda r_\mathrm{i}^2\left(2\lambda^2 + r_\mathrm{o}^2\right) I_0\left(r_\mathrm{i}/\lambda\right)\right)}. \tag{6.8}$$

The constant c_3 corresponds to uniform, rigid displacements of the entire MLT, and can therefore be set to zero by an appropriate choice of the origin of the coordinate system. We have thus solved the equation of stability (the Euler-Lagrange equation) subject to boundary conditions stated above.

We choose the dimensionless unit of length as $(r_\mathrm{i}/\lambda) = 1$, and measure pressure in units of B. For the L_α phase under consideration, λ is of the order of a few layer spacings and $B \simeq 10$atm. If the inner and outer pressures are zero, both the compression and the stress is zero throughout the tubule. Fig.6.4 shows the layer compression $\partial_r u(r)$ as a function of radial coordinate r in the dimensionless units mentioned above.

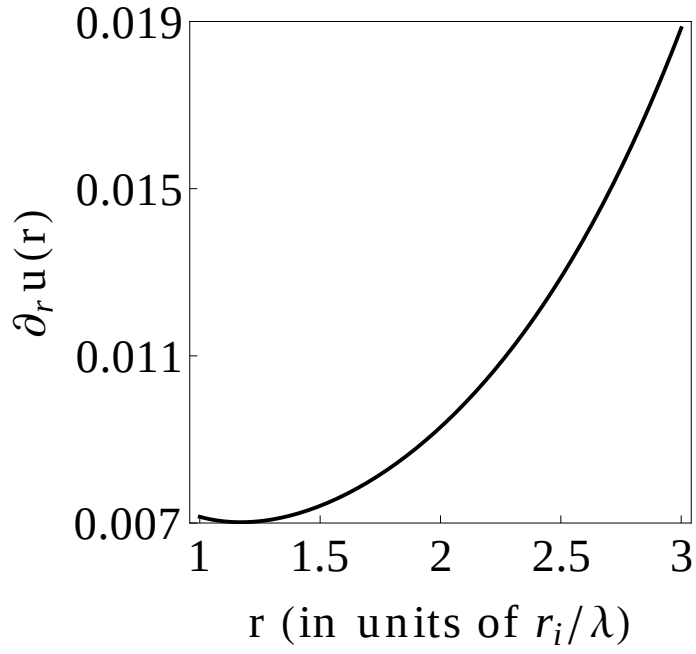

Figure 6.4: $P_\mathrm{o} = P_\mathrm{i} = 1$ atm. $r_\mathrm{o} = 3$ and $r_\mathrm{i} = 1$ in the units of (r_i/λ).

Bilayer compression is a direct measure of change in density. We find that even if the

inner and outer pressures are equal (1 atm for Fig.6.4), the MLT has varying, non-zero bilayer compression.

The compressive and curvature- stresses have to balance within the bulk of the MLT for stability. This is the reason why we need to include the sub-dominant term proportional the λ^2 in the elastic free energy.

Fig.6.5 compares the compression in the above case with one in which the pressure difference is 0.1 atmosphere. Even in this extreme case we find that the compression, and therefore the density profile of lamellar material in the MLT does not change significantly.

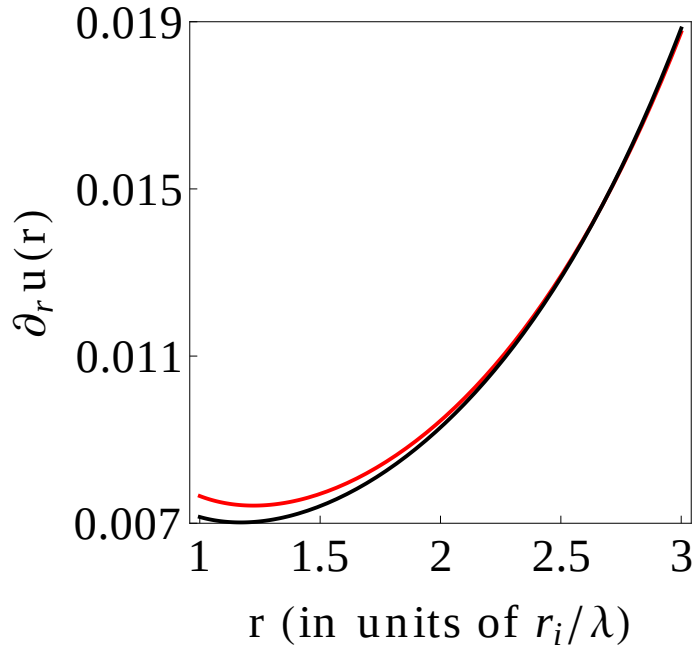

Figure 6.5: Red (P_i = 1.1 atm, P_o = 1 atm), black ($P_o = P_i$ = 1 atm), r_o = 3 and r_i = 1 in the units of (r_i/λ).

A definitive statement cannot be made as to whether the above analysis assuming equilibrium applies to MLTs generated via an explosive event. Notwithstanding this, we have demonstrated that cylindrical morphologies are stable for elastic objects having compression- and bend elasticity.

Bibliography

[1] U. Mennicke and T. Salditt, Langmuir 18, 8172 (2002).

[2] Seul and Sammon, Thin Solid Films 185, 187-305 (1990).

[3] P. G. de-Gennes and J. Prost, *The physics of liquid crystals* (Oxford University Press, 2nd edition, 1994).

[4] P. M. Chaikin and T. C. Lubensky, *Principles of condensed matter physics* (Oxford University Press, 1998).

[5] S. Safran, *Statistical thermodynamics of Surfaces, Interfaces, and Membranes* (Westview Press, Cambridge, 2003).

[6] L. D. Landau, L. P. Pitaevskii, E.M. Lifshitz and A. M. Kosevich , *Theory of Elasticity* (Pergamon Press, 3rd edition, 1986).

[7] Milton Abramowitz and Irene Stegun, *Handbook of Mathematical Functions* (Dover, New York, 1972).